

**TERNARY AND QUATERNARY LIPID PHASE DIAGRAMS TO INVESTIGATE  
MEMBRANE RAFT BEHAVIOR**

A Dissertation

Presented to the Faculty of the Graduate School  
of Cornell University

In Partial Fulfillment of the Requirements for the Degree of  
Doctor of Philosophy

by

Tatyana M. Konyakhina

January 2015

© 2015 Tatyana M. Konyakhina

# **TERNARY AND QUATERNARY LIPID PHASE DIAGRAMS TO INVESTIGATE MEMBRANE RAFT BEHAVIOR**

Tatyana M. Konyakhina, Ph. D.

Cornell University 2015

Nonrandom mixing of lipids and proteins in the plasma membrane plays an important role in many cellular processes, including immune signaling, protein sorting, endocytosis, and virus entry and exit, yet the mechanisms governing the coalescence of these small domains are still not completely understood. Functional domains (“lipid rafts”) that arise from nonrandom mixing of membrane components are believed to be important in governing the spatial organization of lipids and proteins. Model systems comprising chemically simplified lipid mixtures have played a central role in studies aimed at elucidating the mechanisms responsible for forming and regulating the size and lifetime of membrane domains.

In this study we report the first solved phase diagram for the four-component mixture DSPC/DOPC/POPC/Chol (distearoylphosphatidylcholine/dioleoylphosphatidylcholine/1-palmitoyl,2-oleoylphosphatidylcholine/cholesterol), which exhibits a domain size transition from nanoscopic to macroscopic, including a regime of spatially modulated domains within the region of coexisting liquid-disordered (Ld) and liquid-ordered (Lo) phases. I also describe a novel FRET method used to determine boundaries. This phase diagram clearly shows that all phase boundaries determined for the 3-component mixture containing DOPC transition smoothly into the boundaries for the 3-component mixture containing POPC, which has

nanoscopic phase domains of Ld + Lo. Together, our studies show that cells could control domain size and morphology by merely changing lipid composition.

Phospholipids having a polyunsaturated acyl chain are abundant in biological membranes, but their behavior in lipid mixtures is difficult to study. In this work we elucidate the nature of such mixtures with this report of the first ternary phase diagram containing the polyunsaturated lipid SDPC in mixtures of BSM/SDPC/Chol (brain sphingomyelin/1-stearoyl-2-docosahexaenoyl-sn-glycero-3phosphocholine/ cholesterol). These mixtures show macroscopic Ld + Lo phase separation, with phase boundaries determined by FRET and by fluorescence microscopy imaging of giant unilamellar vesicles (GUVs). Surprisingly, SDPC mixes with BSM/Chol similarly to how DOPC and POPC mix with BSM/Chol. In addition, modulated phases are observed within the Ld + Lo liquid-liquid immiscibility region upon addition of fourth component POPC. We find mixtures of BSM/SDPC/POPC/Chol to exhibit nanoscopic Ld + Lo domains over a very large volume of composition space.

In this work we have successfully accomplished the following goals: 1) solved the first ternary phase diagram containing a PUFA lipid; 2) solved the first phase diagram for a four-component lipid bilayer mixture, including developing a new FRET method for accurate location of boundaries; and 3) synthesized a novel phosphorescent lipid-probe analog.

## **BIOGRAPHICAL SKETCH**

Tatyana was born and raised in Moscow, Russia. At the age of 17 she left everything behind to pursue new adventures in the US. Working multiple jobs since the age of 17, she enrolled in a community college where she (often) excelled in science and math, but was not really that good at Spanish. She then was offered a scholarship at Le Moyne College and finished her B.S in Chemistry and Physics, along with many volunteering and community outreach opportunities she undertook. She fell in love with lipids and membranes during Biochemistry class and hasn't deviated from it since then. After a brief employment at Syracuse University, she moved to Ithaca. She thought Ithaca was a huge change from Moscow. She struggled, she succeeded, she failed, she rose above; Tatyana didn't give up and she made it to the end.

## To Life

“Everything will be okay in the end. If it's not okay, it's not the end.” — John Lennon

## ACKNOWLEDGMENTS

I owe an enormous debt to my advisor and mentor Dr. Gerald Feigenson, who provided me with an opportunity to do science. Not only has he guided me along the way, but also motivated me and encouraged me to persevere and push through many difficult times. I owe many thanks to my committee members Dr. Holger Sondermann and my biomedical engineering minor advisor Dr. Warren Zipfel. This work would be impossible without my lab mates and all the coauthors: Dr. Shin Lin Goh, Dr. Fred Heberle, Dr. Jon Amazon, Dr. Robin Smith Petruzielo, Nelson Morales and David Ackerman. I am grateful for the support of Dr. Theresa Beaty and Dr. David Craig (Le Moyne College) for their support and guidance since I had a pleasure of meeting them in 2005. Many thanks to Dr. Liviu Movileanu (Syracuse University) for encouraging my love for lipids and engraving the phrase “data will make you powerful!” into my young scientific mind.

I am grateful for the support of many along the way. I am thankful to my parents Olga and Robin Fischer for giving me a gift of life and being positive force in my life. I am forever grateful to James Mastroianni for his unconditional love and being the voice of reason for the last decade. My dear friends Michael Chapman, Mary Godec and Jamie Jensen for walking by my side during the last few years and keeping me sane and hopeful during times of internal doubt and for all shared memories. Mary Godec for being a friend that one can only hope for to meet along the way. Michael Chapman, you are an internal light and I am grateful for your support. Jamie Jensen, you are a strong woman. I am grateful for John O’Leary for his positive presence.

I can’t imagine my life without Mishka Eve, for being my loyal companion and the best dog in the world. Bridget Rigas and Alejandro Garson for being my housemates and dear friends, and sharing their beautiful home with me, feeding me on many occasions and brightening up my evenings. I am forever in love with their daughters Inez and Eloise for teaching me a few things

along the way about motherhood.

I am grateful for all who walked along my side, by my side, and who parted their ways. Each of you had taught me a lesson about life, science, friendship, and love.

## TABLE OF CONTENTS

BIOGRAPHICAL SKETCH.....	v
DEDICATION .....	vi
ACKNOWLEDGMENTS.....	vii
TABLE OF CONTENTS .....	ix
LIST OF FIGURES.....	xiii
LIST OF TABLES .....	xiv
LIST OF ABBREVIATIONS .....	xv
TABLE OF CONTENTS.....	ix
LIST OF FIGURES .....	xiii
LIST OF TABLES .....	xiv
<b>CHAPTER 1 Introduction .....</b>	<b>1</b>
1.1 Overview.....	1
1.2 Lipids relevant to this work .....	2
1.3 PUFAs.....	4
1.4 Lipid bilayer phases relevant to this work .....	5
1.5 Functional heterogeneity in cell plasma membranes .....	6
1.6 Model membrane studies .....	9
1.7 Phase diagrams of lipid mixtures .....	13
1.8 Type II ternary mixtures: macroscopic liquid domains .....	14
1.9 Type I ternary mixtures: nanoscopic liquid domains.....	15
1.10 Modulated phases in 4-component mixtures .....	16
1.11. Toward a better raft model.....	16
1.12 Key results .....	17
1.12.1 Modulated phases in 4-Component DSPC/DOPC/POPC/Chol.....	17
1.12.2 Phase Diagram of a 4-Component Lipid Mixture: DSPC/DOPC/POPC/Chol .....	18
1.12.3 Phase Diagram of a Polyunsaturated Lipid Mixture: BSM/SDPC/Chol .....	18
References.....	20
<b>CHAPTER 2</b>	
Control of a Nanoscopic-to-Macroscopic Transition: Modulated Phases in 4-Component DSPC/DOPC/POPC/Chol Giant Unilamellar Vesicles .....	30
2.1 Abstract.....	30
2.2 Materials and methods .....	30
2.2.1 Sample preparation and microscopy .....	31

2.3 Results.....	32
References.....	43
Supplemental Materials .....	45
2.S.1 Theory.....	45

## CHAPTER 3

Phase Diagram of a 4-Component Lipid Mixture: DSPC/DOPC/POPC/Chol.....	49
3.1 Abstract .....	49
3.2 Introduction.....	49
3.3 Materials and Methods.....	52
3.3.1 Materials .....	52
3.3.2 Terminology.....	53
3.4 FRET.....	55
3.5 GUV imaging.....	56
3.5.1 GUVs preparation by electroswelling.....	56
3.5.2 Fluorescence microscopy.....	56
3.5.3 Critical point investigation and percolation map.....	57
3.6 Constructing 4-component phase diagrams .....	58
3.7 Results.....	58
3.7.1 2-dye FRET: DHE → BoDIPY-PC .....	58
3.7.2 3-dye FRET: TOE → BoDIPY-PC → C12:0-DiI .....	62
3.8 Microscopy of GUVs.....	67
3.8.1 Phases observed by GUVs.....	67
3.8.2 Percolation map and critical points.....	68
3.9 Discussion.....	69
3.9.1 Tour of the quaternary phase diagram .....	69
Overview of DSPC/DOPC/POPC/chol phase diagram .....	69
3.9.2 4-component regions.....	71
3.9.2.1 Liquid + gel coexistence, $L_d + L_{\beta}(\beta')$ , region 1 .....	71
3.9.2.2 Gel [ $L_{\beta}(L_{\beta}')$ ], region 2 .....	72
3.9.2.3 Liquid-ordered + gel coexistence, $L_o + L_{\beta}$ , region 3 .....	72
3.9.2.4 3-phase coexistence, $L_d + L_o + L_{\beta}$ , region 4 .....	73
3.9.2.5 Liquid-liquid coexistence, $L_d + L_o$ , region 5.....	73
3.9.2.6 One phase varying continuously from $L_d$ to $L_o$ , region 6.....	79

3.9.2.7 Coexisting cholesterol monohydrate crystals and a cholesterol-saturated Lo phase, region 7 .....	79
3.9.3 Some phase transitions might not be first-order .....	80
3.9.4 Maximum cholesterol solubility in L $\beta$ .....	80
3.9.5 Location of the region of modulated phase domains .....	81
3.10 Summary .....	82
References .....	84
Supplemental Materials .....	81

## CHAPTER 4

Phase Diagram of a Polyunsaturated Lipid Mixture: BSM/SDPC/Chol .....	90
4.1 Abstract .....	90
4.2 Introduction .....	90
4.3 Materials and Methods .....	94
4.3.1 Materials .....	94
4.3.2 Control for PUFA lipid breakdown .....	95
4.3.2.1 Control for photooxidation and light-induced phase separation .....	96
4.3.3 Terminology .....	97
4.3.4 FRET, DHE $\rightarrow$ BoDIPY-PC .....	98
4.3.5 GUV imaging .....	99
4.3.5.1 GUVs preparation by gentle hydration .....	99
4.3.5.2 GUVs preparation by electroswelling .....	99
4.3.6 Fluorescence microscopy .....	100
4.3.7 Critical point investigation and percolation map .....	101
4.4 Results .....	101
4.4.1 FRET, DHE $\rightarrow$ BoDIPY-PC .....	101
4.4.2 Microscopy imaging on GUVs .....	105
4.4.2.1 Phases observed on GUVs .....	105
4.4.2.2 Upper boundary determination .....	105
4.4.2.3 Region of modulated phase domains .....	109
4.4.2.4 Critical point investigation and percolation map .....	111
4.4.3 GUVs formed by electroswelling .....	111
4.5 Discussion .....	112
4.5.1 Description of ternary phase diagram .....	112

4.5.2 Phase regions .....	114
4.6 Summary .....	120
Supplemental Materials .....	121
References .....	128
<b>APPENDIX</b> .....	137
Synthesis of a novel phosphorescent lipid-probe analog and measurement of its phosphorescence signal in liposomes. ....	137
A.1 Introduction .....	137
A.2 Data analysis and connection to models .....	139
A.3 Material and Methods .....	140
A.4 Results .....	142
A.5 Discussion and future directions .....	142
References .....	147

## LIST OF FIGURES

Figure 2.1	Modulated phases occur at $\rho = 15 - 25\%$ as POPC is replaced.....	34
Figure 2.2	GUV patterns as POPC is replaced by DOPC.....	35
Figure 2.3	DIC shows the same pattern as does fluorescence.....	37
Figure 2.4	Different fluorescence microscopies show similar patterns.....	37
Figure 2.5	Phase patterns change with Lo area fraction P.....	38
Figure 2.6	DIC images of a GUV without probe.....	40
Figure 2.7	GUV morphologies imaged with DIC.....	41
Figure 2.8	Complementarity of fluorescence and DIC images.....	42
Figure 2.9	Cross section of the bilayer showing the electrostatic.....	47
Figure 2.10	Log plot of the potential in the headgroup region.....	48
Figure 3.1	Compositional trajectories (dashed lines) T1-T6.....	59
Figure 3.2	Upper boundaries of the Ld + Lo region change smoothly.....	60
Figure 3.3	Upper-RHS boundaries of the Ld + Lo region change smoothly.....	61
Figure 3.4	RHS boundaries along T3 are precisely detected.....	65
Figure 3.5.	All RHS phase region boundaries shift smoothly.....	66
Figure 3.6	GUV images identify phase regions.....	67
Figure 3.7	Percolation maps enable finding critical points.....	68
Figure 3.8	The four faces of the DSPC/DOPC/POPC/chol tetrahedron.....	70
Figure 3.9	Tetrahedral phase diagram of DSPC/DOPC/POPC/chol.....	71
Figure 3.10	Location of RHS boundaries along T4.....	74
Figure 3.11	Location of RHS boundaries along T5.....	75
Figure 3.12	Location of RHS boundaries along T6.....	76
Figure 3.13	Gibbs Triangles at intermediate $\rho$ slices.....	77
Figure 3.14	Anaglyph image for DSPC/DOPC/POPC/chol phase diagram.....	78
Figure 3.S6	Schematic representation of the three dye FRET experiment.....	84
Figure 3.S7	Reduction of sensitized dye B emission.....	86
Figure 3.S8	Simulated $F_B^{Aex}$ trajectory data corresponding to model curves.....	88
Figure 4.1	Representative FRET trajectories (dashed lines) used.....	103
Figure 4.2	Modulated phase patterns are observed.....	104
Figure 4.3	The $\rho$ values for the modulated phase windows.....	106
Figure 4.4	Percolation threshold study at $\rho = 1$ .....	107
Figure 4.5	Critical point investigation and boundaries determined.....	108
Figure 4.6	Phase diagram BSM/SDPC/Chol.....	112
Figure 4.7	Electroswelling produces expanded boundaries.....	113
Figure 4.8	Locating the LHS boundary at zero cholesterol.....	114
Figure 4.S1	GUVs of BSM/SDPC/Chol within Ld + Lo phase coexistence.....	123
Figure 4.S2	Complementarity of C12:0 DiI and naphthopyrene.....	124
Figure 4.S3	Slow cooling time needed.....	125
Figure A.1	Total synthesis reaction.....	145
Figure A.2	10 $\mu$ M erythrosin em spectra, ex 500nm.....	146
Figure A.3	Circular domain showing lifetime ho and hd.....	146

## LIST OF TABLES

Table 2.1	Shows the count distribution of three main GUV morphologies.....	35
Table 3.1	<sup>(a-f)</sup> Coordinates for boundaries for all $\rho$ values along T1-T6.....	62
Table 4.1	Percentage of GUVs with main observed morphologies.....	110

## LIST OF ABBREVIATIONS

BoDIPY-PC	2-(4,4-difluoro-5,7-dimethyl-4-bora-3a,4a-diaza-s-indacene-3-pentanoyl)-1-hexadecanoyl-sn-glycero-3-phosphocholine
BSM	sphingomyelin derived from porcine brain
C12:0-DiI	1,1'-didodecyl-3,3',3'-tetramethylindocarbocyanine perchlorate
C20:0-DiI	1,1'-dieicosanyl-3,3',3'-tetramethylindocarbocyanine perchlorate
Chol	cholesterol
DHA	docosahexaenoic acid
DHE	ergosta-5,7,9(11),22-tetraen-3 $\beta$ -ol
DLPC	1,2-dilauroyl-sn-glycero-3-phosphocholine
DMPC	1,2-dimyristoyl-sn-glycero-3-phosphocholine
DOPC	1,2-dioleoyl-sn-glycero-3-phosphocholine
DPhPC	1,2-diphytanoyl-sn-glycero-3-phosphocholine
DPPC	1,2-dipalmitoyl-sn-glycero-3-phosphocholine;
DSPC	1,2-distearoyl-sn-glycero-3-phosphocholine
ESM	sphingomyelin derived from eggs
FRET	Förster resonance energy transfer
GPMV	giant plasma membrane vesicle
GUV	giant unilamellar vesicle
Ld	liquid-disordered phase
LHS	left hand side refers to left side of phase diagram
Ld	liquid-disordered phase
Lo	liquid-ordered phase
MD	molecular dynamic

NMR	nuclear magnetic resonance
PC	phosphatidylcholine
PE	phosphatidylethanolamine
PM	plasma membrane
POPC	1-palmitoyl-2-oleoyl- <i>sn</i> -glycero-3-phosphocholine
PUFA	polyunsaturated fatty acid
REE	region of enhanced FRET efficiency
RHS	right hand side; refers to right side of phase diagram
RRE	region of reduced FRET efficiency
RSE	rapid solvent exchange
SAE	stimulated acceptor emission
SDPC	1-stearoyl-2-docosahexaenoyl- <i>sn</i> -glycero-3-phosphocholine
SM	sphingomyelin
SOPC	1-stearoyl-2-oleoyl- <i>sn</i> -glycero-3-phosphocholine
SSM	stearoyl SM; PC, phosphatidylcholine
TLC	thin-layer chromatography
TOE	Trp-Oleoyl Ester, N-oleoyl-dl-tryptophan ethyl ester

# CHAPTER 1

## 1.1 Overview

Nonrandom mixing of lipids and proteins in the plasma membrane plays an important role in many cellular processes, including immune signaling, protein sorting, endocytosis, and virus entry and exit, yet the mechanisms governing the coalescence of these small domains are still not completely understood. Functional domains (“lipid rafts”) that arise from nonrandom mixing of membrane components are believed to be important in governing the spatial organization of lipids and proteins. Model systems comprising chemically simplified lipid mixtures have played a central role in studies aimed at elucidating the mechanisms responsible for forming and regulating the size and lifetime of membrane domains.

In this study we report the first solved phase diagram for the four-component mixture DSPC/DOPC/POPC/Chol (distearoylphosphatidylcholine/ dioleoylphosphatidylcholine/1-palmitoyl,2-oleoylphosphatidylcholine/cholesterol), which exhibits a domain size transition from nanoscopic to macroscopic, including a regime of spatially modulated domains within the region of coexisting liquid-disordered (Ld) and liquid-ordered (Lo) phases. I also describe a novel FRET method used to determine boundaries. This phase diagram clearly shows that all phase boundaries determined for the 3-component mixture containing DOPC transition smoothly into the boundaries for the 3-component mixture containing POPC, which has nanoscopic phase domains of Ld + Lo. Together, our studies show that cells could control domain size and morphology by merely changing lipid composition.

Phospholipids having a polyunsaturated acyl chain are abundant in biological membranes, but their behavior in lipid mixtures is difficult to study. In this work we elucidate the nature of

such mixtures with this report of the first ternary phase diagram containing the polyunsaturated lipid SDPC in mixtures of BSM/SDPC/Chol (brain sphingomyelin/1-stearoyl-2-docosahexaenoyl-sn-glycero-3-phosphocholine/cholesterol). These mixtures show macroscopic Ld + Lo phase separation, with phase boundaries determined by FRET and by fluorescence microscopy imaging of giant unilamellar vesicles (GUVs). Surprisingly, SDPC mixes with BSM/Chol similarly to how DOPC and POPC mix with BSM/Chol. In addition, modulated phases are observed within the Ld + Lo liquid-liquid immiscibility region upon addition of fourth component POPC. We find mixtures of BSM/SDPC/POPC/Chol to exhibit nanoscopic Ld + Lo domains over a very large volume of composition space.

In this work we have successfully accomplished the following goals: 1) solved the first ternary phase diagram containing a PUFA lipid; 2) solved the first phase diagram for a four-component lipid mixture, including developing a new FRET method for accurate location of boundaries; and 3) synthesized a novel phosphorescent lipid-probe analog.

## **1.2 Lipids relevant to this work**

The three relevant classes of lipids we highlight in this work include glycerophospholipids, sterols, and sphingolipids. Lipids are amphiphilic molecules and they consist of a hydrophobic acyl chains and hydrophilic headgroup. Lipids are classified according to chain lengths, degree (and location) of unsaturation, and headgroup. The glycerophospholipids have a 3-carbon glycerol backbone. The hydroxyl groups at the C1 and C2 positions form ester bonds to the fatty acid (acyl) chains, and the C3 position is bonded to a phosphate group. The sphingolipids are derivatives of the lipid sphingosine. Unsaturated lipids are defined by having one or more double bonds in acyl chain. A fatty acid chain is monounsaturated if it contains one double bond, and polyunsaturated

if it contains more than two double bonds.

The plasma membrane (PM) contains 30-40 mole% of the sterol cholesterol [1]. Different conceptual models have been proposed to explain the nonideal lipid–lipid interactions. Examples include the condensed-complexes model [2, 3], the superlattice model [4] and the umbrella model [5]. The condensed-complexes model explains the condensation effect by assuming that cholesterol induces the reversible formation of a stoichiometric complex. The cholesterol molecule consists of a tetracyclic ring structure with a hydroxyl group at one end and a short hydrocarbon tail at the other. In membranes the hydroxyl group usually sits just below the surface while the long molecular axis extends toward the interior, lining up approximately parallel to the lipid chains [6].

The lipids used in this study have been chosen to represent lipids found in the outer leaflet of mammalian plasma membranes. Low-melting (low-T<sub>m</sub>) lipids in the outer leaflet are fluid at ambient temperature, and commonly used low-T<sub>m</sub> lipids for this work are DOPC, POPC, and SDPC. High-T<sub>m</sub> lipids, such as BSM and DSPC used in current study, undergo a transition from gel to fluid phase around (or above) physiological temperatures. The two phospholipids used in this study, DOPC and DSPC, each have two 18-carbon acyl chains and a choline headgroup. DSPC has two completely saturated acyl chains. DOPC on the other hand has a double bond in each of its acyl chains, and consequently has a much lower melting transition temperature. DOPC is not naturally occurring in cell membranes, however it is often used in model systems for its stability and for inducing macroscopic Lo+Ld phase separation.

Cholesterol is a naturally occurring lipid that has high abundance in biological membranes. Sterols and sphingolipids have an important role in membrane structure and have been associated with regulation of membrane trafficking. Cholesterol has been implicated as influencing

permeability and fluidity of membranes both *in vivo* [7] and *in vitro* [8].

### 1.3 PUFAs

In retinal rod outer segment disk membranes DHA comprises up to 50% of the total lipid, with this high percentage required for optimal Rhodopsin function [9-11]. DHA is also found at high concentrations in certain other membranes, including synaptosomes [12] and sperm [13]. The importance of DHA and PUFAs for human health has been studied [14-16], as well as spectroscopic studies [17-19], and studies of PUFA effects on membrane properties [20-29]. PUFAs seem to have a weaker interaction with cholesterol compared with saturated or monounsaturated acyl chains [30]. A relatively low solubility of cholesterol in PUFA-containing membranes was measured using both X-ray diffraction and solid-state  $^2\text{H}$  NMR [31-39]. It has been proposed [32, 34] that DHA could be directly involved in inducing lateral phase separations into DHA-rich/cholesterol-poor and DHA-poor/cholesterol-rich lipid domains.

Despite the clear importance of DHA-containing lipids such as SDPC, SDPE, PDPC, and PDPE, only a very limited number of PUFA-containing compositions have been examined. The vast majority of studies conducted on DHA-containing lipids have focused on only a few sample compositions, with one common ratio being 1/1/1 = DHA-containing lipid/SM/Chol, with the DHA-containing lipid being SDPC, SDPE, PDPC or PDPE [41-43]. Mixing behavior over all possible compositions of these three-component mixtures, especially the regions of immiscibility, can be described by use of a triangular phase diagram.

## 1.4 Lipid bilayer phases relevant to this work

Glycerophospholipids and sphingolipids form micelles or bilayer structures in the presence of water. In bilayers, several different types of lipid phases can form, depending on the conformational and positional orders of the lipids and the chemical structure of the headgroup and the temperature and the presence of other species in a mixture. The 2D spatial correlation between lipids within the lipid bilayer is described by positional order. Conformational order refers to the ratio of *trans* to *gauche* conformers and describes the order of the hydrocarbon chains. Positional and conformational orders are the fundamental parameters in determining the phase behavior of a given lipid at a given temperature [44]. The three lamellar phases that will be discussed in this work are differentiated by order. The thermotropic phases found in pure lipids are the liquid crystalline ( $L_o$  and  $L_d$ ) and the gel (solid or  $L_\beta$ ) phase. Bilayers that have both high conformational and positional orders are in the gel phase ( $L_\beta$ ), or solid ordered. In the gel phase the acyl chains pack regularly and tightly, with chains extended in *all-trans* conformations [45]. Fluid phases lack positional order. Liquid-disordered phase ( $L_d$ ) describes low positional and conformational orders. Liquid-ordered phase ( $L_o$ ) can exist when sterols (cholesterol for example) are incorporated into the bilayer. In such a phase, the acyl chains of phospholipids are forced to straighten out and assume more *trans* conformations, in order to allow the headgroups of phospholipids to shield the cholesterol from the exposure to water outside the bilayer. Lipid headgroups act as “umbrellas” to shield the hydrophobic cholesterol; the umbrella model was proposed to describe this [5]. The  $L_o$  phase allows for a high rate of lipid translational diffusion (similar to the  $L_d$  phase), and despite the high conformational order, end result is a liquid phase high in acyl chain order. The addition of cholesterol is believed to decouple the packing and

conformational order in the gel state and in the gel-to-Ld chain melting phase transition [46]. Below the main chain-melting transitional temperature (or for saturated lipids in the gel state) it disrupts lateral packing. Above the chain-melting transition (or for unsaturated lipids in the Ld phase) it imposes an all-trans conformational order. The Lo phase is thought to be of biological relevance and that is often correlated to detergent resistant membranes (DRM), although this correlation between real cell membranes and model systems is disputed.

### **1.5 Functional heterogeneity in cell plasma membranes**

The plasma membrane is a quasi-two dimensional barrier surrounding the cell, providing a controlled environment for the function of its organelles. These membranes are both protective barriers, separating life from death for the cell, and participate in a variety of cellular processes such as intracellular trafficking [47, 48] viral assembly and exit [49] and lipid/protein sorting [50]. Understanding these mechanisms has motivated many researchers to investigate lipid–cholesterol interactions in detail. Because a membrane can be seen as a 2D liquid, a first estimate of how the area per molecule would change upon the addition of cholesterol would be to assume ideal mixing, where the area per molecule is simply a weighted average of the pure-components areas. In 1925 Leathes showed that, instead of ideal mixing, one observes a striking nonideal behavior [51]. This nonideal behavior is called the condensing effect [52] because the area per molecule is much lower compared with ideal mixing. Because changes in the structure of the membrane may have important consequences for the functioning of proteins [53], it is important to have a better molecular understanding of the cholesterol-induced changes. The landmark fluid mosaic model was proposed in 1972, and membrane lipids were depicted as a passive and fluid “sea” of nondescript molecules, the uniform matrix in which the transmembrane and peripheral proteins

diffuse and reside [54]. Over the next 40 years, this notion underwent a substantial transformation that still continues to evolve to this day. What is now believed is that nonrandom mixing of lipids and proteins contributes to lateral heterogeneities in the PM that are important in many cellular processes, though the exact mechanisms are still not completely understood.

Biological membranes are vastly complex structures, with hundreds of lipid components and thousands of different proteins. The fluid mosaic model downplayed the importance of lipid diversity in order to allow more spotlight for proteins residing within the plane of the membrane. The appreciation that lipids can play a very important role in functional and organization of plasma membrane came from many decades of studies. Simons and van Meer, reported on lipid sorting into apical and basolateral areas of epithelial cell PM. Lateral inhomogeneities in the lipid compositions of the plasma membrane were implicated in membrane organization [55]. Brown and Rose found specific proteins localized with Chol and sphingolipids in detergent-resistant membrane domains [56]. The sorting of the glycosphingolipids and cholesterol to the trans-Golgi membranes and apical PM of epithelial cells led to inquiry regarding the sorting and preferential association of specific lipid-anchored proteins with “raft” lipids. This question led to development and use of a detergent-resistance assay, where cell membranes treated with cold detergent and fractionated through a sucrose gradient. The properties of DRMs were also examined in model systems, however, the reliability and accuracy of DRM studies has been questioned (discrepancies of results based on detergent and temperature used and fundamental mixing of lipids and detergents). It was shown that DRMs are not the same as lipid rafts in cell plasma membranes [57] and the need for other methods for identification and characterization of functional domains in cell PM continues.

More evidence of colocalization of proteins with certain lipids emerged [58-60]. The lipid

raft hypothesis was proposed, suggesting that the functional domains within the PM (with compositions that differ from the bulk “sea” of lipids) could influence the functions and localization of proteins [61]. Lipid “rafts” [61] have been proposed to play a role in many cellular processes, including immune cell signaling, the area of extensive research. When FcεRI receptors are crosslinked by IgE, they form a more stable patch on the PM outer leaflet, which recruits Lyn kinases to initiate phosphorylation of the receptors on the inner leaflet, with phosphatases being excluded from this patch. Cholesterol depletion disrupted the co-localization of crosslinked receptors and Lyn, and as a result caused a loss of Lyn-mediated phosphorylation [62, 63]. This indicated that specialized compartments (distinct in composition from the rest of the bilayer) are formed in the PM based on preferred associations between particular lipids and proteins.

One challenge arises from the ambiguous definition for lipid “rafts”. Depending on the system of study and technique used, definitions of “rafts” have varied extensively. Rafts are sometimes considered to be a heterogeneous assembly of domains with varied temporal stability and with diverse lipid and protein compositions. One definition of rafts introduced in 2006 became widely used, “Lipid rafts are small (10-200 nm), heterogeneous, highly dynamic, sterol- and sphingolipid-enriched domains that compartmentalize cellular processes. Small rafts can sometimes be stabilized to form larger platform through protein-protein and protein-lipid interactions” [64]. Rafts are considered by some researchers to be a heterogeneous assembly of domains with varied temporal stability and with diverse lipid and protein compositions.

Nanosopic domains are detected *in vivo* in plasma membranes by methods that are sensitive to small length scales, such as FRET [65, 66], FRAP [67], electron spin resonance (ESR) spectroscopy [68], and stimulated emission depletion (STED) far-field fluorescence nanoscopy [69]. In particular, nanodomains that have L<sub>d</sub> and L<sub>o</sub> characteristics have been detected with FRET

[65] and ESR [67] in live cells. Thus, lipid ‘raft’ domains, enriched in cholesterol and sphingolipids, together with non-raft domains, seem to be significant types of lateral heterogeneities in biological membranes [67, 70-73]. In cells, the range of size scales of any phase domains, as well as domain shape and connectivity, are not known. Furthermore, it is quite possible that membranes of living cells use spatial organization on multiple length scales, rather than one special size.

## **1.6 Model membrane studies**

Starting in the 1960s studies on such model systems established that “simple” lipid mixtures can display an astonishingly rich set of behaviors, including phase coexistence driven by the immiscibility of unlike lipid chains. So how do we study complex lipid phase behaviors? Understanding the behavior of any material benefits from knowing which phases are present. Experiments with membranes, both naturally complex membranes as well as chemically simplified models, can be designed to detect information about phases, including cases where these phases coexist. Phase diagrams for three-component lipid mixtures can show rich behavior, or they can be featureless in composition space.

In this study, we focus on one specific subset of complex membrane behaviors: lateral heterogeneity based on lipid-only interactions in multicomponent bilayer mixtures. The motivation for examining such mixtures is the apparent connection between the coexistence of Ld + Lo phases observed in some model lipid-only bilayers, and the properties of lipid rafts observed in some cellular membranes. This connection propelled the study of bilayer mixtures in the previous two decades. The purpose of solving complete phase diagrams is to understand whether

the actual lipid mixtures found in cell membranes could yield bilayer phase coexistence, and changes in which phases are stable. The minimal systems that maintain biological relevance, yet are suitable for comprehensive study, contain both high-melting (high-T<sub>m</sub>) and low-melting temperature (low-T<sub>m</sub>) lipids and cholesterol [89], because the outer leaflet of animal cell plasma membranes contains these three classes of lipids. A rich phase behavior is found in these systems, including a large region of coexisting ordered- and disordered-liquid phases at biologically relevant cholesterol concentrations.

Simple lipid mixtures can reveal several different compositional regions of phase coexistence. However, this doesn't make such systems *a priori* good models for cell plasma membranes. Often such mixtures are chosen for study not because the lipid components are the best representative molecules from a biological perspective, but rather because they allow us to easily detect some key phase regions and phase boundaries. Measuring accurate phase boundaries is an important practical consideration, because it provides us with an opportunity to apply equilibrium thermodynamics of mixing of components to understand other physical properties of the system, such as exactly which phase compositions coexist, necessary for measuring phase bending energies, and partition coefficient measurements of proteins or lipids between coexisting phases. Solved phase diagrams also enable the analysis by small angle neutron scattering (SANS) of the size of nanodomains. For example, line tension is an important parameter that we discuss further in Section 1.11 and phase diagrams must be resolved. In order to measure bending energies in a system, we must know the fractions of each phase present and we can only obtain this information accurately (using Lever rule) by knowing the boundaries of the region. Well-resolved phase boundaries are a must, since phase boundaries represent the link between the thermodynamic data and a model that describes how the components are distributed.

Taking the importance of phase diagrams yet a step further, simulation studies such as Monte Carlo and molecular dynamics (MD) heavily rely on knowing the thermodynamics of a lipid composition under investigation. And based on phase diagram data and on models of size and morphology of coexisting domains, computer simulations may enable us to discover which interactions between lipids and proteins govern membrane behavior. One use of Monte Carlo simulations is to construct a model for any given mixture of lipids (and proteins), describing the clustering, ordering, and phase separation as a function of composition. This is the very subject of the thermodynamics of liquid mixtures, and we want to have a clear picture of the nonrandom mixing on size scales from nanoscopic to macroscopic.

Below we discuss two useful methods of investigating phase separation in model systems: FRET and imaging of GUVs.

### **1.6.1 FRET**

A bilayer probe's signal is often very sensitive to its immediate (*i.e.*, nearest-neighbor) lipid environment. Differences in hydrocarbon chain order and packing can influence probe dynamics and can result in significant differences in probe spectra in different bilayer phases. FRET is a non-radiative process that takes place between an excited donor molecule (D) and the ground-state acceptor molecule (A) over a range of distances, typically 10-100 Å [74-76]. The FRET efficiency is strongly dependent on the (D)-(A) distance and is characterized by  $R_0$  (Förster critical radius), which is a unique parameter for each (D)-(A) probe pair. This distribution is strongly affected by partitioning of donor and acceptor between the coexisting phase domains [74, 75], as well as the size and morphology of such domains [77, 78]. As a general rule, FRET cannot reliably detect phase domains smaller than the Förster distance ( $R_0$ ) of the donor/acceptor pair [77], which by

definition is the distance at which energy transfer between a donor/acceptor pair is 50% efficient.

The FRET method allows unambiguous determination of phase boundaries by visual examination. FRET can be used to construct a phase diagram with few artifacts and with a compositional resolution of  $\sim 2\%$ , but a large number of samples are required. FRET experiments are cuvette-based, enabling sample preparation by use of rapid solvent exchange (RSE), which minimizes the lipid demixing, especially of cholesterol [74]. RSE also allows the use of an inert atmosphere at all stages of sample preparation, minimizing oxygen-induced artifacts that are a significant problem in mixtures containing PUFA lipids (Chapter 4).

### **1.6.2 Fluorescence imaging of GUVs**

Since 1999, giant (10-100 micron diameter) unilamellar vesicles (GUVs) have proven to be useful tools for the visualization of bilayer phases and have been widely used to study phase behavior in model membranes [79-86]. Fluorescence imaging of GUVs (using epifluorescence, confocal, or two-photon microscopy) provides a decisive determination of phase coexistence, and has been used extensively in model membrane studies of phase coexistence [84, 87-93]. Fluorescence imaging of GUVs mimicking the composition of mammalian plasma membrane, revealed stable liquid phase domains resolvable by fluorescence microscopy and became one of the main tools available to study model lipid systems. It allowed for precise and reproducible detection of coexisting phases at a known composition of components. The groundbreaking work to understand the fundamental mechanisms responsible for liquid immiscibility was undertaken by Korlach et al. and Dietrich et al., which also promoted additional efforts to understand the phase behavior of three-component lipid mixtures [84, 87], with the first reports on liquid-liquid immiscibility in ternary model systems in 1996 [94].

As with any experimental technique, there are limitations and potential artifacts involved with fluorescence imaging of GUVs. Domains smaller than the optical resolution limit ( $\sim 200$  nm) are not detected, and it is now known that many biologically important model systems have domains below the optical resolution. Another limitation is the relatively low compositional resolution of  $\sim 5\%$  that can be achieved with this method. Other GUV limitations are the potential for electrolysis-induced artifacts associated with the electroswellling method and indium tin oxide electrodes, including oxygen- and free radical-induced artifacts [85, 86] (discussed in detail in Chapter 4). These artifacts can be avoided by preparing GUVs by gentle hydration method (discussed in detail in Chapter 4). The gentle hydration method for making GUVs was first introduced by Reeves and Dowben [95], and significantly modified by Akashi et al. [96]. In Feigenson's research group, we have developed protocols for minimizing light-induced domain artifacts, including (but not limited to) using very low probe concentrations and low intensity excitation light, and searching for vesicles using brightfield illumination [97], and the possibility of a compositional distribution within the GUV preparation was addressed [98, 99].

### **1.7 Phase diagrams of lipid mixtures**

Throughout the early 2000s, great effort was placed into solving the phase diagrams of three component mixtures mimicking the plasma membrane composition. It is convenient to organize the discussion around the important observation that for mixtures consisting of a low- $T_m$  lipid, a high- $T_m$  lipid, and cholesterol, either one or three phase coexistence regions are observed in microscopy experiments. Feigenson has classified these systems as exhibiting Type I or II behavior, to indicate the number of macroscopic coexistence regions [100]. For both Types I and II,  $L_d + L_\beta$  coexistence is visible by microscopy at low cholesterol concentrations. Type I mixtures

have only  $L_d + L_\beta$  coexistence region visible. Type II mixtures have  $L_d + L_\beta$ ,  $L_d + L_o$ , and  $L_d + L_o + L_\beta$  regions visible by fluorescence microscopy (macroscopic phase separations). Despite these observable macroscopic differences, all such mixtures seem to have the same coexistence regions when examined by techniques such as FRET and ESR, sensitive to nanoscopic phase separations.

### **1.8 Type II ternary mixtures: macroscopic liquid domains**

Type II mixtures are reported for low- $T_m$  lipids that are not abundant in mammalian cell membranes. Lipids such as DOPC or DPhPC have very low- $T_m$  compared to the biologically abundant low- $T_m$  lipids such as POPC and SOPC. Type II phase diagrams are observed for mixtures including: DPPC/DPhPC/Chol [82]; DPPC/DOPC/Chol [102, 75, 104, 93], DSPC/DOPC/Chol [79, 105]; SSM/DOPC/Chol [107]; PSM/DOPC/Chol [81, 106]; BSM/DOPC/Chol [108, 109] and ESM/DOPG/Chol [110].

The general characteristics of a Type II phase diagram are exemplified by the phase diagram of DSPC/DOPC/Chol [79]. At low cholesterol concentrations ( $\sim 0$ – $10$  mol%), a macroscopic  $L_d + L_\beta(\beta')$  region is observed by GUV imaging. Phase domains exhibit irregular, straight-line and edged features, consistent with a solid phase. At intermediate cholesterol concentrations, GUV images of  $L_o + L_d + L_\beta$  coexistence transition to a mixed appearance of rounded and linear features, including in some cases three distinct fluorescence intensities. At even higher cholesterol concentrations, the irregularly shaped domains disappear in the GUV images, yielding to the appearance of two coexisting fluid phases. A more recent variation of the FRET experiment utilizing three probes indicates that the  $L_d + L_o$  region extends to lower concentrations of DOPC (Chapter 3), indicating a narrow region of nanoscopic domains near the binary

DSPC/Chol axis that are not observed with microscopy. Similar observations have been made in SSM/DOPC/Chol. Chapter 3 describes a quaternary phase diagram for DSPC/DOPC/POPC/Chol, which is composed of both type II and type I individual ternary mixtures, making up the faces of the pyramid. Chapter 4 describes a newly solved BSM/SDPC/Chol phase diagram, which is a Type II diagram.

### **1.9 Type I ternary mixtures: nanoscopic liquid domains**

Type I mixtures have only one macroscopic phase coexistence region:  $L_d + L_\beta$ , observed at low cholesterol. The phase behavior of Type II and Type I mixtures is qualitatively identical, i.e. the phase regions are the same but the size of the domains observed is different. Among the small differences was the observation that the upper boundary of  $L_d + L_o$  coexistence occurs at 30 mol% cholesterol for SOPC- and POPC-containing mixtures, rather than at 40% cholesterol for DOPC-containing mixtures.

Feigenson et al undertook the first extensive study of Type I system DPPC/DLPC/Chol, using a combination of techniques sensitive to both macroscopic and nanoscopic phase separations [83]. Heberle et al. used FRET and ESR to examine the mixing behavior of DSPC/POPC/Chol and DSPC/SOPC/Chol [105], which were earlier identified as Type I systems [79]. The phase diagram for BSM/POPC/Chol was solved by Petruzielo et al, which was shown to be a Type I mixture, and as discussed in Chapter 4, is very similar to the BSM/SDPC/Chol phase diagram solved in this work. Other solved Type I mixtures include: PSM/POPC/Chol [111-113]; BSM/POPC/Chol [109, 114]; DSPC/POPC/Chol and DSPC/SOPC/Chol [105]. Type I systems have nanoscopic liquid-liquid immiscibility regions that might resemble phase separation in real cells, where domains have been guessed to be in the nanoscopic range between 20-200 nm [73, 115].

## 1.10 Modulated phases in 4-component mixtures

Both Type II and Type I phase diagrams have the same topology, a central three-phase region joining three two phase regions. It is reasonable to assume that a continuous two-phase Ld + Lo volume should exist within the four component (tetrahedral) space, joining individual Type I and Type II Ld + Lo regions. We asked the following questions: Is the nanoscopic-to-macroscopic transition abrupt, or rather a gradual change? What is the composition dependence of the transition zone? Do lipids control the transition? Chapter 3 discusses our findings in detail.

The first experiments to address these questions examined a volume joining two ternary faces in the Ld + Lo regions of DSPC/DOPC/Chol and DSPC/POPC/Chol and are discussed in Chapter 2 and [116].

## 1.11. Toward a better raft model: transition from macroscopic to nanoscopic domains

Biological membrane phase behavior can be modeled well by mixtures of four lipids, which enables study of Ld + Lo domain size from a few nanometers to many microns that is controlled by composition. Why do we care about the switch of domain size from nano-to-macro? The tens of nanometer scale seems to describe the phase-separated domains in animal cell plasma membranes better than does the micron scale [117-120]. Silvius [121] proposed the presence of nanodomains in a lipid bilayer with compositions mimicking the outer leaflet bilayer. Lipids such as SOPC or POPC, having one saturated sn-1 chain and one monounsaturated sn-2 chain, naturally occur as the most abundant phospholipid species in animal cell membranes. Optical microscopy studies on such lipids in ternary mixtures with cholesterol and a high-melting lipid show uniform membranes [79, 111], yet other methods indicate the presence of lateral heterogeneity [105, 111, 120, 121] invisible to optical microscopy imaging. We have previously reported the presence of

intermediate states that have modulated phase morphology in the 4-component mixture DSPC/DOPC/POPC/Chol [116, 122]. Modulated phase morphology occurs when two liquid phases coexist, if the line tension that drives the minimization of domain perimeter is opposed by a long-range interaction such as bending energy of a curved membrane that acts to break up domains [123, 124].

The surprising complexity observed in the four component DSPC/DOPC/POPC/Chol mixture may have significance for rafts in biological systems. The existence of distinct regimes of nanoscopic and macroscopic, spatially modulated domains might be important organizing principles in plasma membranes. The domain size transition is driven by lipid composition rather than temperature, which may suggest a mechanism by which cells control domain properties including size and morphology.

## **1.12 Key results**

### **1.12.1 Modulated phases in 4-Component DSPC/DOPC/POPC/Chol**

We have found modulated phase morphology in a particular region of composition within the liquid-ordered + liquid-disordered coexistence region in the four-component lipid bilayer mixture DSPC/DOPC/POPC/Chol. By controlling lipid composition, we could see distinct types of modulated liquid-liquid phase morphologies, including linear, irregular, and angular features in giant unilamellar vesicles. We used a combination of confocal, two-photon, wide-field fluorescence, and differential interference contrast microscopies, and used stringent controls to minimize light-induced artifacts. These studies establish that both the size and morphology of membrane rafts can be controlled by the concentration and the type of low-melting lipid in mixtures with cholesterol and a high-melting lipid.

### **1.12.2 Phase Diagram of a 4-Component Lipid Mixture: DSPC/DOPC/POPC/Chol**

We report the first 4-component phase diagram for the lipid bilayer mixture, DSPC/DOPC/POPC/chol(distearoylphosphatidylcholine/dioleoylphosphatidylcholine/1-palmitoyl, 2-oleoylphosphatidylcholine/cholesterol). All phase regions of the 3-component mixture DSPC/DOPC/Chol can be determined unequivocally, with spectroscopic methods and GUV imaging in agreement as to phase boundaries and phase identity. In contrast, the phase diagram of the 3-component mixture DSPC/POPC/Chol shows no visible Ld + Lo domains by optical imaging of GUVs. However, as DOPC is replaced by POPC, phase boundaries determined spectroscopically shift smoothly to new values, with no significant change in the nature of the phase behaviors. These observations are consistent with nanodomains of Ld + Lo in POPC-rich mixtures being phase domains.

With two appropriate 3-component phase diagrams in hand, constructing the 4-component phase diagram that joins them requires a relatively modest effort that can enable a clear definition of the phase region where “modulated phase behavior” occurs.

Some phase boundaries do not show up clearly when examined by conventional fluorescence spectroscopic methods, but can show up distinctly with a new “3-dye method” that makes use of a second FRET acceptor.

### **1.12.3 Phase Diagram of a Polyunsaturated Lipid Mixture: BSM/SDPC/Chol**

Phospholipids having a polyunsaturated acyl chain are abundant in biological membranes, but their behavior in lipid mixtures is difficult to study. Here we elucidate the nature of such

mixtures with this report of the first ternary phase diagram containing the polyunsaturated lipid SDPC in mixtures of BSM/SDPC/Chol (brainsphingomyelin/1-stearoyl-2-docosahexaenoyl-sn-glycero-3-phosphocholine/ cholesterol). These mixtures show macroscopic Ld + Lo phase separation, with phase boundaries determined by FRET and by fluorescence microscopy imaging of giant unilamellar vesicles (GUVs). Surprisingly, SDPC mixes with BSM/Chol similarly to how DOPC and POPC mix with BSM/Chol. In addition, modulated phases are observed within the Ld + Lo liquid-liquid immiscibility region upon addition of fourth component POPC. We find mixtures of BSM/SDPC/POPC/Chol to exhibit nanoscopic Ld + Lo domains over a very large volume of composition space.

## References

- [1] Lodish, H., A. Berk, S.L. Zipursky, P.Matsudaira, D. Baltimore, J. Darnell, Molecular Cell Biology, 5<sup>th</sup> ed., W.H. Freeman and Company, New York, 2004.
- [2] Radhakrishnan A, and McConnell HM. 1999. Condensed complexes of cholesterol and phospholipids. *Biophys J.* 77:1507–1517.
- [3] Radhakrishnan A, Anderson TG, and McConnell HM. 2000. Condensed complexes, rafts, and the chemical activity of cholesterol in membranes. *Proc Natl Acad Sci USA* 97:12422–12427.
- [4] Chong PLG. 1994. Evidence for regular distribution of sterols in liquid-crystalline phosphatidylcholine bilayers. *Proc Natl Acad Sci USA* 91:10069–10073.
- [5] Huang, J. and G.W. Feigenson. 1999. A microscopic model of maximum solubility of cholesterol in lipid bilayers, *Biophys J.* 76: 2142-2157.
- [6] Khelashvili, G., and D. Harries. 2013. How sterol tilt regulates properties and organization of lipid membranes and membrane insertions. *Chem. Phys. Lipids* 169:113–123.
- [7] Emter, R., A. Heese-Peck, A. Kralli. 2002. ERG6 and PDR5 regulate small lipophilic drug accumulation in yeast cells via distinct mechanisms, *FEBS Letters.* 521:57-61.
- [8] Haines T.H. 2001. Do sterols reduce proton and sodium leaks through lipid bilayers? *Progress in Lipid Research.* 40:299-324.
- [9] <http://lipidlibrary.aocs.org/Lipids/complex.html>
- [10] Wiegand R.D., and RE. Anderson. 1983. Phospholipid molecular species of frog rod outer segment membranes. *Exp. Eye Res.* 37:159–173.
- [11] Mitchell D.C., Litman B.J. 1998. Effect of cholesterol on molecular order and dynamics in highly polyunsaturated phospholipid bilayers. *Biophys. J.* 75:896–908.
- [12] Breckenridge W.C., Gombos G., Morgan L.G. 1972. The lipid composition of adult rat brain synaptosomal membranes. *Biochim. Biophys. Acta.* 266:695–707.
- [13] Neill A.R., Masters C.J. 1973. Metabolism of fatty acids by bovine spermatozoa. *J. Reprod.Fertil.* 34:279–287.
- [14] Stillwell W., and SR. Wassall. 2003. Docosahexaenoic acid: membrane properties of a unique fatty acid. *Chem. Phys. Lipids.* 126:1–27.

- [15] Wassall S.R., Stillwell W., 2008. Docosahexaenoic acid domains: the ultimate non-raft membrane domain. *Chem. Phys. Lipids*. 153:57–63.
- [16] Wassall S.R., Stillwell W. 2009. Polyunsaturated fatty acid-cholesterol interactions: domain formation in membranes. *Biochim Biophys Acta*. 1788:24-32.
- [17] Litman, B. J., E. N. Lewis, and I. W. Levin. 1991. Packing characteristics of highly unsaturated bilayer lipids: Raman spectroscopic studies of multilamellar phosphatidylcholine dispersions. *Biochem*. 30: 313–319.
- [18] Paddy, M. R., F. W. Dahlquist, E. A. Dratz, and A. J. Deese. 1985. Simultaneous observation of order and dynamics at several defined positions in single acyl chain using <sup>2</sup>H NMR of single acyl chain perdeuterated phosphatidylcholines. *Biochem*. 24:5988 – 5995.
- [19] Salmon, A., S. W. Dodd, G. D. Williams, J. M. Beach, and M. F. Brown. 1987. Configurational statistics of acyl chains in polyunsaturated lipid bilayers from <sup>2</sup>H NMR. *J. Am. Chem. Soc*. 109:2600 –2609.
- [20] Everts, S., and J. H. Davis. 2000. <sup>1</sup>H and <sup>13</sup>C nuclear magnetic resonance of multilamellar dispersions of polyunsaturated (12:6) phospholipids. *Biophys. J*. 79:885– 897.
- [21] Binder, H., and K. Gawrisch. 2001. Dehydration induces lateral expansion of polyunsaturated 18:0-22:6 phosphatidylcholine in a new lamellar phase. *Biophys. J*. 81 (2): 969-82.
- [22] Separovic, F., and K. Gawrisch. 1996. Effect of unsaturation on the chain order of phosphatidylcholines in a dioleoylphosphatidylethanolamine matrix. *Biophys. J*. 71:274 – 282.
- [23] Huster, D., G. Paasche, U. Dietrich, O. Zschoernig, T. Gutberlet, K. Gawrisch, and K. Arnold. 1999. Investigation of phospholipid area compression induced by calcium-mediated dextran sulfate interaction. *Biophys. J*. 77:879–887.
- [24] Koenig, B. W., H. H. Strey, and K. Gawrisch. 1997. Membrane lateral compressibility measured by NMR and x-ray diffraction. *Biophys. J*. 73:1954 –1966.
- [25] Rawicz, W., K. C. Olbrich, T. McIntosh, D. Needham, and E. Evans. 2000. Effect of chain length and unsaturation on elasticity of lipid bilayers. *Biophys. J*. 79:328 –339.
- [26] D. Huster, K. Arnold, K. Gawrisch. 1998. Influence of docosahexaenoic acid and cholesterol on lateral lipid organization in phospholipid mixtures, *Biochem*. 37:17299– 17308.
- [27] Olbrich, K., W. Rawicz, D. Needham, and E. Evans. 2000. Water permeability and mechanical strength of polyunsaturated lipid bilayers. *Biophys. J*. 79:321–327.

- [28] Shaikh S.R., Cherezov V., Caffrey M., Soni S.P., LoCascio D., Stillwell W., Wassall S.R. 2006. Molecular organization of cholesterol in unsaturated phosphatidylethanolamines: X-ray diffraction and solid state <sup>2</sup>H NMR reveal differences with phosphatidylcholines. *J Am Chem Soc.* 128:5375-83.
- [29] Koubi L., Saiz L., Tarek M., Scharf D, Klein M.L. 2003. Influence of Anesthetic and Nonimmobilizer Molecules on the Physical Properties of a Polyunsaturated Lipid Bilayer. *J. Phys. Chem. B.* 107: 14500-14508.
- [30] Kucerka N., Marquardt D., Harroun T.A., Nieh M.P., Wassall S.R., de Jong D.H., Schäfer L.V., Marrink S.J., Katsaras J. 2010. Cholesterol in bilayers with PUFA chains: doping with DMPC or POPC results in sterol reorientation and membrane-domain formation. *Biochem.* 35:7485-93.
- [31] Brzustowicz, M. R., V. Cherezov, M. Caffrey, W. Stillwell, and S. R. Wassall. 2002b. Molecular organization of cholesterol in polyunsaturated membranes: microdomain formation. *Biophys. J.* 82:285–298.
- [32] Brzustowicz, M. R., V. Cherezov, M. Zerouga, M. Caffrey, W. Stillwell, and S. R. Wassall. 2002a. Controlling membrane cholesterol content. A role for polyunsaturated (docosahexaenoate) phospholipids. *Biochem.* 41:12509–12519.
- [33] Brzustowicz, M. R., W. Stillwell, and S. R. Wassall. 1999. Molecular organization of cholesterol in polyunsaturated phospholipid membranes: a solid state <sup>2</sup>H NMR investigation. *FEBS Lett.* 451:197–202.
- [34] Shaikh, S. R., M. R. Brzustowicz, N. Gustafson, W. Stillwell, and S. R. Wassall. 2002. Monounsaturated PE does not phase-separate from the lipid raft molecules sphingomyelin and cholesterol: role for polyunsaturation? *Biochem.* 41:10593–10602.
- [35] Shaikh, S. R., V. Cherezov, M. Caffrey, W. Stillwell, and S. R. Wassall. 2003a. Interaction of cholesterol with a docosahexaenoic acid-containing phosphatidylethanolamine: trigger for microdomain/raft formation? *Biochem.* 42:12028–12037.
- [36] Shaikh, S. R., A. C. Dumauval, D. LoCascio, R. A. Siddiqui, and W. Stillwell. 2003b. Acyl chain unsaturation in PEs modulates phase separation from lipid raft molecules. *Biochem. Biophys. Res. Commun.* 311:793–796
- [37] Shaikh SR, Locascio DS, Soni SP, Wassall SR, Stillwell W. 2009. Oleic- and docosahexaenoic acid-containing phosphatidylethanolamines differentially phase separate from sphingomyelin. *Biochim. Biophys. Acta.* 178:2421-2426.
- [38] Saiz L., Klein M.L., 2001. Structural properties of a highly polyunsaturated lipid bilayer from molecular dynamics simulations. *Biophys. J.* 81:204–216.

- [39] Shaikh S.R., Brzustowicz M.R., Stillwell W., and S.R. Wassall. 2001. Formation of inverted hexagonal phase in SDPE as observed by solid-state  $^{31}\text{P}$  NMR. *Biochem. Biophys. Res. Commun.* 286:758–763.
- [40] Shaikh S.R., Kinnunb J.J. Lengb X., Williamsb JA., and S.R. Wassal. 2015. How polyunsaturated fatty acids modify molecular organization in membranes: Insight from NMR studies of model systems, *Biochim. Biophys. Acta.* 1848:1, 211–219
- [41] Shaikh S.R., Dumauual A.C., Castillo A., LoCascio D., Siddiqui R.A., Stillwell W., Wassall S.R. 2004. Oleic and docosahexaenoic acid differentially phase separate from lipid raft molecules: a comparative NMR, DSC, AFM, and detergent extraction study. *Biophys J.* 87:1752-66.
- [42] Soni S.P., LoCascio D.S., Liu Y., Williams J.A., Bittman R., Stillwell W., Wassall S.R. 2008. Docosahexaenoic acid enhances segregation of lipids between:  $^2\text{H}$ -NMR study. *Biophys J.* 95(1):203-14.
- [43] Shaikh S.R., Kinnunb J.J. Lengb X., Williamsb JA., Wassal S.R. 2015. How polyunsaturated fatty acids modify molecular organization in membranes: Insight from NMR studies of model systems, *Biochim. Biophys. Acta.* 1848:1, 211–219.
- [44] Nagle, J.F. 1973. Theory of biomembrane phase transitions. *Journal of Chemical Physics.* 58: 252-264.
- [45] Seelig, A., and J. Seelig. 1974. The dynamic structure of fatty acyl chains in a phospholipid bilayer measured by deuterium magnetic resonance. *Biochemistry.* 13:4839-4845.
- [46] Ipsen, J.H. et al. 1987. Phase equilibria in the phosphatidylcholine-cholesterol system, *Biochimica et Biophysica Acta.* 905: 162-172.
- [47] Parton, R. G. and Richards, A. A. 2003. Lipid rafts and caveolae as portals for endocytosis: New insights and common mechanisms. *Traffic.* 4(11): 724-738.
- [48] Rajendran, L. and Simons, K. 2005. Lipid rafts and membrane dynamics. *Journal of Cell Science.* 118(6):1099-1102.
- [49] Ono, A. 2010. Relationships between plasma membrane microdomains and HIV-1 assembly. *Biology of the Cell.* 102(6): 335-350.
- [50] Cao, X., Surma, M. A. and K. Simons. 2012. Polarized sorting and trafficking in epithelial cells. *Cell Research.* 22(5): 793-805.
- [51] Leathes, JB. 1925. Croonian lectures on the role of fats in vital phenomena. *The Lancet.* 205:853–856.
- [52] McConnell, HM, and A. Radhakrishnan. 2003. Condensed complexes of cholesterol and

- phospholipids. *Biochim Biophys Acta Biomembr.* 1610:159–173.
- [53] Ikonen, E. 2008. Cellular cholesterol trafficking and compartmentalization. *Nat Rev Mol Cell Biol.* 9:125–138.
- [54] Singer, S.J. and G.L. Nicolson. 1972. The fluid-mosaic model of the structure of cell membranes. *Science.* 175: 720-731.
- [55] Simons, K. and G. van Meer. 1988. Lipid sorting in epithelial cells, *Biochemistry.* 27:6197-6202.
- [56] Brown, D.A. and J.K. Rose. 1992. Sorting of GPI-anchored proteins to glycolipid-enriched membrane subdomains during transport to the apical cell surface. *Cell.* 68: 533-544.
- [57] Brown, D. A. 2006. Lipid rafts, detergent-resistant membranes, and raft targeting signals. *Physiology,* 21, 430-439.
- [58] Carter, W.G. and S.I. Hakomori. 1981. A new cell surface, detergent-insoluble glycoprotein matrix of human and hamster fibroblasts. *Journal of Biological Chemistry.* 256, 6953-6960.
- [59] Okada, Y. G., Mugnai, EG, Bremer, and Hakomori SI. 1984. Glucosphingolipids in detergent-insoluble substrate attachment matrix (DIAM) prepared from substrate attachment material (SAM): Their possible role in regulating cell adhesion. *Experimental Cell Research.* 155: 448-456.
- [60] Field, K.A., D. Holowka, and B. Baird. 1995. Fc $\epsilon$ RI-mediated recruitment of p53/56(lyn) to detergent-resistant membrane domains accompanies cellular signaling field, *Proceedings of the National Academy of Sciences (USA).* 92: 9201-9205.
- [61] Simons K., and E. Ikonen. 1997. Functional rafts in cell membranes. *Nature.* 387: 569-572.
- [62] Sheets, E.D., D. Holowka, and B. Baird. 1999a. Membrane organization in immunoglobulin E receptor signaling, *Current Opinion in Chemical Biology.* 3: 95-99.
- [63] Sheets, E.D., D. Holowka, and B. Baird. 1999b. Critical role for cholesterol in Lyn-mediated tyrosine phosphorylation of Fc $\epsilon$ RI and their association with detergent-resistant membranes. *The Journal of Cell Biology.* 145: 877-887.
- [64] Pike L.J. 2006. Rafts defined: a report on the Keystone Symposium on Lipid Rafts and Cell Function. *Journal of Lipid Research.* 47:1597-8.
- [65] Sengupta P., Holowka D., and B. Baird. 2007. Fluorescence resonance energy transfer between lipid probes detects nanoscopic heterogeneity in the plasma membrane of live cells. *Biophys. J.* 92:3564–3574.

- [66] Sharma P., Varma R., and S. Mayor. 2004. Nanoscale organization of multiple GPI-anchored proteins in living cell membranes. *Cell*. 116:577–589.
- [67] Meder D., Moreno M.J., Verkade P., Vaz W.L., and K. Simons. 2006. Phase coexistence and connectivity in the apical membrane of polarized epithelial cells. *PNAS*. 103: 329-334.
- [68] Swamy MJ, Ciani L, Ge M, Smith AK, Holowka D, Baird B, and JH Freed. 2006. *Biophys J*. 90(12):4452-65.
- [69] Eggeling C., Ringemann C., and SW. Hell. 2009. Direct observation of the nanoscale dynamics of membrane lipids in a living cell. *Nature*. 457:1159–1162.
- [70] Simons K. Eehalt R. 2002. Cholesterol, lipid rafts, and diseases. *J.Clin. Invest*. 110:597-603.
- [71] Simons K., and E. Ikonen. 1998. Protein and lipid sorting from the trans-Golgi network to the plasma membrane in polarized cells. *Cell and Develop. Biol*. 9:503-509.
- [72] Simons K.Vaz W.L.C. 2004. Model systems, Lipid Rafts, and Cell Membranes. *Biophys. Biomol. Struct*. 33:269-295.
- [73] Simons K., and D. Lingwood. 2010. Lipid Rafts as a Membrane-Organizing Principle. *Science*. 327: 46-50.
- [74] Buboltz, J.T. 2007. Steady-state probe-partitioning fluorescence resonance energy transfer: A simple and robust tool for the study of membrane phase behavior. *Phys. Rev. E* 76: 021903.
- [75] Buboltz, J.T., Bwalya, C., Williams, K., and Schutzer, M. 2007b. High-Resolution Mapping of Phase Behavior in a Ternary Lipid Mixture: Do Lipid—Raft Phase Boundaries Depend on the Sample Preparation Procedure? *Langmuir* 23: 11968-11971.
- [76] Heberle, F.A., Buboltz, J.T., Stringer, D., and Feigenson, G.W. 2005. Fluorescence Methods to Detect Phase Boundaries in Lipid Bilayer Mixtures. *Biochim. Biohyps. Acta* 1746: 186-192.
- [77] Brown, A. C., Towles, K. B. and S. P. Wrenn. 2007a. Measuring raft size as a function of membrane composition in PC-based systems: Part 1--binary systems. *Langmuir*. 23(22): 11180-11187.
- [78] Brown, A. C., Towles, K. B. and S. P. Wrenn. 2007b. Measuring raft size as a function of membrane composition in PC-based systems: Part II--ternary systems. *Langmuir*. 23(22): 11188-11196.
- [79] Zhao, J., J. Wu, F.A. Heberle, T.T. Mills, P. Klawitter, G. Huang, G. Costanza and G.W.

- Feigenson. 2007. Phase studies of model biomembranes: complex behavior of DSPC/DOPC/Cholesterol. *Biochim. Biophys. Acta - Biomembranes* 1768: 2764–2776.
- [80] Veatch S.L., and S.L. Keller. 2005. Miscibility phase diagrams of giant vesicles containing sphingomyelin. *Phys Rev Lett.* 94: 148101.
- [81] Veatch S.L., and S.L. Keller. 2005. Seeing spots: complex phase behavior in simple mixtures. *Biochim Biophys Acta.* 1746:172–185.
- [82] Veatch, S. L., Gawrisch, K. and S. L. Keller. 2006. Closed-loop miscibility gap and quantitative tie-lines in ternary membranes containing diphytanoyl PC. *Biophysical Journal.* 90(12): 4428-4436.
- [83] Feigenson G.W, and J.T. Buboltz. 2001. Ternary Phase Diagram of Dipalmitoyl-PC/Dilauroyl-PC/Cholesterol: Nanoscopic Domain Formation Driven by Cholesterol. *Biophys. J.* 80:2775-2788.
- [84] Korlach J., Schwille P., Webb W.W. and G.W. Feigenson. 1999. Characterization of lipid bilayer phases by confocal microscopy and fluorescence correlation spectroscopy. *Proc. Natl. Acad. Sci.* 96: 8461–8466.
- [85] Ayuyan A.G., Cohen F.S. 2006. Lipid Peroxides Promote Large Rafts: Effects of Excitation of Probes in Fluorescence Microscopy and Electroformation Research During Vesicle Formation. *Biophys J.* 91: 2172-2183.
- [86] Zhao, J., Wu, J., Shao, H., Kong, F., Jain, N., Hunt, G., and Feigenson, G.W. 2007. Phase studies of model biomembranes: macroscopic coexistence of  $L\alpha + L\beta$ , with light-induced coexistence of  $L\alpha + L_o$  phases. *Biochim. Biophys. Acta* 1768: 2777-2786.
- [87] Dietrich, C. et al., 2001. Lipid rafts reconstituted in model membranes. *Biophysical Journal.* 80: 1417-1428.
- [88] Scherfeld, D., Kahya, N. and P. Schwille. 2003. Lipid dynamics and domain formation in model membranes composed of ternary mixtures of unsaturated and saturated phosphatidylcholines and cholesterol. *Biophysical Journal.* 85(6): 3758-3768.
- [89] Veatch, S. L. and S. L. Keller. 2003. Separation of liquid phases in giant vesicles of ternary mixtures of phospholipids and cholesterol. *Biophysical Journal.* 85(5): 3074-3083.
- [90] Baumgart, T., S. Hess, and W.W. Webb. 2003. Imaging coexisting fluid domains in biomembrane models coupling curvature and line tension. *Nature.* 425: 821-824.
- [91] Hammond, A. T., et al. 2005. Crosslinking a lipid raft component triggers liquid ordered-liquid disordered phase separation in model plasma membranes. *Proceedings of the National Academy of Sciences of the USA.* 102(18): 6320-6325.

- [92] Fidorra, M., et al. 2006. Absence of fluid-ordered/fluid-disordered phase coexistence in ceramide/POPC mixtures containing cholesterol. *Biophysical Journal*, 90(12): 4437-4451.
- [93] Juhasz, J., Sharom, F. J. and J. H. Davis. 2009. Quantitative characterization of coexisting phases in DOPC/DPPC/cholesterol mixtures: comparing confocal fluorescence microscopy and deuterium nuclear magnetic resonance. *Biochimica Et Biophysica Acta-Biomembranes*. 1788(12): 2541-2552.
- [94] Silvius, J.R., D. del Giudice, and M. Lafluer. 1996. Cholesterol at different bilayer concentrations can promote or antagonize lateral segregation of phospholipids of differing acyl chain length. *Biochemistry*. 35:15198-15208.
- [95] Reeves JP, and Dowben RM. 1969. Formation and properties of thin-walled phospholipid vesicles. *Journal of Cellular Physiology*. 73: 49–60.
- [96] Akashi K, Miyata H, Itoh H, and K. Kinoshita. 1996. Preparation of giant liposomes in physiological conditions and their characterization under an optical microscope. *Biophys J*. 71:3242–3250.
- [97] Morales-Pennington, N. F., et al. 2010. GUV preparation and imaging: Minimizing artifacts. *Biochimica Et Biophysica Acta-Biomembranes-Biomembranes*, 1798(7): 1324-1332.
- [98] Dimova, R., et al. 2006. A practical guide to giant vesicles. Probing the membrane nanoregime via optical microscopy. *Journal of Physics-Condensed Matter*. 18(28): S1151-S1176.
- [99] Baykal-Caglar E1, Hassan-Zadeh E, Saremi B, Huang J. 2012. Preparation of giant unilamellar vesicles from damp lipid film for better lipid compositional uniformity. *Biochim Biophys Acta*. 1818(11):2598-604
- [100] Feigenson, G. W. 2007. Phase boundaries and biological membranes. *Annual Review of Biophysics and Biomolecular Structure*, 36, 63-77.
- [101] Veatch, S. L. 2007. From small fluctuations to large-scale phase separation: lateral organization in model membranes containing cholesterol. *Seminars in Cell and Developmental Biology*. 18(5): 573-582.
- [102] Veatch, S. L., et al. 2007a. Fluorescent probes alter miscibility phase boundaries in ternary vesicles. *Journal of Physical Chemistry B*. 111(3): 502-504.
- [103] Veatch, S. L., et al. 2007b. Critical fluctuations in domain-forming lipid mixtures. *Proceedings of the National Academy of Sciences of the United States of America*. 104(45): 17650-17655.
- [104] Davis, J. H., Clair, J. J. and J. Juhasz. 2009. Phase equilibria in DOPC/DPPC-

d62/cholesterol mixtures. *Biophysical Journal*. 96(2): 521-539.

- [105] Heberle F.A., J. Wu, S.L. Goh, R.S. Petruzielo, and G.W. Feigenson. 2010 Comparison of three ternary lipid bilayer mixtures: FRET and ESR reveal nanodomains. *Biophysical Journal*. 99: 3309-3318.
- [106] Nyholm, T. K. M., et al. 2011. Construction of a DOPC/PSM/Cholesterol Phase Diagram Based on the Fluorescence Properties of trans-Parinaric Acid. *Langmuir*. 27(13): 8339-8350.
- [107] Farkas ER, and WW. Webb. 2010. Precise and millidegree stable temperature control for fluorescence imaging: application to phase transitions in lipid membranes. *The Review of Scientific Instruments*. 81: 093704.
- [108] Smith, A.K. and J.H. Freed. 2009. Determination of tie-line fields for coexisting lipid phases: an ESR study. *Journal of Physical Chemistry B*. 113: 3957-3971.
- [109] Petruzielo, R. S., et al. 2013. Phase behavior and domain size in sphingomyelin-containing lipid bilayers. *Biochimica Et Biophysica Acta-Biomembranes*. 1828(4): 1302-1313.
- [110] Vequi-Suplicy, C. C., et al. 2010. Vesicles with charged domains. *Biochimica Et Biophysica Acta-Biomembranes*, 1798(7): 1338-1347.
- [111] de Almeida, R. F. M., A. Fedorov, and M. Prieto. 2003. Sphingomyelin/ Phosphatidylcholine/ cholesterol phase diagram: boundaries and composition of lipid rafts. *Biophys. J*. 85:2406–2416.
- [112] Halling, K. K., et al. 2008. Cholesterol interactions with fluid-phase phospholipids: Effect on the lateral organization of the bilayer. *Biophysical Journal*. 95(8): 3861-3871.
- [113] Ionova, I. V., Livshits, V. A. and Marsh, D. 2012. Phase diagram of ternary cholesterol/palmitoylsphingomyelin/palmitoyloleoyl-phosphatidylcholine mixtures: spin-label EPR study of lipid-raft formation. *Biophysical Journal*, 102(8): 1856-1865.
- [114] Pokorny, A., et al. 2006. Temperature and composition dependence of the interaction of delta-lysine with ternary mixtures of sphingomyelin/cholesterol/POPC. *Biophysical Journal*. 91(6): 2184-2197.
- [115] Elson E.L., Fried E., Dolbrow J.E., and Genin G.M. 2010. Phase Separation in Biological Membranes: Integration of Theory and Experiment. *Ann. Rev. Biophys.* 39:207-226.
- [116] Konyakhina TM, Goh SL, Amazon J, Heberle FA, Wu J, and GW. Feigenson. 2011. Control of a nanoscopic-to-macroscopic transition: modulated phases in 4-Component DSPC/DOPC/POPC/chol Giant Unilamellar Vesicles. *Biophys J Letters*. 101(2):L8–L10.

- [117] Feigenson G.W. 2009. Phase Diagrams and Lipid Domains in Multicomponent Lipid Bilayer Mixtures. *Biochim. Biophys Acta.* 1788: 47-52.
- [118] Mayor S., Rao M. 2004. Rafts: scale-dependent, active lipid organization at the cell surface. *Traffic.* 5: 231-240.
- [119] Jacobson K., Mouritsen OG, and RG. Anderson. 2007. Lipid rafts: at a crossroad between cell biology and physics. *Nat. Cell. Biol.* 9: 7-14.
- [120] de Almeida, R. F., et al. 2005. Lipid rafts have different sizes depending on membrane composition: a time-resolved fluorescence resonance energy transfer study. *Journal of Molecular Biology.* 346(4): 1109-1120.
- [121] Silvius, J. R. 2003. Fluorescence energy transfer reveals microdomain formation at physiological temperatures in lipid mixtures modeling the outer leaflet of the plasma membrane. *Biophys. J.* 85:1034–1045.
- [122] Goh SL, Amazon J, and GW. Feigenson. 2013. towards a better raft model: Modulated phases in the 4-component bilayer, DSPC/DOPC/POPC/CHOL. *Biophys J.* 104:853–862.
- [123] Amazon, J. J., Goh, S. L. and GW. Feigenson. 2013. Competition between line tension and curvature stabilizes modulated phase patterns on the surface of giant unilamellar vesicles: A simulation study. *Physical Review E.* 87(2): 022708.
- [124] Seul M., and D. Andelman. 1995. Domain shapes and patterns: the phenomenology of modulated phases. *Science.* 267:476–483.

## CHAPTER 2

### **Control of a Nanoscopic-to-Macroscopic Transition: Modulated Phases in 4-Component DSPC/DOPC/POPC/Chol Giant Unilamellar Vesicles<sup>1</sup>**

#### **2.1 Abstract**

We have found modulated phase morphology in a particular region of composition within the liquid-ordered + liquid-disordered coexistence region in the four-component lipid bilayer mixture DSPC/DOPC/POPC/Chol. By controlling lipid composition, we could see distinct types of modulated liquid-liquid phase morphologies, including linear, irregular, and angular features in giant unilamellar vesicles. We used a combination of confocal, two-photon, wide-field fluorescence, and differential interference contrast microscopies, and used stringent controls to minimize light-induced artifacts. These studies establish that both the size and morphology of membrane rafts can be controlled by the concentration and the type of low-melting lipid in mixtures with cholesterol and a high-melting lipid.

#### **2.2 Materials and methods**

Phospholipids were purchased from Avanti Polar Lipids (Alabaster, AL), and cholesterol was from Nu Chek Prep (Elysian, MN). Fluorescent dyes C12:0-DiI (1,1'-didodecyl-3,3,3',3'-

---

<sup>1</sup> The following section is reproduced from: Konyakhina TM, Goh SL, Amazon J, Heberle FA, Wu J, Feigenson GW. Control of a nanoscopic-to-macroscopic transition: modulated phases in 4-Component DSPC/DOPC/POPC/chol Giant Unilamellar Vesicles. *Biophys J Letters*. 2011;101(2):L8–L10. TMK and SLG contributed equally to GUV preparation and data analysis. JA developed the mathematical model.

tetramethylindocarbocyanine perchlorate) and BoDIPY-PC (2-(4,4-difluoro-5,7-dimethyl-4-bora-3a,4a-diaza-s-indacene-3-pentanoyl)-1-hexadecanoyl-sn-glycero-3-phosphocholine) were from Invitrogen (Carlsbad, CA). Concentrations of phospholipid stocks were determined to <1% error with inorganic phosphate assay, and purity checked with thin layer chromatography in 65:25:4= chloroform/methanol/water solvent (1). Cholesterol at defined concentration was prepared by standard gravimetric procedures. Fluorescent dye concentrations were determined using absorption spectroscopy on an HP 8452A spectrophotometer (Hewlett-Packard, Palo Alto, CA).

### **2.2.1 Sample preparation and microscopy**

Giant unilamellar vesicles (GUVs) were prepared using a modified electroformation procedure as described in (2). GUVs were swelled at 55°C in 100 mM sucrose, and cooled to room temperature (23°C) over 10 hours. For 2-photon, confocal, and most wide-field fluorescence microscopy experiments, GUVs were diluted into 100 mM glucose before imaging. The difference in solution density allows vesicles to settle more efficiently and also creates a sufficient refractive index difference to enable locating and focusing on GUVs without intense illumination (1,3). For DIC microscopy, the internal and external media were kept identical (100 mM sucrose) to avoid mismatch in buffer refractive indices that might distort DIC imaging.

Wide-field microscopy was performed on the Nikon Diaphot-TMD and Nikon Ti-E Perfect Focus (Micro Video Instruments Inc., Avon, MA and Rochester, NY) inverted microscopes at 23°C using 60X 1.4NA oil immersion objectives. GUVs were labeled with C12:0-DiI at 0.02 mol%; the dye partitions preferentially into the Ld-phase. Controls for light-induced artifacts included samples with 0.014 and 0.01 mol % C12:0-DiI. To minimize light-induced artifacts, we used a combination of methods including lowering exposure time (down to 10-20 ms), using

neutral density filters, and in particular, locating GUVs with transmitted light or DIC prior to exposure to the intense illumination needed for fluorescence imaging. Images were taken with a Photometrics charge-coupled device camera CoolSNAP<sub>HQ2</sub> (Tucson, Arizona) on the Diaphot-TMD, and with a DR328G Andor Clara Interline Camera (MVI Inc., Avon, MA and Rochester, NY) on the Ti-E. C12:0-DiI was imaged with 535-550 nm excitation and 565-610 nm emission on the Diaphot-TMD; 528-553 nm excitation and 590-650 nm emission on the Ti-E. Images were contrast-enhanced and analyzed with NIS Elements Basic Research Software (MVI, Inc.). Confocal imaging was performed on an inverted Zeiss 710 confocal microscope at 23°C using a 63X 1.4NA oil immersion objective. Confocal laser excitation was 561 nm (10.0 % ) with pinhole 98  $\mu$ m, and images collected at 564 – 684 nm. Confocal images were analyzed with Zeiss ZEN software. Two-photon microscopy was performed on home-built apparatus based on an inverted Zeiss Axiovert 35 microscope at 23°C using a 60X 1.2NA water immersion objective. Images were collected using a Hamamatsu HC125-02 Bialkali photomultiplier tube (Hamamatsu Corp., Middlesex, NJ). GUVs were labeled with 0.02 mol% BoDIPY-PC, which partitions preferentially into the Ld-phase. The excitation wavelength was 960 nm. Images were contrast-enhanced, and Z-projection image stacks prepared in Image J.

## 2.3 Results

The size and shape of coexisting Lo+Ld domains in lipid mixtures might affect behaviors of cell membranes (1). We have reported that GUVs of DSPC/DOPC/chol exhibit macroscopic liquid/liquid Lo+Ld domains (2,3), whereas GUVs of DSPC/POPC/chol appear uniform, even though FRET indicates liquid/liquid phase separation (3). We are interested in the transition from nano- to macro-scale morphologies. When liquid phases coexist, line tension drives the phase

domains toward minimum perimeter-- a single round domain within a matrix of the other phase. This simple morphology can be modulated when a long-range repulsive interaction competes with the free energy cost of forming excess domain interface (4). This occurs for small domains in monolayers that do not coalesce due to long-range dipole-dipole repulsion (5). In other cases, the repulsive interaction arises from contractile tension from adsorption on a substrate (6,7). Interdomain repulsion can also be generated from curvature effects in phase-separated bilayers, whereby fluid superstructures are maintained (8). Patterned phases can also arise from dynamic behavior, such as critical fluctuations (9-11) or trapped domain growth (12). In all cases, competing interactions are needed for structured morphologies. Here we report the existence of modulated morphology at certain compositions within the Lo+Ld coexistence region in the 4-component DSPC/DOPC/POPC/chol mixture. A key aspect of this study is simplicity: (i) only lipid-lipid interactions are involved to yield both the line tension and any competing repulsive interaction; and (ii) composition, the only variable, is under stringent experimental control. This control might be useful in order to relate model membrane studies to the existence of nano-scale rafts in cells (1). We used fluorescence and DIC microscopies to image domain morphologies of GUVs prepared with fixed mole fractions ( $\chi$ ) of both cholesterol and DSPC, while varying [DOPC] and [POPC] (see Supporting Materials for details). We define a replacement ratio  $\rho$  as follows:

$$\rho \equiv [\text{DOPC}]/([\text{DOPC}+\text{POPC}]) (\%)$$

Fixing  $\chi_{\text{chol}} = 0.25$  and  $\chi_{\text{DSPC}} = 0.45$ , modulated phases are observed in a narrow window of composition with  $\rho = 15\text{-}25\%$  (Fig. 2.1). At  $\rho < 15\%$ , GUVs look uniform, whereas at  $\rho > 25\%$ , they display macroscopic round Lo + Ld domains. We also varied  $\rho$  at  $\chi_{\text{chol}} = 0.22$  and  $\chi_{\text{DSPC}} = 0.39$ , and found similar morphological transitions. We catalog five types of

morphologies (Figs. 2.1B and 2.2B-E; see Table 2.1 for statistics), including honeycomb arrangements of Lo domains, irregular 2D bubbles, and stripes.

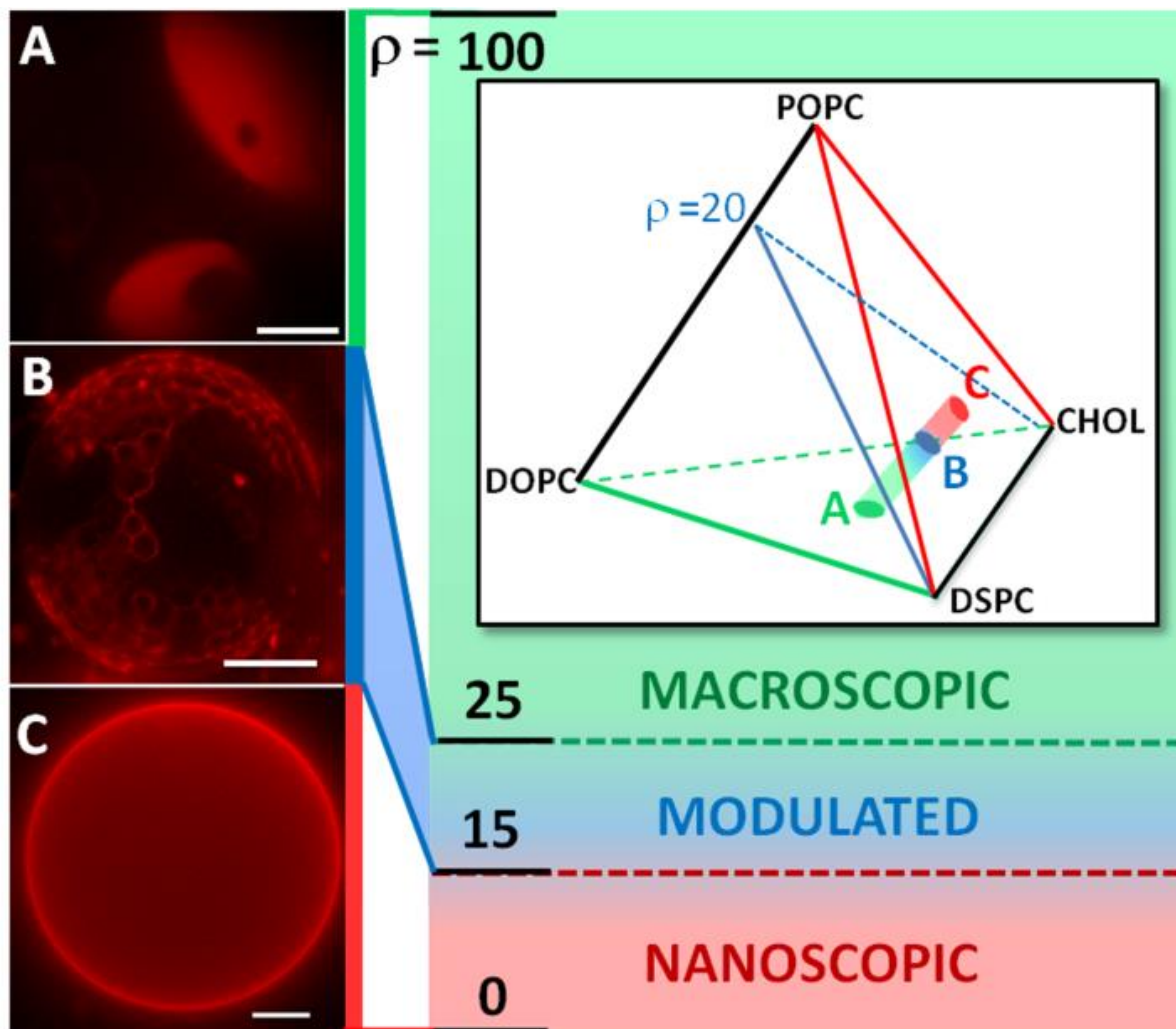


**Figure 2.1** Modulated phases occur at  $\rho = 15 - 25\%$  as POPC is replaced by DOPC along Lo+Ld compositional trajectory (inset). GUV compositions DSPC/DOPC/POPC/chol at  $23^\circ\text{C}$ : (A) 0.45/0.3/0/0.25 ( $\rho = 100\%$ ); (B) 0.45/0.06/0.24/0.25 ( $\rho = 20\%$ ); (C) 0.45/0/0.3/0.25 ( $\rho = 0\%$ ). Dye C12:0-DiI (0.02 mol%, color-merged red) partitions into Ld. Scale bars 10  $\mu\text{m}$ .

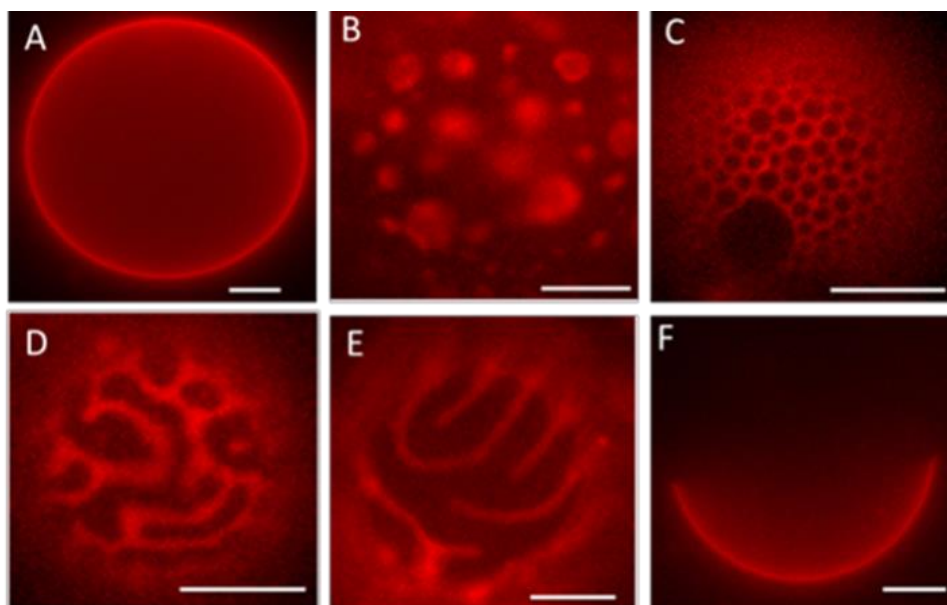


**Figure 2.2** GUV patterns as POPC is replaced by DOPC. (A) uniform; (B) continuous Lo with asymmetric Ld domains; (C) honeycomb; (D) irregular patches of Lo; (E) regular striped pattern; (F) round macro Lo+Ld domains. Compositions of DSPC/DOPC/POPC/chol: (A) 0.45/0.03/0.27/0.25; (B,E) 0.45/0.05/0.25/0.25; (C) 0.39/0.06/0.33/0.22; (D) 0.39/0.10/0.29/0.22; (F) 0.45/0.30/0/0.25. C12:0-DiI at 0.02 mol%. Scale bars 10  $\mu$ m, temperature 23°C.

**Table 2.1** Percentage of GUVs having the observed morphologies

$\rho$	N GUV	% macroscopic	% modulated	% uniform
10	60	2	31	67
15	82	15	63	22
20	89	22	70	8
25	88	23	74	3
30	66	80	20	0

**Table 2.1** shows the count distribution of three main GUV morphologies (macroscopic round domains; modulated domains; uniform) observed from  $\rho = 10$ -30, at  $\chi_{\text{DSPC}} = 0.45$  and  $\chi_{\text{chol}} = 0.25$ .

These morphologies are intriguing: though compositions are within the liquid-liquid coexistence region, domains were not round, displaying linear features that come together at angles. We also observed that individual GUVs at fixed composition could show different domain

morphologies (Figs. 2.2 *B,E*, 2.4*C* and 2.8*B*). These intermediate states of the nano-to-macro domain size transition might have distinct physical and chemical properties that would set them apart from fully formed macroscopic or nanoscopic domains.

Artifactual light-induced domains can occur under commonly-used experimental conditions (13). Here we have made substantial efforts to minimize light-induced artifacts. We used C12:0-DiI probe concentrations as dilute as 0.010 mol %, neutral density filters up to OD = 1.0, and shutter open time during imaging as short as 10 ms. Most important, we found modulated phase morphologies without intense illumination, obtaining images with DIC to locate GUVs prior to fluorescence imaging.

Indeed, DIC experiments were decisive in proving that (a) modulated phases exist prior to intense light exposure and (b) modulated phases exist and can be observed even in samples without a probe (Fig. 2.6). GUVs with modulated phases have discernible DIC patterns (Fig. 2.7) that correlate exactly with fluorescence images of the same GUV (Figs. 2.3 and 2.8). Furthermore, the patterns are not dependent on details of the wavelength, intensity or duration of the delivery of light energy to the samples, because 2-photon, confocal, and widefield microscopies all showed modulated phases within the same composition range,  $\rho = 15\text{-}25\%$  (Fig. 2.4). We also observed patterned domains with both DIC and fluorescence on a free-floating GUV (data not shown), confirming that the modulated domains in our system are not caused by adhesion to glass.

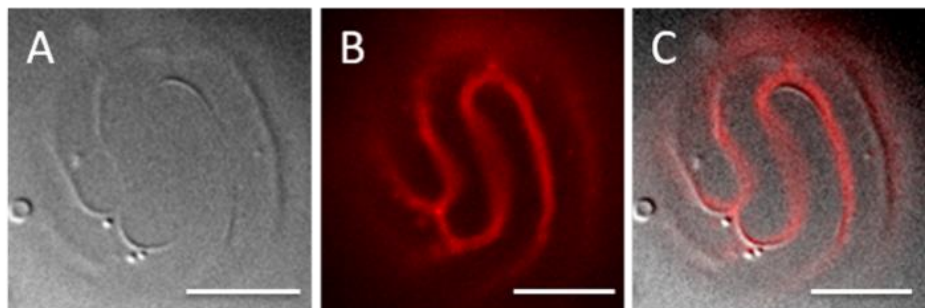


**Figure 2.3** DIC shows the same pattern as does fluorescence. DSPC/DOPC/POPC/chol = 0.45/0.05/0.25/0.25 at 23°C. (A) DIC; (B) fluorescence; (C) superimposition of DIC and fluorescence. See Fig. S3 for additional images. Scale bars 10  $\mu\text{m}$

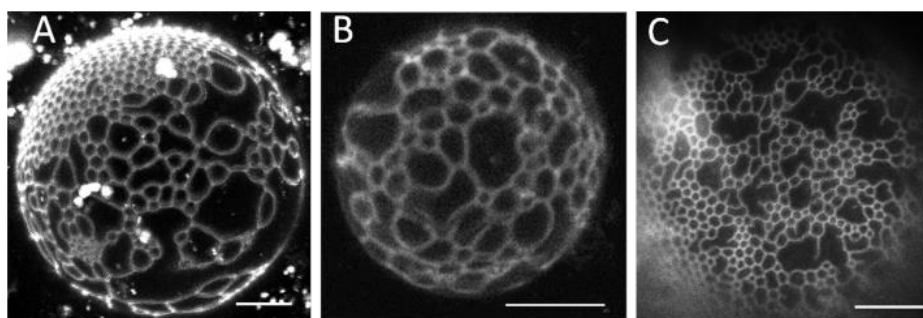


**Figure 2.4** Different fluorescence microscopies show similar patterns at 23°C. (A) confocal image, C12:0-DiI at 0.02 mol%; (B) 2-photon image Bodipy-PC at 0.02 mol%; (C) wide-field image, C12:0-DiI at 0.02 mol%. DSPC/DOPC/POPC/chol = 0.45/0.05/0.25/0.25. Scale bars 10  $\mu\text{m}$ .

Theoretical modeling shows that a competition between the interdomain line energy that tends to reduce domain perimeter and a repulsive domain-domain interaction (perhaps domain curvature, dipole moment or some other property of Lo domains) yields stable, modulated phase patterns. Calculations by Liu et al. (14) suggest that such competing interactions can control formation of nano-sized rafts in cells. To model the observed phase patterns we used a field theory approach with competing interactions (see Supporting Materials for details). We considered line tension, which favors large round domains, and a repulsive field, which tends to disperse domains. We are currently studying the nature of the repulsive field that competes with line tension, so its

form is not yet known. In order to perform preliminary calculations, here we model it as dipole-dipole repulsion. We model the free energy phenomenologically as a Landau-Ginzburg energy functional (4) with a long range field term as follows:

$$F = \iint \left[ -B\phi^2(r) + \frac{B}{2}\phi^4(r) + \frac{K}{2}|\nabla\phi(r)|^2 \right. \\ \left. + Q\mu(r)D[\mu](r) \right] dA \quad (1)$$

where  $\phi$  is the order parameter at position  $r$ ,  $B$  sets the free energy scale of the phase separation,  $K$  is proportional to line tension,  $Q$  is the coupling coefficient for the field term,  $\mu$  is the area density of dipoles, and  $D[\mu]$  is the electric field normal to the membrane. This choice of dipole-dipole interactions is an initial approach; other forms of the repulsive term, perhaps involving curvature, might prove to better model the interactions. See Supporting Materials for more detailed discussion.

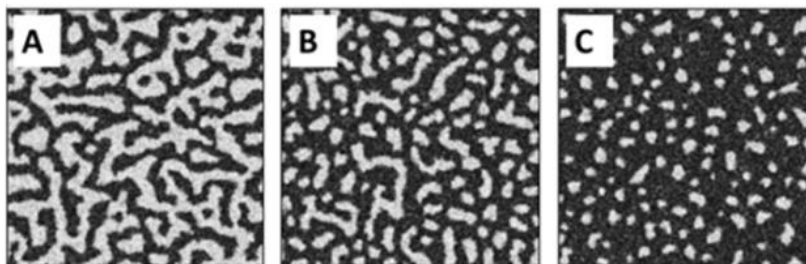


**Figure 2.5** Phase patterns change with Lo area fraction  $P$ , with  $B = 100$ ,  $K = 10$ ,  $Q = 2$ ,  $\mu=1$  in Ld (dark) and 0 in Lo (bright). (A)  $P = 0.5$ , (B)  $P = 0.6$ , (C)  $P = 0.7$ .

We used Monte Carlo simulations to find equilibrium configurations that minimize Eq. 1. Fig. 2.5 shows resulting patterns that could be obtained along a thermodynamic tieline, varying only the phase fractions. The fraction of each phase varies along a tieline, whereas phase properties (line tension, dipole density) are fixed, enabling a simple connection between model and

experiments. For example, Fig. 5 shows a continuous transition from stripe to small isolated domains as  $P$  deviates from 0.50, where  $P$  is the area fraction of  $L_o$ . The parameters  $B$ ,  $K$ , and  $Q$  were chosen to be in a region of non-trivial phase morphology.

Obtaining true linewidths of modulated phase patterns could aid theoretical investigations into the nature of the competing interactions. Measured linewidths for the honeycomb and 2D bubble patterns are in the range 0.4 - 0.7  $\mu\text{m}$ . Given small movements of the GUVs, these measurements are consistent with true linewidths being diffraction limited. Further experiments together with modeling might clarify the relationship between lipid concentrations and types of patterns and linewidths of modulated phases in these 4-component mixtures. We benefit greatly from studying a system with known thermodynamic tielines (2, 3).

In cells, both equilibrium and nonequilibrium processes can contribute to the formation and stability of domains (9). Here we show that *lipid composition alone* can control the patterns of phase-separated membrane domains. However, we have not yet indentified the long-range interaction that competes with line tension to control domain morphology (Figs. 2.9 and 2.10). Understanding the nature of this interaction might be important for understanding the nature of bilayer phase domain size and shape in cells.

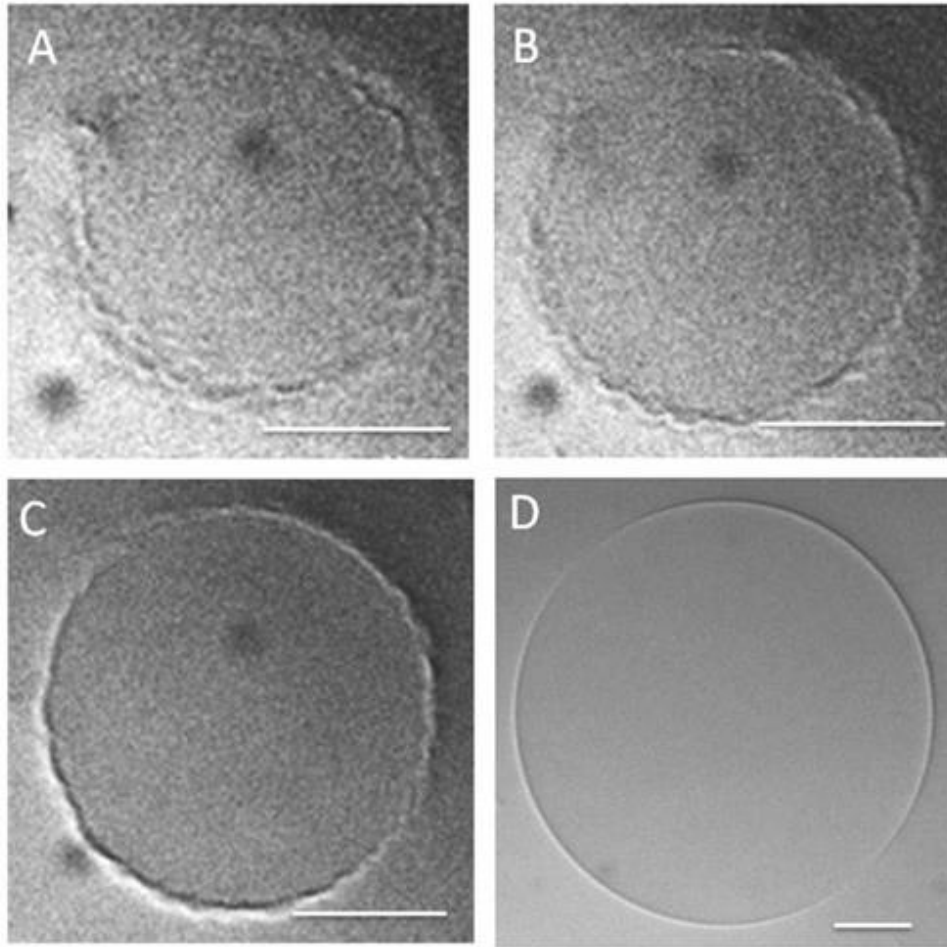


**Figure 2.6** DIC images of a GUV without probe C12:0-DiI show scalloped edges at  $\rho = 20\%$  (A-C) compared to a probe-free, uniform GUV (D). (A-C) shows the same GUV at different planes of a z-stack. Compositions DSPC/DOPC/POPC/chol: (A-C) 0.45/0.06/0.24/0.25; (D) 0.45/0.03/0.27/0.25. Scale bars 10  $\mu\text{m}$ , temperature 23°C.

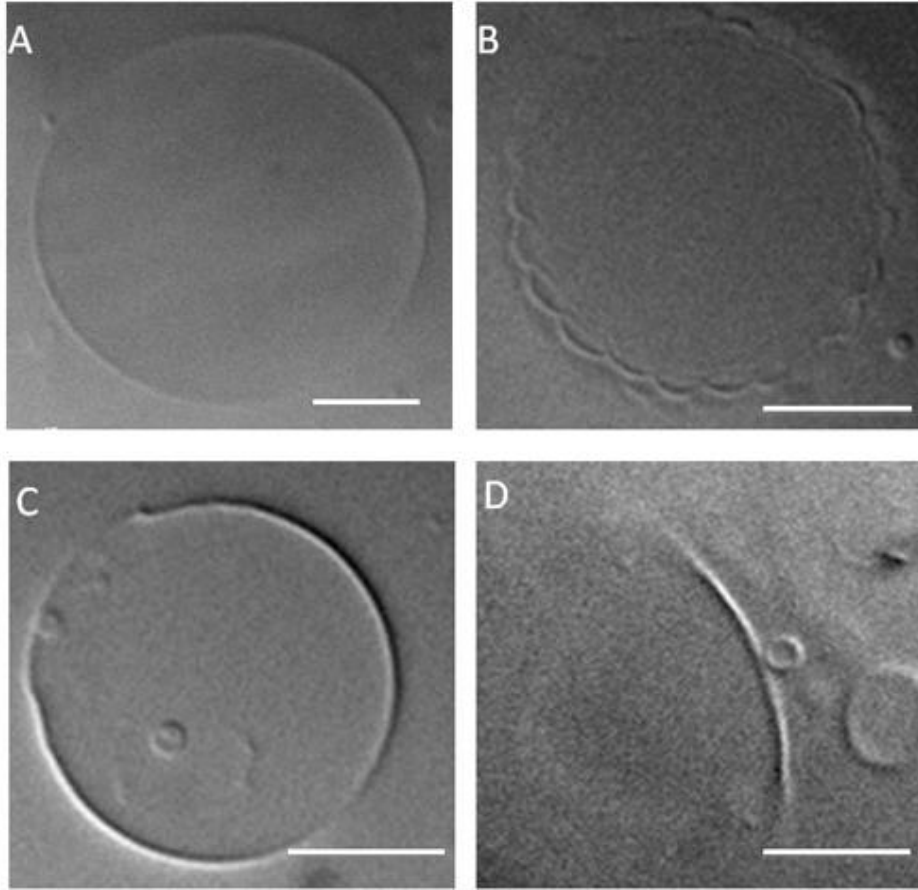


**Figure 2.7** GUV morphologies imaged with DIC. (A) uniform, featureless with smooth edges; (B) scalloped edges pattern; (C) budding vesicle; (D) border of Lo + Ld macroscopic phases. Compositions of DSPC/DOPC/POPC/chol: (A) 0.45/0.015/0.285/0.25; (B) 0.45/0.045/0.255/0.25; (C) 0.45/0.09/0.21/0.25; (D) 0.45/0.30/0/0.25. Scale bars 10  $\mu\text{m}$ , temperature 23°C.

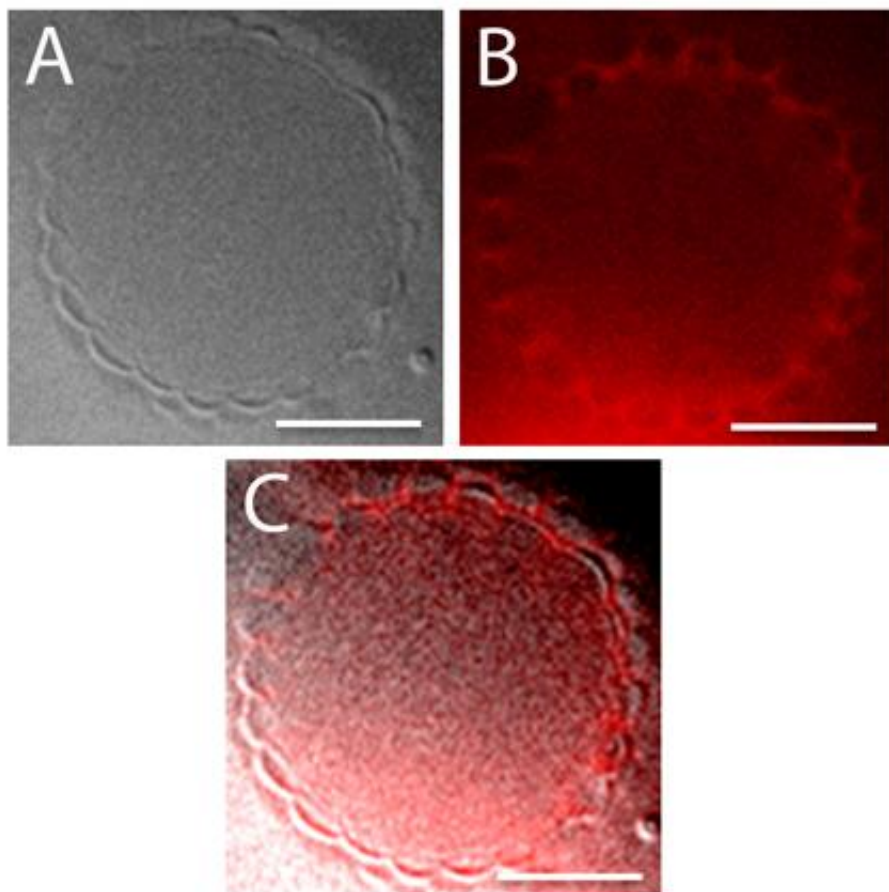


**Figure 2.8** Complementarity of fluorescence and DIC images for a GUV with honeycomb pattern at DSPC/DOPC/POPC/chol = 0.45/0.045/0.255/0.25. (A) DIC; (B) fluorescence image, C12:0-DiI at 0.02 mol%; (C) superimposition of DIC and fluorescence images. Scale bars 10  $\mu\text{m}$ , temperature 23°C.

## References

- [1] Lingwood, D. and K. Simons. 2010. Lipid Rafts as a Membrane-Organizing Principle. *Science*. 327:46-50.
- [2] Zhao, J., J. Wu, F. A. Heberle, T. T. Mills, P. Klawitter, G. Huang, G. Costanza, and G. W. Feigenson. 2007. Phase studies of model biomembranes: Complex behavior of DSPC/DOPC/Cholesterol. *Biochim. Biophys. Acta*. 1768:2764-2776.
- [3] Heberle, F. A., J. Wu, S. L. Goh, R. S. Petruzielo, and G. W. Feigenson. 2010. Comparison of Three Ternary Lipid Bilayer Mixtures: FRET and ESR Reveal Nanodomains. *Biophys. J.* 99:3309-3318.
- [4] Seul, M. and D. Andelman. 1995. Domain Shapes and Patterns: The Phenomenology of Modulated Phases. *Science*. 267:476-483.
- [5] McConnell, H. M. 1991. Structures and Transitions in Lipid Mono layers at the Air-Water Interface. *Ann. Rev. Phys. Chem.* 42:171-195.
- [6] Rozovsky, S., Y. Kaizuka, and J. T. Groves. 2004. Formation and Spatio-Temporal Evolution of Periodic Structures in Lipid Bilayers. *J. Am. Chem. Soc.* 127:36-37.
- [7] Plass, R., N. C. Bartelt, and G. L. Kellogg. 2002. Dynamic observations of nanoscale self-assembly on solid surfaces. *J. Phys. Condens. Matter*. 14:4227.
- [8] Kaizuka, Y. and J. T. Groves. 2010. Bending-mediated superstructural organizations in phase-separated lipid membranes. *New J. Phys.* 12: 095001
- [9] Fan, J., M. Sammalkorpi, and M. Haataja. 2010. Formation and regulation of lipid microdomains in cell membranes: Theory, modeling, and speculation. *FEBS Lett.* 584:1678-1684.
- [10] Honerkamp-Smith, A. R., S. L. Veatch, and S. L. Keller. 2009. An introduction to critical points for biophysicists; observations of compositional heterogeneity in lipid membranes. *Biochim. Biophys. Acta*. 1788:53-63.
- [11] Baumgart, T., S. T. Hess, and W. W. Webb. 2003. Imaging coexisting fluid domains in biomembrane models coupling curvature and line tension. *Nature*. 425:821-824.
- [12] Semrau, S., T. Idema, T. Schmidt, and C. Storm. 2009. Membrane-Mediated Interactions Measured Using Membrane Domains. *Biophys. J.* 96:4906-4915.
- [13] Zhao, J., Wu, J., Shao, H., Kong, F., Jain, N., Hunt, G., and G.W. Feigenson. 2007. Phase

studies of model biomembranes: macroscopic coexistence of  $L\alpha + L\beta$ , with light-induced coexistence of  $L\alpha + L_o$  phases. *Biochim. Biophys. Acta* 1768: 2777-2786.

- [14] Liu, J., S. Qi, J. T. Groves, and A. K. Chakraborty. 2005. Phase Segregation on Different Length Scales in a Model Cell Membrane System. *J. Phys. Chem. B.* 109:19960-19969.

## Supplemental Materials

### 2.S.1 Theory

The Landau-Ginzburg energy functional is a widely applicable phenomenological description of phase separation in field theory models (4). For our approach we modeled the local phase as a scalar field (order parameter) on the 2D plane with toroidal boundary conditions. The order parameter varies continuously on  $[-1,1]$ , where  $(-1)$  represents Ld and  $(+1)$  represents Lo:

$$F = \iint [-B\phi^2(r) + \frac{B}{2}\phi^4(r) + \frac{K}{2}|\nabla\phi(r)|^2 + Q\mu(r)D[\mu](r)] dA \quad (S1)$$

where  $\phi$  is the order parameter at position  $r$ ,  $B$  defines the free energy scale of the phase separation,  $\mu$  is the local area density of molecular dipoles,  $D[\mu](r)$  is the electric field normal to the membrane,  $K$  is proportional to line tension, and  $Q$  is the coupling coefficient for the field. Normally the quadratic and quartic couplings are independent; here they are fixed to ensure that the energy minima always occur at  $(\pm)1$ . The amount of each phase is fixed by constraining the order parameter to be conserved. We specify the amount of each phase by  $P$ , defined as the area fraction of Lo:

$$P = \frac{1}{2A_{\text{Tot}}} \left[ \iint \phi(r) dA \right] + \frac{1}{2} \quad (S2)$$

where  $A_{\text{Tot}}$  is the total simulation area. The long range field term is computed as a convolution of the dipole density with the point source field (which goes as  $1/r^3$ ).

$$\mu(r) = \left( \frac{\mu_o - \mu_d}{2} \right) \phi(r) + \left( \frac{\mu_o + \mu_d}{2} \right) \quad (S3)$$

$$D[\mu](r) = \int \frac{\mu(r')}{|r - r'|^3} dA' \quad (S4)$$

where  $\mu_o$  and  $\mu_d$  are the field source densities in the Lo and Ld phases, respectively. The order parameter is discretized and shuffled about the plane using a Monte Carlo/Metropolis algorithm to arrive at a minimal energy configuration. Competition between line tension (K) and the repulsive field term (Q) drives the system to reach equilibrium patterns approximating the experimental observations. The field we studied here is modeled after electrostatic dipole-dipole interactions. Using electrostatics as the dispersive term does not take into account the effects of salt screening or the large dielectric mismatch from the interior/exterior of the membrane. To check the physicality of long range dipole interactions in bilayer membranes we solved for the electrostatic potential in and around a bilayer submerged in an ionic solution using the Poisson-Boltzmann equation (5):

$$\nabla \cdot [\epsilon(r)\nabla V(r)] = \epsilon(r)\kappa^2(r)V(r) - \rho(r) \quad (S5)$$

where  $\kappa(r)$  is the inverse Debye length,  $\epsilon(r)$  is the local dielectric,  $V(r)$  is the electrostatic potential, and  $\rho(r)$  is the charge density. Equation S5 was solved using an iterative relaxation method for a cylindrically symmetric charge distribution of two thin discs located at the headgroup/water interface and the headgroup/acyl chain interface to mimic an array of dipoles normal to the membrane. The dielectric is varied smoothly from the low dielectric in the chain region to the high dielectric of the water.  $\kappa$  varied discontinuously from zero inside the bilayer to a finite value in solution. The magnitude of the charge separation was tuned to match the experimental transmembrane potential (300 mV). This gave a value of  $\sim 0.6$  Debye per lipid normal to the bilayer (Fig. 2.9). For a 16 nm diameter domain, we found that for various monovalent salt concentrations the transverse potential in the headgroup region falls off exponentially upon moving radially outward from the edge of the domain. Even for the case of no salt (which matches the experimental

conditions) we found an exponential decay length of no more than 4 nm (Fig. 2.10). This analysis shows that the use of a long range dipole-dipole term in the energy functional might be justified only for very small nanodomains. We are currently studying other possible long range competing interactions to explain the modulated phase shapes and sizes, such as domain curvature interacting with bilayer fluctuations, or an intrinsic property of the Lo phase that is favorable for smaller domains.

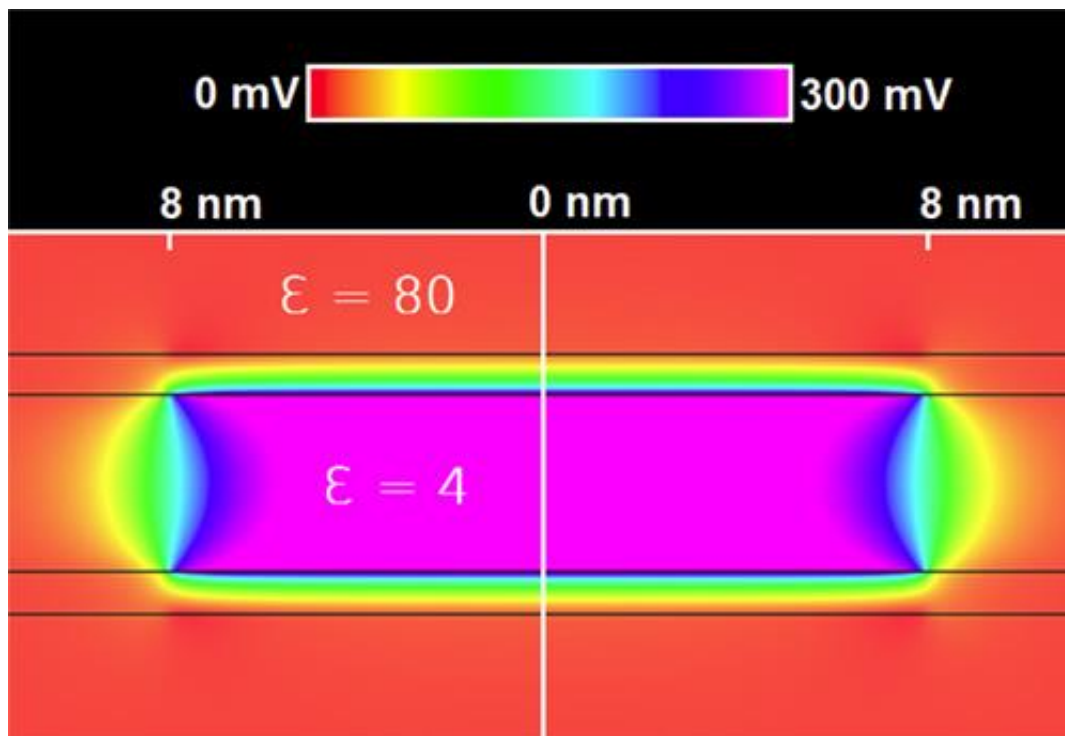


**Figure 2.9** Cross section of the bilayer showing the electrostatic potential obtained by solving Eq. S5 everywhere inside a 16 nm circular domain with a Debye length of 1 nm in solution.

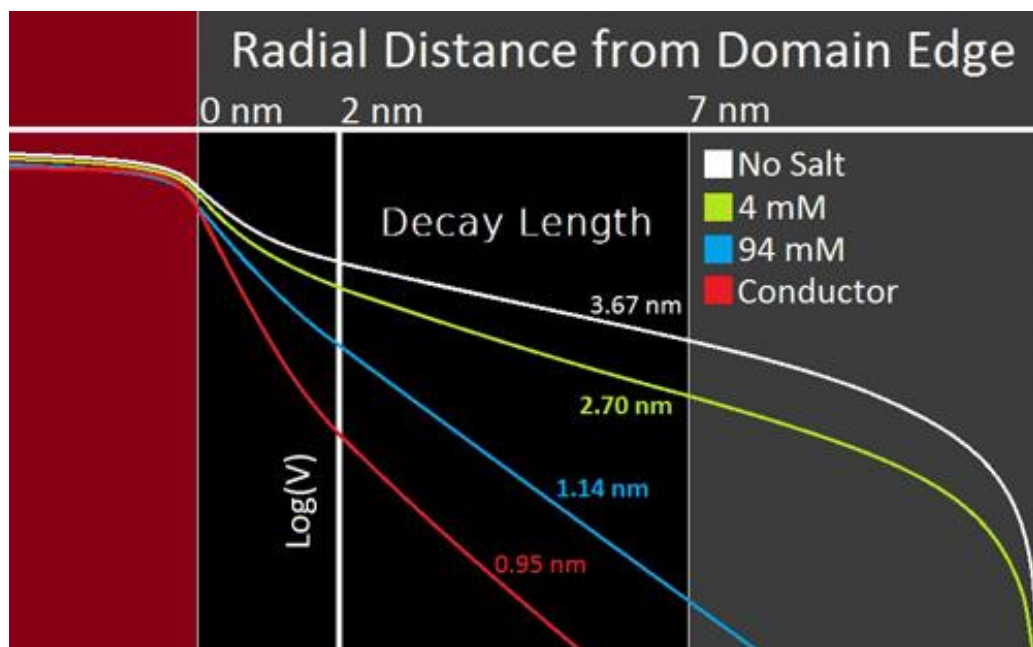


**Figure 2.10** Log plot of the potential in the headgroup region moving radially outward from the edge of the domain (red) for various salt concentrations. Decay lengths are shown next to each curve.

## REFERENCES

- [1] Morales-Pennington N.F, J. Wu, E.R. Farkas, S.L. Goh, T.M. Konyakhina, J.Y. Zheng, W.W. Webb, and G.W. Feigenson. 2010. GUV Preparation and Imaging: Minimizing Artifacts. *Biochim. Biophys. Acta.* 1798:1324-1332.
- [2] M.I. Angelova, S. Soléau, P. Méléard, J.F. Faucon and P. Bothorel. 1992. Preparation of giant vesicles by external AC fields. Kinetics and application. *Prog. Colloid Polym. Sci.* 89:127-131
- [3] Akashi, K., H. Miyata, H. Itoh, and K. Kinoshita, Jr. 1996. Preparation of giant liposomes in physiological conditions and their characterization under an optical microscope. *Biophys. J* 71:3242-3250.
- [4] Seul, M. and D. Andelman. 1995. Domain Shapes and Patterns: The Phenomenology of Modulated Phases. *Science.* 267:476-483.
- [5] Travasset, A. 2006. Effect of dipolar moments in domain sizes of lipid bilayers and monolayers. *J. Chem Phys.* 125: 084905.

## CHAPTER 3

### Phase Diagram of a 4-Component Lipid Mixture: DSPC/DOPC/POPC/Chol<sup>2</sup>

#### 3.1 Abstract

We report the first 4-component phase diagram for the lipid bilayer mixture, DSPC/DOPC/POPC/chol (distearoylphosphatidylcholine/dioleoylphosphatidylcholine/1-palmitoyl, 2-oleoylphosphatidylcholine/cholesterol). This phase diagram, which has macroscopic Ld + Lo phase domains, clearly shows that all phase boundaries determined for the 3-component mixture containing DOPC transition smoothly into the boundaries for the 3-component mixture containing POPC, which has nanoscopic phase domains of Ld + Lo. Our studies start from two published ternary phase diagrams, and show how these can be combined into a quaternary phase diagram by study of a few hundred samples of intermediate compositions.

#### 3.2 Introduction

Phase diagrams of chemically well-defined lipid mixtures help to clarify the behavior of biological membranes. In particular, mixtures of a high-melting phosphatidylcholine or sphingomyelin, a low-melting PC, and cholesterol have proven to be especially useful. These 3-

---

<sup>2</sup> The following section is reproduced from: Konyakhina TM, Wu J, Mastroianni JD, Heberle FA, Feigenson GW. 2013. Phase diagram of a 4-component lipid mixture: DSPC/DOPC/POPC/chol. *Biochim Biophys Acta*. 1828(9):2204-14. Konyakhina performed FRET and GUV experiments, analyzed data and wrote the paper. F. Heberle performed theoretical modeling and mathematical derivation of the 3-dye method. J. Wu collected some FRET data and J. Mastroianni used software to create a final 3D phase diagram.

component mixtures show coexisting bilayer phases over much of the composition space. A standard format for showing the phase behavior of all possible combinations of a 3-component mixture is the triangular phase diagram, or “Gibbs Triangle”. The particular phase behavior where liquid-disordered (Ld) and liquid-ordered (Lo) phases coexist has been termed “the raft region”, and might provide a useful model for understanding behaviors of the outer leaflet of animal cell plasma membranes. Lipid compositional phase diagrams describe the occurrence and location in composition space of phase types (e.g., solid gel L $\beta$ , liquid-ordered Lo, and liquid-disordered Ld) and their coexistence regions at equilibrium. For 3-component lipid mixtures, many fluorescence imaging-based studies have focused on either DOPC or else diphytanoyl-PC as the low-melting lipid, because the region of coexisting Ld + Lo phases shows easily identifiable macroscopic phase domains in giant unilamellar vesicles (GUVs), whether the high-melting lipid is a SM, DPPC, or DSPC [1-3]. In contrast, Ld + Lo phase domains are not visible with standard light microscopy when (i) the low-melting lipid component has one saturated acyl chain and one monounsaturated chain, e.g., POPC [3, 4] or SOPC [5]; or (ii) the low-melting lipid is DLPC [6, M. Doktorova unpublished results]. In this case, domains can be detected by some spectroscopic methods, for example, by fluorescent or spin-label probes that partition between the domains [7, 8], or by neutron scattering without probes [9]. In brief, methods sensitive to submicron length scales consistently imply liquid phase heterogeneity in POPC- and SOPC-containing ternary mixtures [7, 10-12]. The size scale of phase domains found with POPC or SOPC is therefore below the optical diffraction limit, or “nanoscopic”. Such small phase domains might be a good model for the outer leaflet of animal cell plasma membrane, which also seems to have nanoscopic coexisting Ld + Lo phase domains [13-15]: Liquid-liquid phase separation has been detected *in vivo* in cell membranes

using techniques including FRET [16], FRAP [17], ESR [18], and super resolution optical methods [19-21].

In cells, the range of size scales of any phase domains, as well as domain shape and connectivity, are not known. Furthermore, it is quite possible that membranes of living cells use spatial organization on multiple length scales, rather than one special size. We would benefit from chemically simple model systems that also have phase coexistence that spans the range from nanoscopic to macroscopic, thus enabling study of a range of domain sizes [22]. Here we explore the complexity of such a lipid mixture. We find that four components are the minimum to exhibit the range of size scales of coexisting phase domains from nanometers to microns as a function of mixture lipid composition. Unexpectedly, we discovered that the transition from small to large Ld + Lo domains is not at all linear, but instead passes through a compositional range in which phases show a variety of shapes and sizes [23, 24]. The compositional location of this range might be significant, and by solving the entire quaternary mixture phase behavior, we are able to place this region of “modulated phases” in composition space.

A challenge for constructing a phase diagram is to determine phase boundaries with sufficient precision to establish (i) every phase region; (ii) whether any stoichiometric compositions appear; (iii) whether any phase boundaries intersect the binary axes; and (iv) comparisons of phase diagrams when, for example, lipid chain lengths differ. Such precision requires examination of a large number of samples. For example, with 20 samples binary mixtures can yield  $\sim \pm 5$  mole% compositional resolution. This much uncertainty would be acceptable for certain studies, but not in cases where the uncertainty is comparable to the compositional range of interest. Ternary mixtures would require approximately 400 samples of different compositions to achieve  $\pm 5$  mole% resolution, and quaternary mixtures would require nearly 8000 samples to

evenly cover the entire composition space. A second problem is that the location of phase boundaries is not always well marked by changes in fluorescence or other phase-sensitive measurements. In order to solve this problem, we introduce here a new method to locate phase boundaries with higher accuracy. Our studies, at 2 mole% compositional resolution for most boundaries, start from two published ternary phase diagrams [4, 7], and show how these can be combined into a quaternary phase diagram by study of just a few hundred samples of intermediate compositions.

We note that a different view of the DSPC/POPC/chol mixture is that no Ld + Lo “nanodomain phase separation” occurs, and instead, fluctuations in the vicinity of a critical point give rise to transient changes of bilayer physical properties [25-27]. As we make clear below, the findings described here of continuous phase boundaries between DSPC/DOPC/chol and DSPC/POPC/chol over the entire composition space, support the view that Ld + Lo phase coexistence occurs whether phase domains are small or large, with all regions throughout the tetrahedron in accord with the Gibbs Phase Rule.

### **3.3 Materials and Methods**

#### **3.3.1 Materials**

Phospholipids were purchased from Avanti Polar Lipids (Alabaster, AL), and cholesterol from Nu Chek Prep (Elysian, MN). Fluorescent dyes C20:0-DiI, C12:0-DiI, and BoDIPY-PC were from Invitrogen (Carlsbad, CA), DHE was from Sigma-Aldrich (St. Louis, MO), and TOE (tryptophan oleoyl ester) was a gift from Erwin London. Phospholipid stocks were quantitated by phosphate assay, and purity verified to be > 99% by thin-layer chromatography (TLC) of ~ 20 micrograms of lipid on washed and activated Adsorbosil TLC plates (Alltech, Deerfield, IL),

developed in a solvent system chloroform/methanol/water (65/25/4). Cholesterol stocks were prepared analytically and purity checked with TLC in petroleum ether/diethyl ether/chloroform (7/3/3). Fluorescent dyes were checked for purity with the following solvent systems: BoDIPY-PC in chloroform/methanol/water (65/25/4); C12:0-DiI in chloroform/methanol (10/1); C20:0-DiI in petroleum ether/diethyl ether/chloroform (7/3/3); and TOE in hexane/ethyl acetate (3/1). Concentrations of fluorescent dyes were measured by absorption spectroscopy using an HP 8452A spectrophotometer (Hewlett-Packard, Palo Alto, CA).

### 3.3.2 Terminology

Whereas at constant temperature the ternary mixture phase behavior is conveniently represented in the plane of a Gibbs Triangle, quaternary mixture phase behavior is best shown in the volume of a tetrahedron. Our construction of the quaternary phase diagram begins with the two ternary mixtures DSPC/DOPC/chol [4] and DSPC/POPC/chol [7] that form two triangular faces of the tetrahedron for DSPC/DOPC/POPC/chol. The tetrahedral phase diagram can be thought of as the locus of all phase observations traveling through composition space from one ternary mixture to the other, replacing POPC by DOPC. We find it convenient to refer to compositions within the tetrahedron between DOPC-containing and POPC-containing triangular faces in terms of the fractional replacement of POPC by DOPC,  $\rho \equiv [\text{DOPC}]/([\text{DOPC}] + [\text{POPC}])$ . Thus, the POPC-containing face of the tetrahedron has  $\rho = 0$ , whereas the DOPC-containing face has  $\rho = 1$ .

We use the term “trajectory” to mean a series of samples along a specified path of compositions. Trajectories are used to examine the compositional dependence of a measurement such as fluorescence; in this study, trajectories were used to find the dependence of phase boundaries on  $\rho$ , that is, to connect the 3-component phase diagrams previously determined at  $\rho =$

0 and 1 [4, 7]. Concentrations of mixture components are specified as a mole fraction (e.g.,  $\chi_{\text{DSPC}}$ ). We note that the mixtures studied here should be considered pseudo-quaternary because we neglect all components of the aqueous buffer. Most important, we neglect water on the basis that its chemical potential is constant at every lipid composition examined because of the presence of excess water. Even so, the water composition of each phase varies over the phase diagram, and we do not measure its fraction in any of the phases.

Fluorescent dyes can provide a unique signal of their local environment, for example, by a change in wavelength or intensity in different phase environments. Here we make use of changes in FRET as donor and acceptor dyes partition between coexisting phases. When dyes concentrate within the same phase, their average separation distance decreases, resulting in a compositional region of enhanced FRET efficiency (REE). When dyes prefer different phases, the increase in average dye separation distance leads to a region of reduced FRET efficiency (RRE). We used the donor/acceptor FRET dye pair DHE/BoDIPY-PC (which partition into  $L_o$  and  $L_d$  phase, respectively) to generate RREs when  $L_d$  and  $L_o$  phases coexist. In a second type of experiment, described below in more detail, we used the FRET pair TOE/BoDIPY-PC (both of which partition strongly into the  $L_d$  phase) to generate REEs, but with an additional dye, C12:0-DiI, added to the energy transfer chain. C12:0-DiI also partitions strongly into the  $L_d$  phase, and accepts energy selectively from BoDIPY-PC. This “3-dye method” can be especially sensitive, in at least some regions of the phase diagram, to the formation of a small fraction of  $L_d$  phase.

### 3.4 FRET

We used FRET to find many of the phase boundaries in the quaternary phase diagram. All samples for FRET measurement were prepared by use of rapid solvent exchange (RSE) to minimize cholesterol de-mixing [28]. Lipids and dyes were dispensed into glass tubes with a 25  $\mu$ L Hamilton syringe attached to a repeating dispenser (Hamilton USA, Reno, NV). RSE buffer (0.500 mL, 200 mM KCl, 5 mM PIPES, 1 mM EDTA, pH 7.0) was added to the chloroform solution of lipids and dyes. Samples were vortexed while vacuum pumping for 1 min, sealed under argon and placed in a water bath at 60  $^{\circ}$ C. Samples were cooled at 2  $^{\circ}$ C/h to 23  $^{\circ}$ C and equilibrated at room temperature for 48 h before measurements. 1.90 mL of RSE buffer was added to 0.100 mL of sample to yield 25  $\mu$ M lipid vesicles in the cuvette. Data were collected on a Hitachi F-7000 FL spectrofluorimeter (Hitachi High Technologies America, Schaumburg, IL) at an ambient temperature of 23 $^{\circ}$ C.

Samples contained 250 nmol of the lipid mixture. Dye concentrations were 0.5 mol% for DHE and 0.05 mol% for BoDIPY-PC. Using 2.5 nm bandpass for excitation and emission slits and 10 s integration time, intensity was measured in six channels (ex/em): DHE fluorescence (327/393 nm), BoDIPY-PC sensitized emission (327/517 nm), BoDIPY-PC direct fluorescence (500/517 nm), and light scattering (440/430 nm). For the 3-dye experiment, dye concentrations were 0.7 mol% for TOE, 0.07 mol% for BoDIPY-PC, and 0.05 mol% for C12:0-DiI. Fluorescence was measured in six ex/em channels using 2.5 nm bandpass slits and 10 s integration time. TOE fluorescence was measured at (280/340 nm), BoDIPY-PC sensitized emission at (280/516 nm), BoDIPY-PC direct fluorescence (509/516 nm), C12:0-DiI sensitized emission (509/575 nm), C12:0-DiI direct fluorescence (549/575 nm), and vesicle light scattering (440/430 nm). Control

samples were prepared to correct for non-FRET contributions as described previously [7, 28]. Briefly, corrections account for non-FRET contributions of direct fluorescence emission from donor and acceptor, and scattering of excitation light by the vesicle suspension.

### **3.5 GUV imaging**

#### **3.5.1 GUVs preparation by electroswelling**

GUVs were prepared by the method of “electroswelling” [29, 30]. Briefly, each sample contained 250 nmol of a lipid mixture in 200  $\mu$ L chloroform, with 0.02 mol% C12:0-DiI. A lipid film was created by evenly dispersing the chloroform solution onto indium tin oxide (ITO)-coated microscope slides (Delta Technologies, Stillwater, MN) on a hotplate set at 55 °C. After the residual solvent was removed under vacuum, ITO slides were sealed with Buna-N O-rings to create a chamber and filled with 100 mM sucrose solution. The films were incubated for 2 h at 55 °C with an AC field of 5 Hz,  $\pm$  1 Vpp, using a Wavetek FG2C function generator (Meterman, Everett, WA) and Digi-sense temperature controller R/S (Cole Palmer, Vernon Hills, IL) to produce GUVs, followed by a 10 h cooling period. GUVs were harvested into 100 mM glucose solution and allowed to settle for 1 h before microscopy observations at 23°C.

#### **3.5.2 Fluorescence microscopy**

A Nikon Diaphot-TMD microscope (Micro Video Instruments Inc., Avon, MA) was used for wide-field fluorescence microscopy at 23°C, using a 60X 1.4 NA oil immersion objective. BoDIPY-PC and C20:0-DiI (at 0.02 mol%) were chosen as a dye pair with different phase partitioning: in DSPC-containing mixtures, BoDIPY-PC partitions into the Ld phase whereas C20:0-DiI prefers DSPC-rich Lo and L $\beta$  phases over disordered phases [4]. GUVs in the Ld + Lo

region were imaged with BoDIPY-PC and naphthopyrene dyes at 0.02 and 0.033 mol%, respectively. In this system, naphthopyrene partitions into the Lo phase over the Ld phase. GUVs exhibiting spatially modulated Ld + Lo phase domains were also imaged with complementary BoDIPY-PC and naphthopyrene dyes. For critical point investigation, GUVs were labeled with C12:0-DiI at 0.02 mol%. We used a combination of tactics to minimize light-induced artifacts [5]: low exposure times (100-300 ms); neutral density filters at OD = 1.0; and minimizing sample exposure to light by using dim halogen transmitted light to locate and focus on GUVs [30]. Images were taken with a Photometrics charge-coupled device camera CoolSNAP HQ2 (Tucson, Arizona). C12:0-DiI and C20:0-DiI dyes were imaged with ex/em 540-552 nm/565-605 nm; BoDIPY-PC 460-500 nm/515-560 nm; naphthopyrene 426-446 nm/460-500 nm. Images from GUVs containing multiple dyes were color-merged using NIS software: BoDIPY-PC green, C20:0-DiI and C12:0-DiI red, and naphthopyrene blue. Image contrast was enhanced with NIS Elements Basic Research Software (MVI, Inc.).

### **3.5.3 Critical point investigation and percolation map**

The critical point at  $\rho = 1$  was previously determined by Heberle et al. [7] to be at DSPC/DOPC/chol = 0.26/0.34/0.40. Critical points for  $\rho = 0.50$  and  $\rho = 0.70$  were experimentally determined in this study by determining the continuous (percolating) phase as a function of composition to obtain a percolation map. The region of the Ld + Lo percolation map near the critical point was constructed for  $\rho = 0.50$  and  $\rho = 0.70$ , by analyzing on average ~100 GUVs at each composition. The locus of compositions for which connectivity in GUVs changes from Ld to

Lo was extrapolated to its intersection with the previously determined Ld + Lo upper phase boundary, thereby marking the critical point at these  $\rho$  values.

### **3.6 Constructing 4-component phase diagrams**

The 3-dimensional model of the 4-component phase diagram was developed using Environmental Systems Research Institute's (ESRI) ArcGIS for Desktop Advanced software suite version 10.1 (Redlands, California), a geographic information system designed to view and manipulate spatial data. The primary modeling environment was the 3D visualization application ArcScene. A spherical coordinate system was used to derive a relative frame of reference for each component of the phase diagram. Data were imported into an undefined coordinate system in ArcScene as XYZ point cloud data that were then manually edited into vector geometry, specifically line and polygon feature classes. The resulting 3-dimensional 4-component model is interactive and rotatable, with all phase volumes and the bounding tetrahedron independent of one another including adjustment of chromaticity, illumination, and transparency. Individual 2D phase diagrams, corresponding to faces of tetrahedron and slices at various  $\rho$  values, were constructed using Mathematica 7 (Wolfram Research, Champaign, IL).

## **3.7 Results**

### **3.7.1 2-dye FRET: DHE $\rightarrow$ BoDIPY-PC**

Trajectories T1 and T2 were used to locate the upper boundary of region 5 between  $\rho = 0$  and 1. (See Fig. 3.1 legend for detailed description of trajectories and their endpoints). Within the Ld + Lo coexistence region, the dyes separate from each other and the FRET signal decreases. In

favorable cases, depending on the lipid mixture and location of the trajectories in composition space, the change in slope of the FRET signal is significant and easily identified when the phase boundary is crossed. Fig. 3.1 shows the locations of trajectories T1-T6 (panels A and B) and  $\rho$  planes (panel C) within the composition space. Figs. 3.2 and 3.3 show 2-dye FRET data for trajectories T1 and T2, respectively, used to find phase boundaries at different  $\rho$  values. Table 3.1 summarizes boundary compositions in terms of component mole fractions.

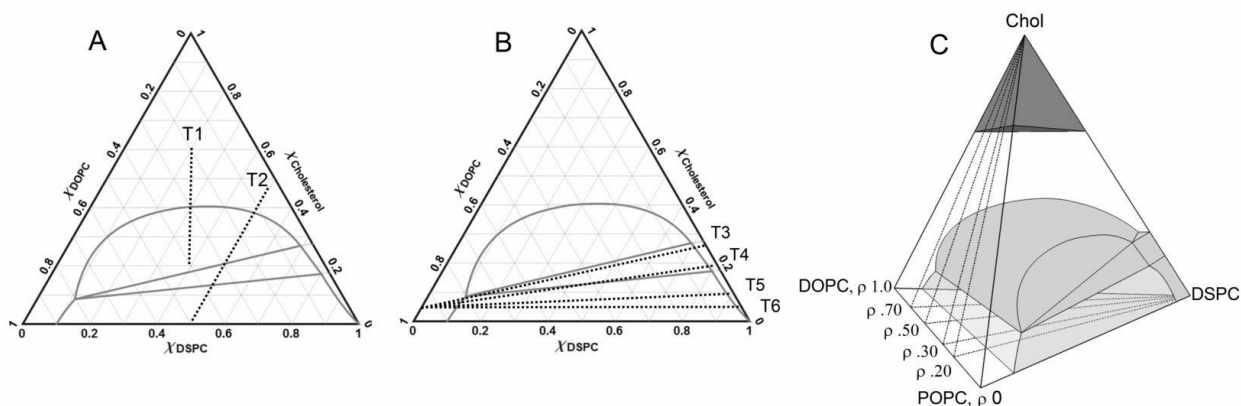


**Figure 3.1** Compositional trajectories (dashed lines) T1-T6 are located in the 4-component phase diagram. (A) 2-dye trajectories T1-T2; T1 is along  $0.20 \leq \chi_{DSPC} \leq 0.40$  between cholesterol concentration  $0.20$  or  $0.25 \leq \chi_{CHOL} \leq 0.50$  or  $0.60$  at  $\rho$  values  $0, 0.30, 0.50, 0.70,$  and  $1.0$ ; T2 is along constant  $\chi_{DSPC} = 0.50$  and cholesterol concentration  $0 \leq \chi_{CHOL} \leq 0.45$  at  $\rho$  values  $0, 0.30, 0.50, 0.70$ . For convenience, T1 and T2 are only shown at  $\rho = 1.0$  and boundaries for DSPC/DOPC/Chol are drawn (solid lines); (B) 3-dye trajectories T3-T6 (dashed lines). T3 is  $0 \leq \chi_{DSPC} \leq 0.732$  and  $0.054 \leq \chi_{CHOL} \leq 0.268$ ; T4 is  $0 \leq \chi_{DSPC} \leq 0.80$  and  $0.054 \leq \chi_{CHOL} \leq 0.20$ ; T5 is  $0 \leq \chi_{DSPC} \leq 0.90$  and  $0.054 \leq \chi_{CHOL} \leq 0.10$ ; T6 is  $0 \leq \chi_{DSPC} \leq 0.95$  and  $0.054 \leq \chi_{CHOL} \leq 0.05$ . All trajectories were prepared at  $\rho$  values  $0, 0.20$  or  $0.30, 0.50, 0.70,$  and  $1.0$ ; (C) Placement of  $\rho$  “slices” within the quaternary phase diagram. All  $\rho$  slices share common Chol and DSPC endpoints, with varying  $\rho = [DOPC]/([DOPC] + [POPC])$ .

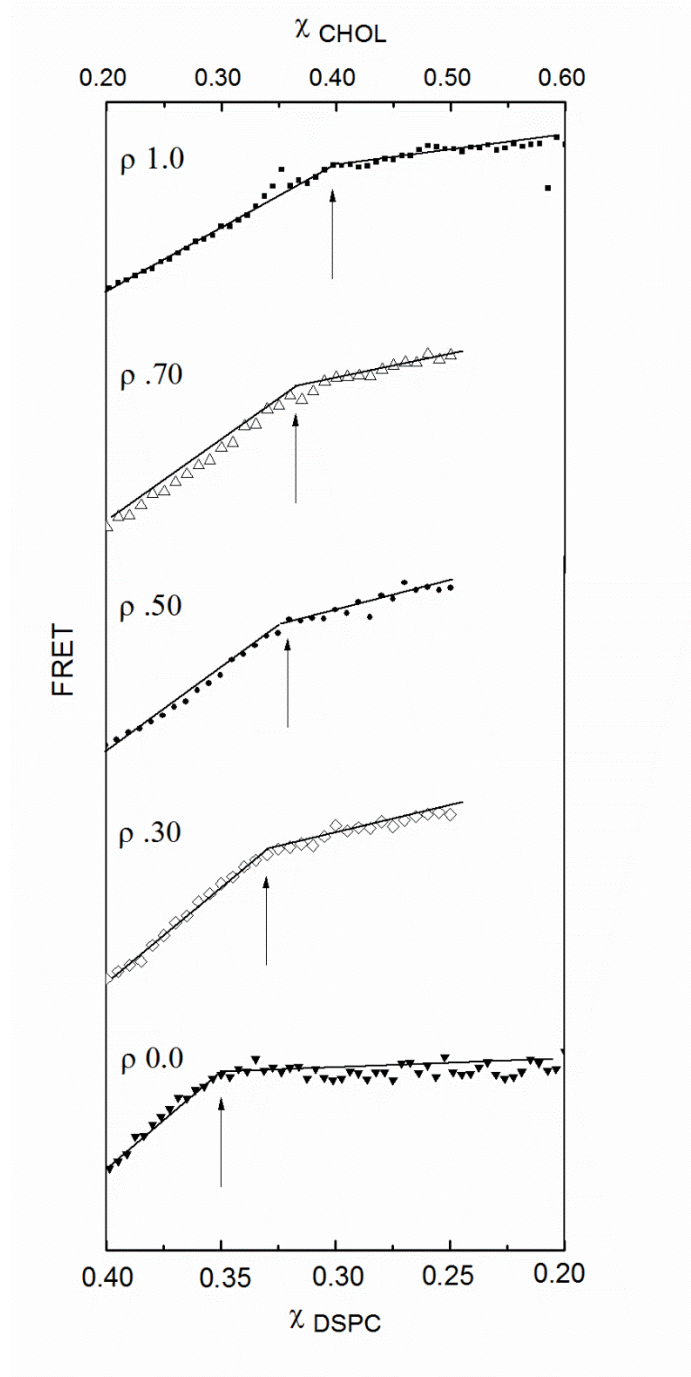


**Figure 3.2** Upper boundaries of the Ld + Lo region change smoothly from  $\rho = 0$  to 1 along T1. Panels show FRET along T1 using 2-dye pair DHE  $\rightarrow$  BoDIPY-PC to locate boundaries. FRET changes abruptly at the onset of a phase transition, allowing precise boundary determination (solid lines show fit for slope change). Arrows show location of the phase boundary where Ld + Lo phase coexistence appears/disappears.

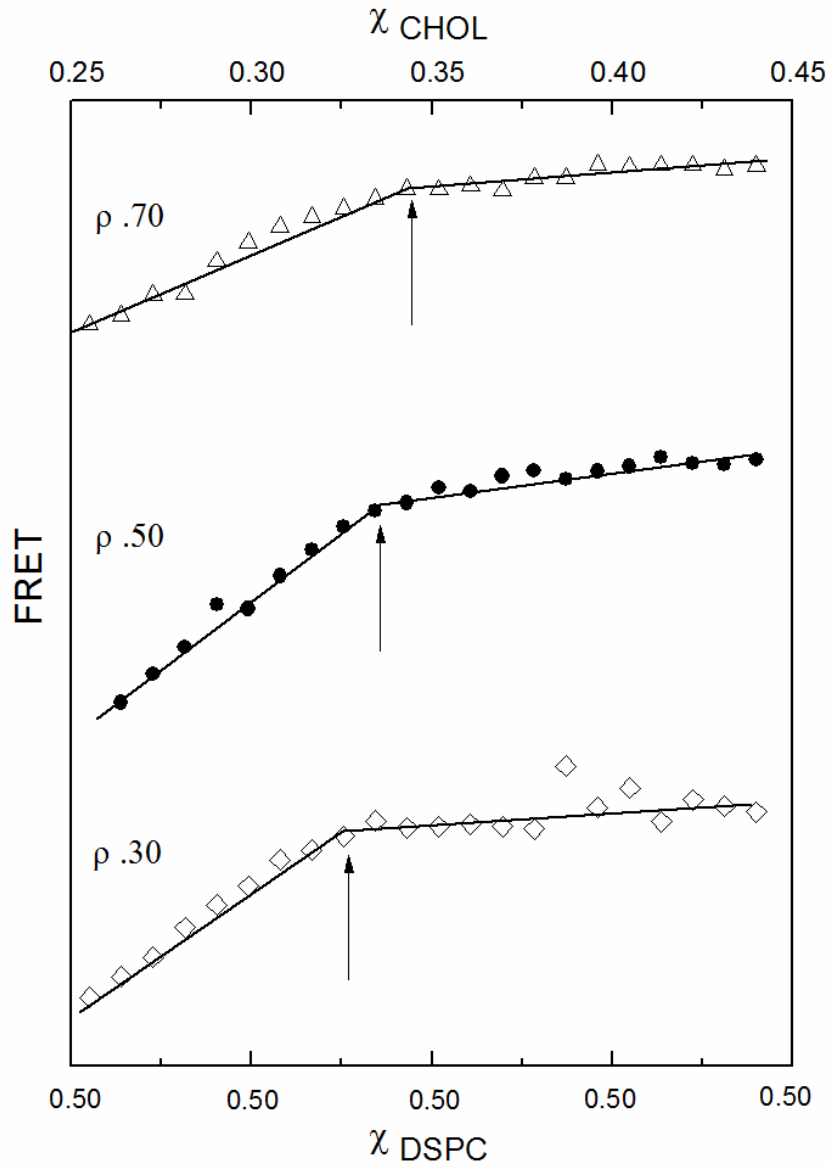


**Figure 3.3** Upper-RHS boundaries of the Ld + Lo region change smoothly with  $\rho$  along T2. Panels show FRET along T2 using DHE  $\rightarrow$  BoDIPY-PC to locate boundaries at  $\rho = 0.70, 0.50$  and  $0.30$ . Arrows show location of the boundary, which shifts smoothly between  $\rho = 0$  to  $1$ .

	$\rho =$	1.0	.70	.50	.30	.20	0
T1 <sup>a</sup>	$\chi_{DSPC}$	0.30	0.31	0.32	0.33	--	0.35
	$\chi_{DOPC}$	0.30	0.22	0.16	0.099	--	0.0
	$\chi_{POPC}$	0.0	0.090	0.16	0.231	--	0.35
	$\chi_{Chol}$	0.40	0.38	0.36	0.34	--	0.30

	$\rho =$	1.0	.70	.50	.30	.20	0
T5 <sup>e</sup>	$\chi_{DSPC}$	0.87	0.87	0.87	0.85	--	0.83
	$\chi_{DOPC}$	0.031	0.0217	0.0155	0.0364	--	0
	$\chi_{POPC}$	0	0.0093	0.0155	0.0156	--	0.073
	$\chi_{Chol}$	0.099	0.099	0.099	0.098	--	0.097

	$\rho =$	1.0	.70	.50	.30	.20	0
T2 <sup>b</sup>	$\chi_{DSPC}$	--	0.50	0.50	0.50	--	--
	$\chi_{DOPC}$	--	0.11	0.085	0.050	--	--
	$\chi_{POPC}$	--	0.050	0.085	0.13	--	--
	$\chi_{Chol}$	--	0.34	0.33	0.32	--	--

	$\rho =$	1.0	.70	.50	.30	.20	0
T6 <sup>f</sup>	$\chi_{DSPC}$	0.93	0.91	0.91	--	0.89	0.88
	$\chi_{DOPC}$	0.020	0.028	0.020	--	0.012	0.0
	$\chi_{POPC}$	0.0	0.012	0.020	--	0.048	0.070
	$\chi_{Chol}$	0.050	0.050	0.050	--	0.050	0.050

	$\rho =$	1.0	.70	.50	.30	.20	0
T3 <sup>c</sup>	$\chi_{DSPC}$	0.71	0.68	0.67	--	0.64	0.63
	$\chi_{DOPC}$	0.030	0.049	0.040	--	0.024	0.0
	$\chi_{POPC}$	0.0	0.021	0.040	--	0.096	0.13
	$\chi_{Chol}$	0.26	0.25	0.25	--	0.24	0.24

	$\rho =$	.70	.50	0
Critical points <sup>g</sup>	$\chi_{DSPC}$	0.24	0.22	0.18
	$\chi_{DOPC}$	0.12	0.22	0.0
	$\chi_{POPC}$	0.27	0.22	0.54
	$\chi_{Chol}$	0.37	0.34	0.28

	$\rho =$	1.0	.70	.50	.30	.20	0
T4 <sup>d</sup>	$\chi_{DSPC}$	0.78	0.76	0.75	--	--	0.69
	$\chi_{DOPC}$	0.030	0.035	0.030	--	--	0.0
	$\chi_{POPC}$	0.0	0.015	0.030	--	--	0.13
	$\chi_{Chol}$	0.19	0.19	0.19	--	--	0.18

**Table 3.1** <sup>(a-f)</sup> Coordinates for boundaries for all  $\rho$  values along T1-T6, in terms of  $\chi_{DSPC}$ ,  $\chi_{DOPC}$ ,  $\chi_{POPC}$  and  $\chi_{Chol}$ , and <sup>(g)</sup> locations for critical points at  $\rho = .70$ ,  $\rho = 0.50$ , and  $\rho = 0$ , in terms of  $\chi_{DSPC}$ ,  $\chi_{DOPC}$ ,  $\chi_{POPC}$  and  $\chi_{Chol}$ .

### 3.7.2 3-dye FRET: TOE $\rightarrow$ BoDIPY-PC $\rightarrow$ C12:0-DiI

The 2-dye FRET method mentioned in the previous section was developed to allow for unambiguous determination of phase boundaries by visual inspection [31]. The method exploits the highly nonlinear concentration variation, along a tieline, of dyes that partition strongly between coexisting phases. In many cases, there is an abrupt change in sensitized acceptor emission (SAE) at one or both phase boundaries—this is especially true when SAE shows little variation within the single phase regions. For many years our studies of phase behavior yielded imprecise results for

some phase boundaries close to the binary axis of high-melting lipid/chol, primarily due to a steep compositional dependence of SAE for Ld-preferring dyes in single-phase gel and Lo regions. This steep dependence may be due in part to highly nonideal mixing of these probes in an unfavorable ordered environment. In these cases, the change in slope at the phase boundary is often subtle, and easily obscured by limited compositional resolution and experimental noise.

We have developed a new method that circumvents this problem by addition of a third dye that (i) partitions strongly into Ld, and (ii) selectively accepts energy from the second dye (i.e., the original FRET acceptor in the 2-dye experiment). SAE of the second dye is reduced by the presence of the third dye, in direct proportion to the transfer efficiency  $E_{2\rightarrow3}$ . Crucially,  $E_{2\rightarrow3}$  is highly nonlinear along a tieline, particularly near the ordered phase boundary, where the probes are concentrated in the Ld phase. By varying the concentration of the third dye, the slope near the Lo boundary can be “tuned” to contrast strongly with the adjacent single phase Lo or gel region. A quantitative model for this behavior is developed in the Appendix, and a description of how a two-dye SAE curve is systematically altered by addition of the third dye is provided in the Supporting Information.

We measured sensitized emission of BoDIPY-PC upon selective illumination of TOE, with C12:0-DiI added to quench BoDIPY-PC fluorescence *via* FRET. A series of different trajectories was prepared, each with 50 samples along with additional appropriate controls, labeled as T3-T6. (See Fig. 3.1 legend for a description of trajectories and their endpoints). Trajectories were prepared at  $\rho = 0, 0.20$  or  $0.30, 0.50, 0.70,$  and  $1$  (Figs. 3.1B and 3.1C). At sufficiently high concentration of C12:0-DiI (0.05 mol%), the ordered (Lo or gel) boundary is clearly observed as a drop in BoDIPY-PC fluorescence upon crossing the phase boundary from the single phase (Lo or gel) region.

SAE data shown in Figs. 3.4 (trajectory T3) and S1-S3 (trajectories T4-T6) were fit to Eq. 3.A.9. Arrows indicate locations of the boundaries determined by visual inspection. Table 3.1 summarizes the boundary locations for all trajectories. We find that RHS boundaries shift to lower  $\chi_{\text{DSPC}}$  as DOPC is replaced with POPC: A smooth monotonic shift is apparent for all trajectories T3-T6, consistent with better mixing of DSPC in POPC than in DOPC. Fig. 3.5 summarizes the phase boundary shift as DOPC is replaced with POPC, revealing the shape of the volume between  $\rho = 0$  and 1.

In addition to the thousands of samples covering the entire composition space needed originally to solve the phase diagrams of DSPC/DOPC/chol [4] and DSPC/POPC/chol [7], targeted linear sample trajectories were useful for precisely locating boundaries. The 3-dye method was useful for determining the RHS boundaries. Based on the analysis of these data, we found that relatively small adjustments should be made to our previously published 3-component phase diagrams [4, 7].

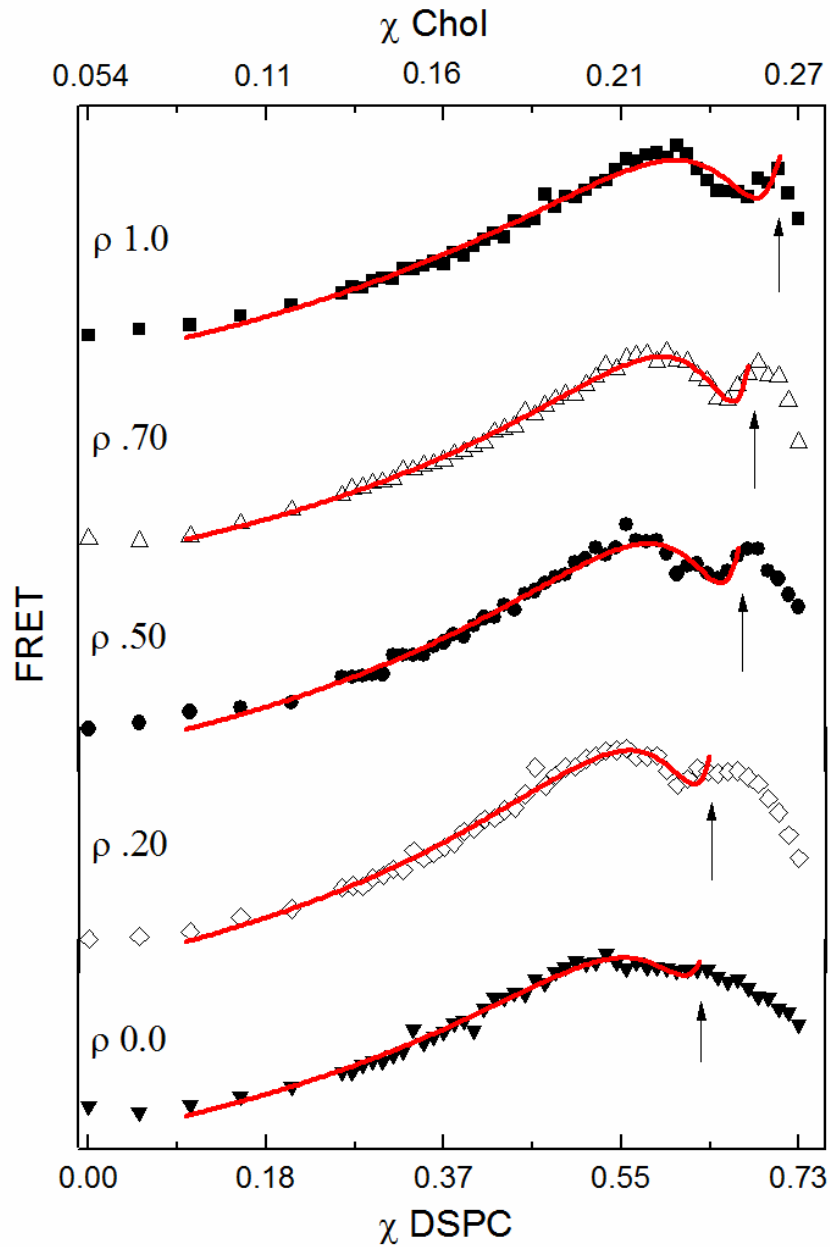


**Figure 3.4** RHS boundaries along T3 are precisely detected by use of 3-dye FRET TOE $\rightarrow$ BoDIPY-PC $\rightarrow$ C12:0-DiI data along T3 from  $\rho = 0$  to 1. Arrows show location of the RHS boundary of Ld + Lo coexistence for each  $\rho$  value. At low  $\rho$  values this boundary is much less sharp. Data for T4-T6 are shown in Figs. 3.10-3.12. Solid lines represent fits to Eq. 3.A.9, as described in Appendix and Supporting Materials.

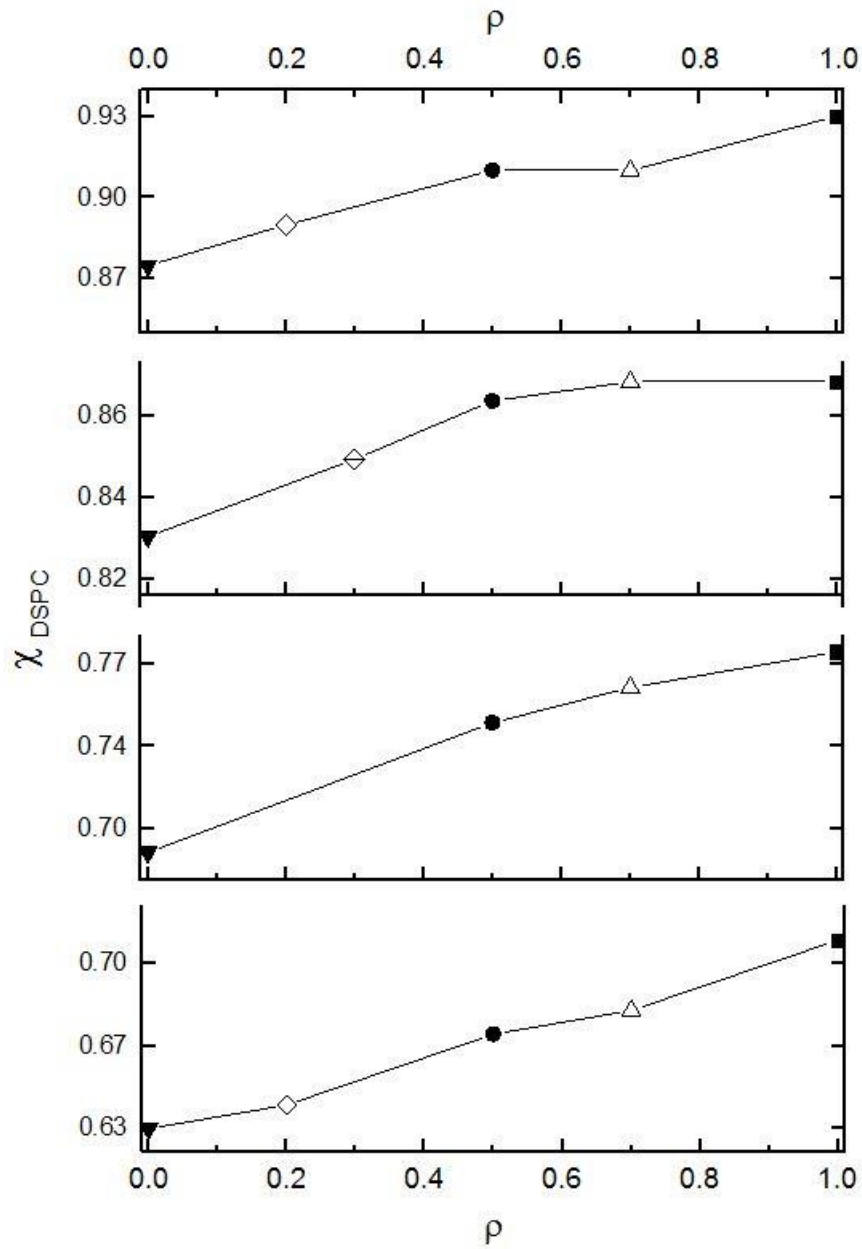


**Figure 3.5** All RHS phase region boundaries shift smoothly as  $\rho$  changes from 0 to 1 along T3-T6. Boundary locations are described by  $\chi_{\text{DSPC}}$ . Filled squares,  $\rho = 1.0$  for T3-T6; open triangles,  $\rho = 0.70$  for T3-T6; filled circles,  $\rho = 0.50$  for T3-T6; diamonds with line,  $\rho = 0.30$  for T4 and T5; open diamonds,  $\rho = 0.20$  for T3 and T6; filled triangles,  $\rho = 0$  for T3-T6.

### 3.8 Microscopy of GUVs

#### 3.8.1 Phases observed by GUVs

We are especially interested in the transition through the region of modulated phases [23, 24] from macroscopic to nanoscopic size scales. Representative GUV images are shown in Fig. 3.6: (A) macroscopic Ld + Lo coexistence at  $\rho = 1$ ; (B) nanoscopic Ld + Lo coexistence at  $\rho = 0$ , and (C) modulated morphology at  $\rho = 0.2$ . Fig. 3.6D is a representative image for the Ld + L $\beta$  phase region. We have previously found that Ld + L $\beta$  domains are macroscopic at all  $\rho$  values [4].

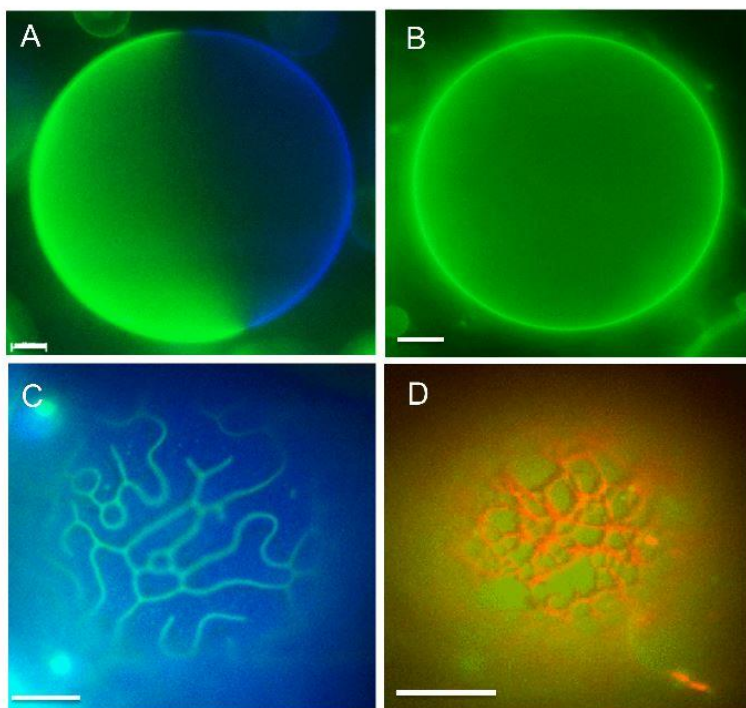


**Figure 3.6** GUV images identify phase regions at various compositions of DSPC/DOPC/POPC/chol. (A) macroscopic Ld + Lo coexistence at 0.45/0.30/0/0.25; (B) nanoscopic Ld + Lo coexistence at 0.45/0/0.30/0.25; (C) modulated phase morphology at 0.45/0.06/0.24/0.25; (D) Ld + L $\beta$  phase coexistence at 0.45/0.50/0/0.05. Images are color-merged using Nikon multichannel acquisition: C20:0-DiI (red), BoDIPY-PC (green), and naphthopyrene (blue). Temperature 23 °C. Scale bar 10 microns.

### 3.8.2 Percolation map and critical points

Critical points for  $\rho = 0.50$  and  $0.70$  were determined as described in section 3.5.3. GUVs near the critical point exhibited irregular domain boundaries, consistent with proximity to a critical point. Critical points (stars) for  $\rho = 0.50$  and  $0.70$  were found at DSPC/DOPC/POPC/chol =  $0.22/0.22/0.22/0.34$  and  $0.24/0.12/0.27/0.37$ , respectively (Fig. 3.7). Locations of critical points are summarized in Table 3.1. The  $\rho = 1$  critical point was previously determined at DSPC/DOPC/chol =  $0.26/0.34/0.40$  [7]. By extrapolating a line connecting these three experimentally determined points, we estimate the critical point at  $\rho = 0$  to be at DSPC/POPC/chol =  $0.18/0.54/0.28$ .

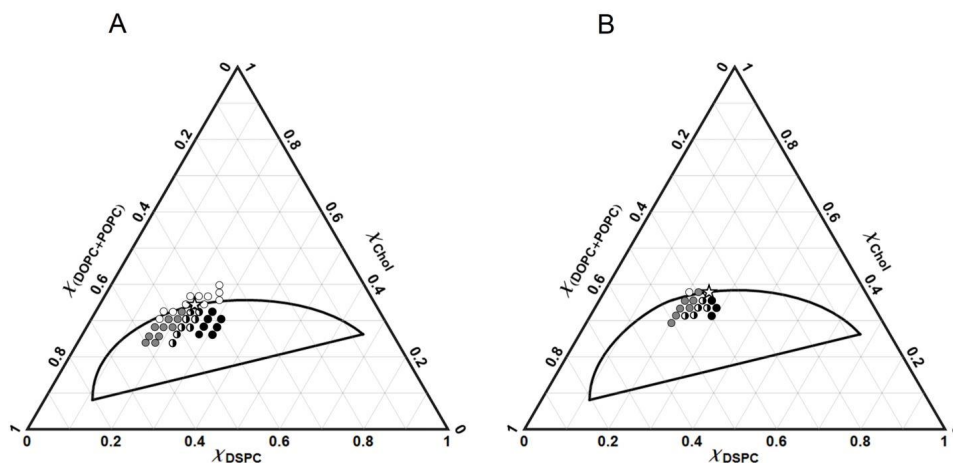


**Figure 3.7** Percolation maps enable finding critical points, marked by small stars for (A)  $\rho = 0.50$  and (B)  $\rho = 0.70$ . Boundaries for the Ld + Lo region are shown for reference. Filled circles, GUVs within Ld + Lo phase coexistence with Lo as the percolating phase; grey circles, Ld is the percolating phase; open circles, GUVs are uniform within a one phase region; half black/white circles, GUVs exhibiting both types of connectivity. Critical points, (A)  $0.22/0.22/0.22/0.34$ ; (B)  $0.24/0.117/0.273/0.37$ . Locations of critical points are summarized in Table 3.1. The  $\rho = 1.0$  critical point has been previously determined at DSPC/DOPC/chol =  $0.26/0.34/0.40$  [8]. By extrapolating a line connecting these three experimentally determined points, we estimate the critical point at  $\rho = 0$  to be at DSPC/POPC/chol =  $0.18/0.54/0.28$  (Fig. 3.9C and Table 3.1).

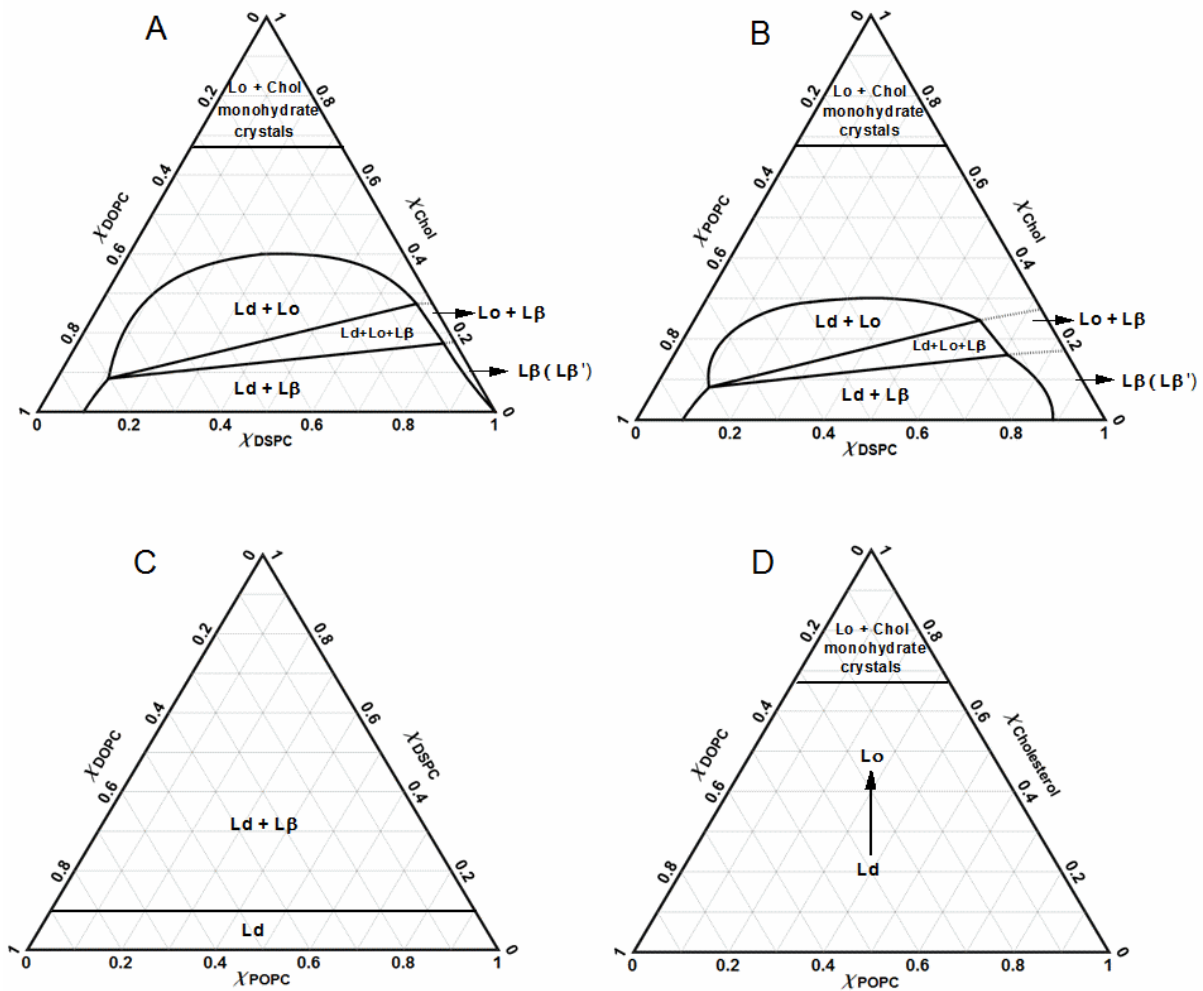
## 3.9 Discussion

### 3.9.1 Tour of the quaternary phase diagram

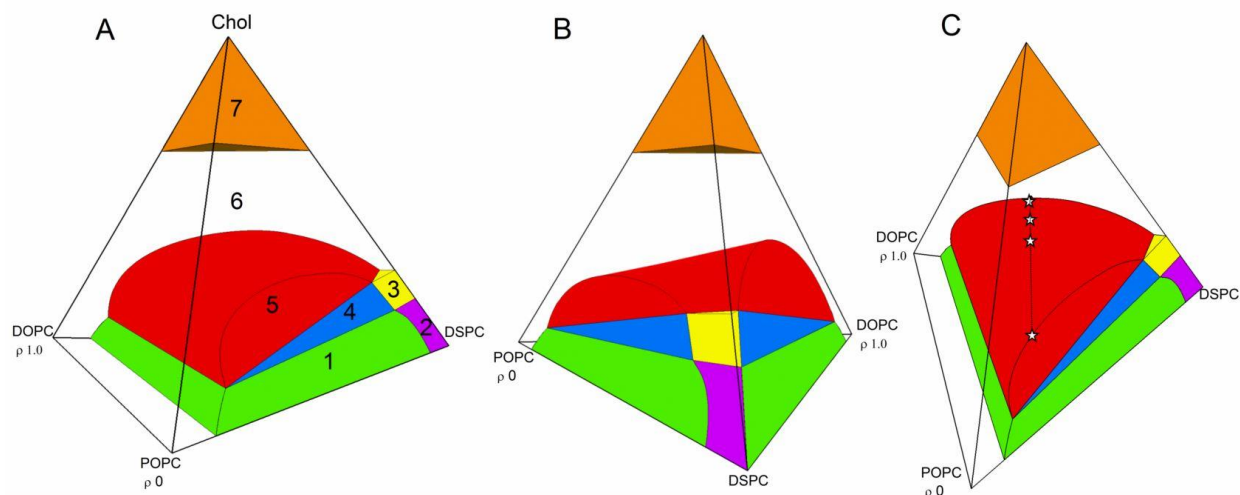
#### Overview of DSPC/DOPC/POPC/chol phase diagram

Fig. 3.8 shows each individual face of the DSPC/DOPC/POPC/chol phase diagram, and Fig. 3.14 shows planar sections through the phase diagram at  $\rho = 0.20$  (panel A),  $\rho = 0.50$  (panel B), and  $\rho = 0.70$  (panel C). The quaternary phase diagram for DSPC/DOPC/POPC/chol from three perspectives is shown in Fig. 3.9, and a stereoscopic 3D image is shown in Fig. 3.14. We describe below the 7 phase volumes (Fig. 3.9A) of DSPC/DOPC/POPC/chol, starting with the 4 individual ternary faces of the tetrahedron.

Ternary phase diagrams for DSPC/DOPC/chol and DSPC/POPC/chol were described previously [4, 6], but are shown here with some phase boundaries adjusted based on our new data. The ternary faces DSPC/DOPC/POPC (Fig. 3.8C) and DOPC/POPC/chol (Fig. 8D) show rather simple phase behavior. The boundary between Ld phase and coexisting Ld + L $\beta$  is found at  $\chi_{\text{DSPC}} = 0.10$  for all  $\rho$  values (Fig. 3.8C). Fig. 3.8D (the ternary phase diagram for DOPC/POPC/chol) illustrates the uniform transition from Ld to Lo in region 6, along with region 7 for  $\chi_{\text{CHOL}} > 0.67$ .



**Figure 3.8** The four faces of the DSPC/DOPC/POPC/chol tetrahedron are each 3-component phase diagrams. (A) DSPC/DOPC/chol; (B) DSPC/POPC/chol; (C) DSPC/DOPC/POPC; (D) DOPC/POPC/chol. Solid black lines are well-determined by experimental measurement, dashed lines show estimated boundaries.



**Figure 3.9** Tetrahedral phase diagram of DSPC/DOPC/POPC/chol with all phase volumes labeled. (A) region 1 (green), 2-phase Ld + L $\beta$  coexistence; region 2 (purple) 1-phase L $\beta$  (L $\beta'$ ); region 3 (yellow) 2-phase Lo + L $\beta$  becomes a continuous phase transition along the binary axis; region 4 (blue) 3-phase Lo + Ld + L $\beta$ ; region 5 (red) 2-phase Ld + Lo; region 6 (white) 1-phase varying continuously between Ld and Lo; region 7 (orange) 2-phase crystalline cholesterol monohydrate + cholesterol-saturated Lo phase; (B) clockwise rotation of (A) shows the smooth transition of the upper Ld + Lo boundary from the mixture containing POPC to that containing DOPC. (C) counterclockwise rotation and tilting of (B) shows the line of critical points (stars) along the upper boundary of Ld + Lo. Compositions of the critical points are given in Table 3.1.

### 3.9.2 4-component regions

#### 3.9.2.1 Liquid + gel coexistence, Ld + L $\beta$ ( $\beta'$ ), region 1

The upper boundary of region 1 is a plane that is also the lower boundary of the 3-phase coexistence region 4. The LHS boundary of Fig. 3.9A indicates the maximum solubility of DSPC at  $\chi_{\text{DSPC}} = 0.10$ , for both DOPC-rich and POPC-rich Ld phases. This boundary does not change as cholesterol concentration increases. The RHS boundary of region 1 shows that DOPC is rather insoluble in the DSPC-rich L $\beta'$  phase, with  $\chi_{\text{DOPC}} < 0.02$  without cholesterol; POPC is more soluble than DOPC in the DSPC-rich solid phase, with  $\chi_{\text{POPC}} \sim 0.11$  without cholesterol, as previously determined by differential scanning calorimetry [32]. As cholesterol concentration increases, only small changes occur in the RHS boundary, i.e. the solubility of POPC in the gel hardly changes,

and the solubility of DOPC only changes from  $\chi_{\text{DOPC}} < 0.02$  to about 0.03. The maximum solubility of cholesterol in the DSPC-rich  $L\beta$  phase is nearly the same at  $\chi_{\text{CHOL}} = 0.16-0.18$ , whether the  $L\beta$  phase contains  $\chi_{\text{DOPC}}$  at 0.03 or  $\chi_{\text{POPC}}$  at 0.11. We have found this same maximum solubility of cholesterol of  $\chi_{\text{CHOL}} \sim 0.17$  for these two  $L\beta$  phase mixtures, as well as for  $L\beta$  phases of DPPC/DLPC [6], brain sphingomyelin (bSM)/DOPC [8] and bSM/POPC [8].

### 3.9.2.2 Gel [ $L\beta(L\beta')$ ], region 2

The pure hydrated lipid DSPC at 23 °C is a solid with tilted chains,  $L\beta'$ . As found for DPPC, addition of cholesterol causes the chain tilt to disappear but without the formation of a coexisting phase, i.e. a continuous phase transition occurs in region 2, with  $L\beta$  forming from  $L\beta'$  [6]. Region 2 is thus bounded at  $\chi_{\text{DOPC}} = 0.03$ ,  $\chi_{\text{POPC}} = 0.11$ , and  $\chi_{\text{CHOL}} \sim 0.17$ .

### 3.9.2.3 Liquid-ordered + gel coexistence, $Lo + L\beta$ , region 3

This wedge-shaped region has one edge along the DSPC/chol binary axis from  $\chi_{\text{CHOL}} \sim 0.18-0.27$ . Along this axis,  $L\beta$  transitions to  $Lo$  with increasing cholesterol fraction, but without evidence of coexisting phases (i.e., a continuous phase change). Away from this binary axis, as low-melting PC increases in the mixture, coexisting phases appear. The upper and lower boundaries of region 3 are not well defined by our data. Instead, these boundaries, which connect to the lower and upper boundaries of region 4, were chosen to be in agreement with Schreinemakers' Rules [33].

#### **3.9.2.4 3-phase coexistence, Ld + Lo+ L $\beta$ , region 4**

3-dye data for trajectories T3 and T4 (Figs. 3.4 and 3.10, respectively) were used to determine the RHS boundaries of this volume at five  $\rho$  values: 0, 0.20, 0.30, 0.50, 0.70, and 1. Remarkably, the upper and lower planes that bound region 4 do not change from POPC-containing mixtures to DOPC-containing mixtures, although the RHS boundaries do change with  $\rho$ . For all values of  $\rho$ , the Lo phase that separates has  $\chi_{\text{CHOL}} \sim 0.25\text{-}0.27$ . The solubility of DSPC in both POPC/chol and DOPC/chol mixtures is the same, and the solubility of chol in the L $\beta$  phase that contains either POPC or DOPC is also nearly the same. Together, these behaviors yield the remarkable observation that the upper and lower boundaries of the three phase region are essentially independent of  $\rho$ . These boundary planes are immensely useful because they contain thermodynamic tielines.

#### **3.9.2.5 Liquid–liquid coexistence, Ld + Lo, region 5**

The upper DSPC/DOPC/chol boundary terminates at a maximum  $\chi_{\text{CHOL}} \sim 0.40$ , whereas that of DSPC/POPC/chol terminates at  $\chi_{\text{CHOL}} \sim 0.30$ . A smaller region of immiscibility indicates better mixing of both DSPC and cholesterol with POPC. The upper boundary is established by FRET trajectories (T1 and T2) using the donor/acceptor pair DHE/BoDIPY-PC (Figs. 3.2 and 3.3).

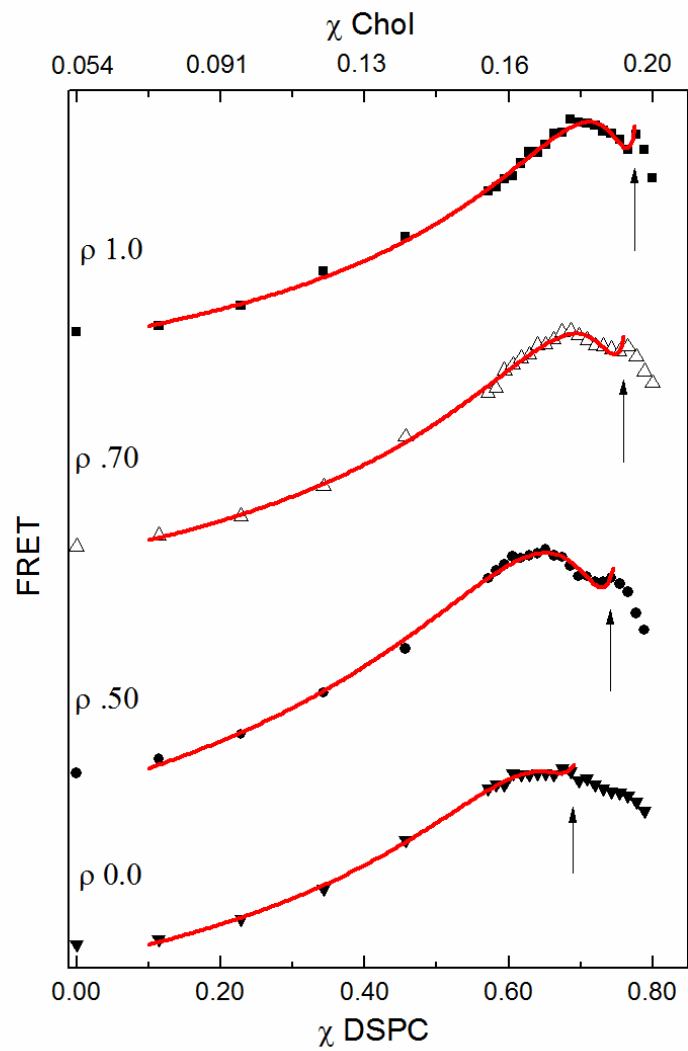


**Figure 3.10** Location of RHS boundaries along T4 by use of the 3-dye method; 5 panels represent 3-dye FRET TOE $\rightarrow$ BoDIPY-PC $\rightarrow$  C12:0-DiI data at  $\rho = 1.0, 0.70, 0.50, 0.30$  and  $0$ . Arrows show location of the boundary. Solid lines correspond to fits to Eq. 3.A.9 as described Supporting sections.

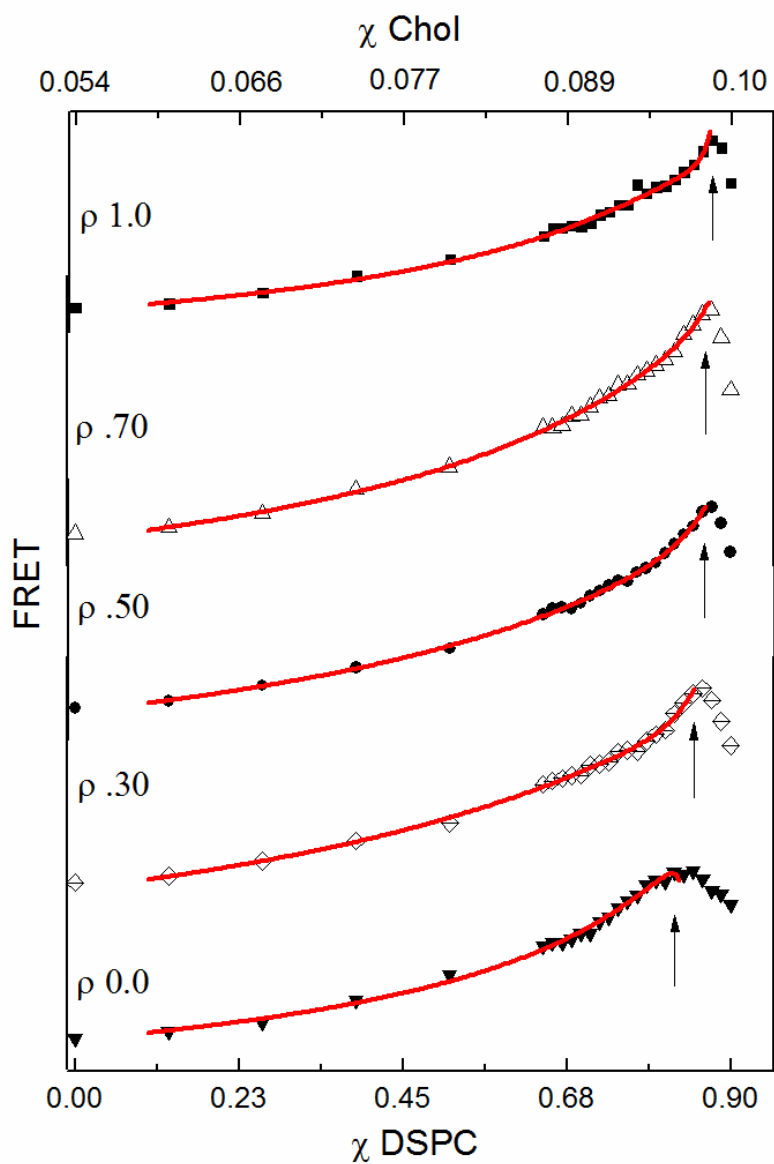


**Figure 3.11** Location of RHS boundaries along T5 by use of the 3-dye method; 5 panels represent 3-dye FRET TOE $\rightarrow$ BoDIPY-PC $\rightarrow$  C12:0-DiI data at  $\rho = 1.0, 0.70, 0.50, 0.30$  and  $0$ . Arrows show location of the boundary. Solid lines correspond to fits to Eq. 3.A.9, as described in Supporting sections.

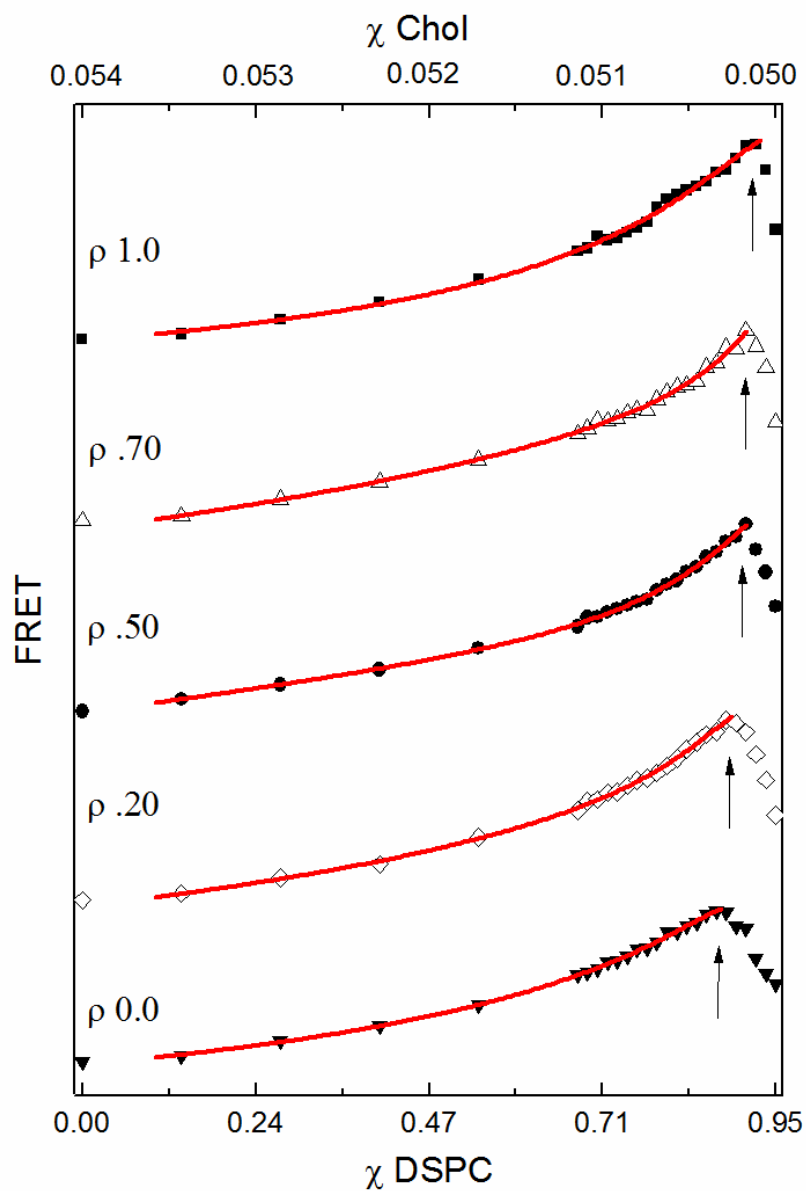


**Figure 3.12** Location of RHS boundaries along T6 by use of the 3-dye method; 5 panels represent 3-dye FRET TOE→BoDIPY-PC→ C12:0-DiI data at  $\rho = 1.0, 0.70, 0.50, 0.20$  and  $0$ . Arrows show location of the boundary. Solid lines correspond to fits to Eq. 3.A.9, as described Supporting sections.

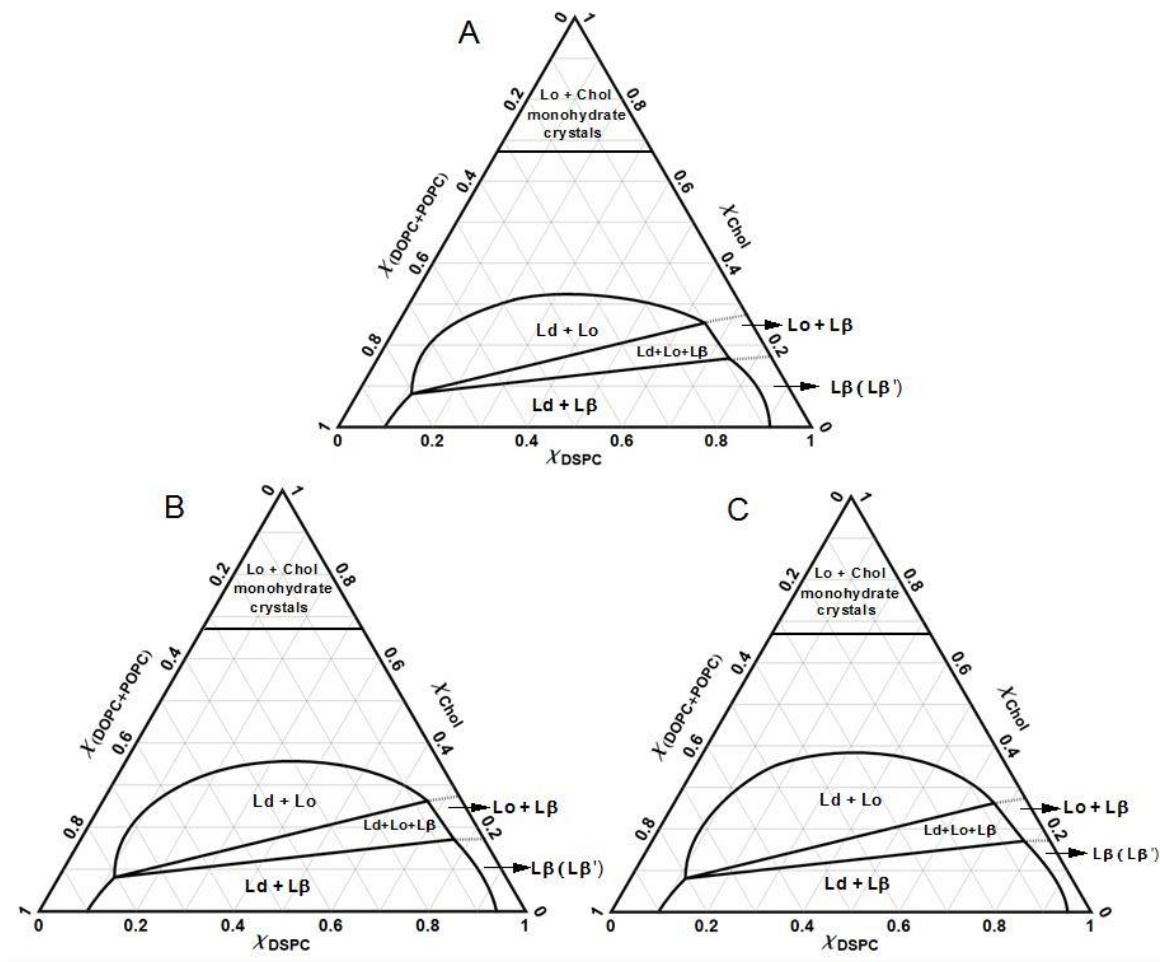


**Figure 3.13** Gibbs Triangles at intermediate  $\rho$  slices; (A)  $\rho = 0.20$ ; (B)  $\rho = 0.50$ ; and (C)  $\rho = 0.70$ . Phase boundaries are marked with solid black lines and dashed lines show estimated boundaries.

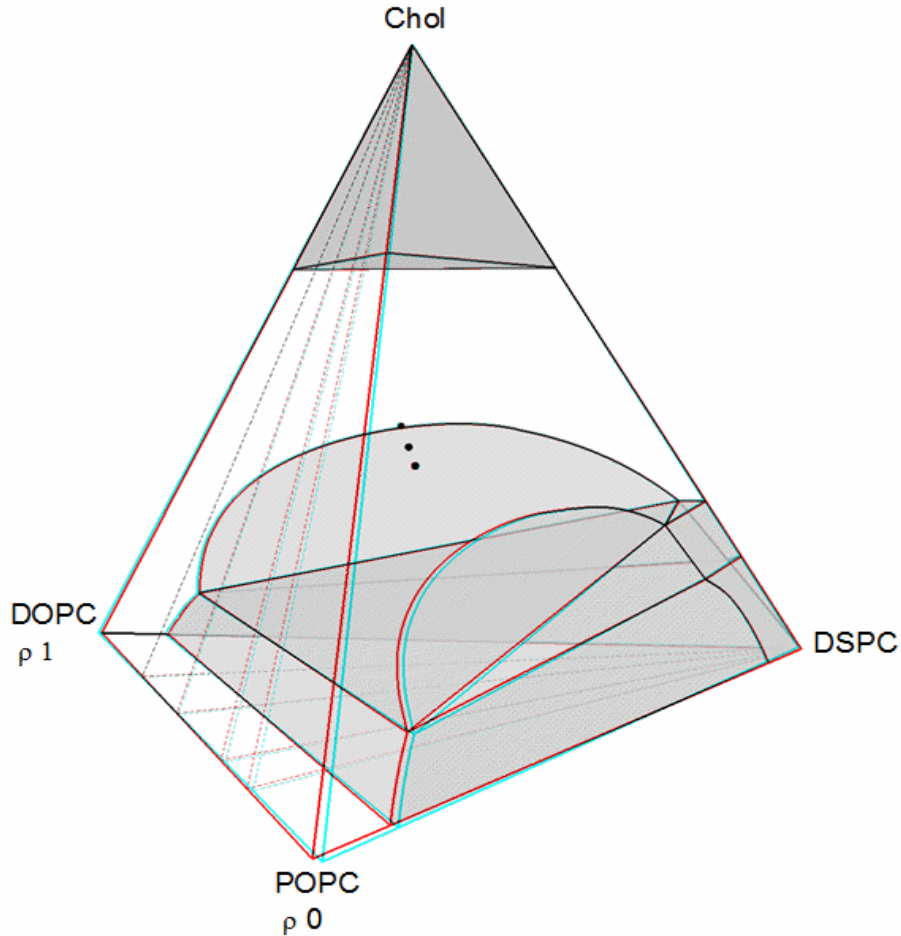


**Figure 3.14** Anaglyph image for DSPC/DOPC/POPC/chol phase diagram. Critical points for  $\rho = 1.0, 0.70,$  and  $0.50$  are shown as black dots.

The slopes of the bottom tieline in region 5 shows that the chemical potential of cholesterol is  $\sim 3$ -fold greater in the Ld phase than in the Lo phase, consistent with cholesterol interacting more favorably with saturated acyl chains than unsaturated ones. Yet, the Ld phase can accommodate cholesterol up to mole fraction 0.67 without a first-order phase change, instead gradually changing from Ld to Lo as cholesterol fraction increases [6]. In contrast, the L $\beta$  phase can accommodate cholesterol only up to  $\chi_{\text{CHOL}} \sim 0.17$ , above which the cholesterol-rich Lo phase separates in a first-order transition. We note that for plasma membranes having compositions

within region 5, as  $\chi_{\text{CHOL}}$  approaches typical values found in cells of  $\sim 0.3$ - $0.4$  [34], the  $\chi_{\text{CHOL}}$  in each phase becomes similar.

We have previously reported existence of an intermediate morphology of “modulated phases” within the Ld + Lo region in DSPC/DOPC/POPC/chol [23, 24]. Within the Ld + Lo coexistence region, the phase domain size changes from the nanometer scale at  $\rho = 0$  to the micron scale at  $\rho = 1$ . This size scale transition is accompanied by a visible morphology transition over a narrow range of compositions as DOPC is replaced with POPC, i.e. phase coexistence exhibits patterns, with one example illustrated by the GUV image in Fig. 6C. In the compositional region near  $\chi_{\text{DSPC}} = 0.39$ - $0.45$  and  $\chi_{\text{CHOL}} = 0.22$ - $0.25$ , the region of modulated phase domain morphology appears between  $\rho = 0.15$ - $0.30$  [23].

### **3.9.2.6 One phase varying continuously from Ld to Lo, region 6**

This region is shown as its entire phase volume in Fig. 3.9A, and the intersection of that volume with the  $\chi_{\text{DSPC}} = 0$  face of the tetrahedron in Fig. 8D. This is a region of continuous phase change, with no boundary marking a transition between Ld and Lo.

### **3.9.2.7 Coexisting cholesterol monohydrate crystals and a cholesterol-saturated Lo phase, region 7**

When cholesterol concentration exceeds  $\chi_{\text{CHOL}} \sim 0.67$ , cholesterol precipitates as crystals of the monohydrate. This phase boundary was determined previously [35], and results are shown here for completeness.

### 3.9.3 Some phase transitions might not be first-order

Phase boundaries determined by FRET are based on the principle that dyes partition between coexisting phases, a behavior that is characteristic of first-order phase transitions. In this study, we do not attempt to investigate the nature of the phase transitions, but rather focus on locating the phase boundaries. Clearly, some of the observed transitions cannot be first-order, such as the nano-to-macro domain size transition in region 5 (Ld + Lo). In this regard, it might also be the case that transitions along the DSPC/chol binary axis are not first-order [36], but we do not pursue that issue here.

### 3.9.4 Maximum cholesterol solubility in L $\beta$

We observe that the maximum solubility of cholesterol in the L $\beta$  phase is  $\chi_{\text{CHOL}} \sim 0.18$  when DOPC constitutes a small fraction ( $\sim 3$  mol%) of the L $\beta$  phase [4, 7]. In the L $\beta$  phase that has  $\chi_{\text{POPC}} \sim 0.12$  the maximum solubility of cholesterol is  $\chi_{\text{CHOL}} \sim 0.16$ . These observations might mean that the POPC-containing Lo phase forms somewhat more readily than the DOPC-containing Lo phase. Or, perhaps cholesterol within the L $\beta$  phase at  $\chi_{\text{POPC}} \sim 0.12$  has a higher chemical potential than has cholesterol in the L $\beta$  phase at  $\chi_{\text{DOPC}} \sim 0.03$ . We cannot answer this in the present study. As we have noted previously [6], this maximum cholesterol solubility of  $\chi_{\text{CHOL}} \sim 0.17$  in the L $\beta$  phase corresponds closely to each cholesterol being surrounded by one shell, i.e.  $\sim 6$  nearest-neighbor PCs. Apparently, more cholesterol than this cannot be accommodated in L $\beta$ . In contrast, Ld phases of either DOPC or POPC are stable up to  $\chi_{\text{CHOL}} \sim 0.67$ , where cholesterol monohydrate crystals precipitate.

### 3.9.5 Location of the region of modulated phase domains

One important aspect of this study is to place the observations of “nanodomains” within the framework of equilibrium phase behavior: The compositional volume of Ld + Lo phase coexistence extends from one face of the tetrahedron continuously through composition space to another face of the tetrahedron. This finding enables us to frame the origin of the nanodomains detected here at low concentration of DOPC as a “phase question”: Why should a liquid phase be more stable as small domains, rather than as one round domain having minimum perimeter and thus minimum unfavorable energy from line tension?

Although we do not attempt to answer this question directly here (but see Amazon et al. [37]), the present study provides a firm basis to pose this question in terms of equilibrium thermodynamics, rather than, for example, dynamic gain or loss of compositional regions as membrane turns over, or proximity to a critical point—bilayer behaviors that describe some systems well, but which are not universally applicable to all observations of small phase domains. For example, the 4-component phase diagram can be used to understand whether a region of nanodomains is indeed a 2-phase coexistence region, or instead is a structured 1-phase region. For the mixture DSPC/DOPC/chol, a 3-phase region of Ld + L $\beta$  + Lo exists just above the 2-phase Ld + L $\beta$  region. This 3-phase region was identified by fluorescence microscopy imaging that directly showed the shape and approximate area fractions of coexisting domains, and FRET data that clearly revealed the linearity of two sides of the phase coexistence triangle [4, 7]. In our current study of the 4-component mixture DSPC/DOPC/POPC/chol, we found this 3-phase region, directly observable by microscopy for DOPC-rich mixtures, to merge “seamlessly” with the smaller putative 3-phase region for DSPC/POPC/chol.

DSPC/POPC/chol mixtures with compositions above the 2-phase  $L_d + L_\beta$  region appear uniform by fluorescence microscopy imaging of GUVs [5]. The possibility has been raised that this region, which we identify as 3-phase, is actually a 1-phase microemulsion [38], or else a 1-phase region of critical fluctuations [27]. If so, then according to the phase boundaries that we report here for the 4-component mixture, a version of the Phase Rule sometimes termed the “Law of Adjoining Phases” [39] would be violated: As a phase boundary is crossed, one and only one phase can appear or disappear. If a 1-phase region were directly above the  $L_d + L_\beta$  coexistence region in POPC-rich mixtures, that 1-phase region would meet the 3-phase region  $L_d + L_\beta + L_o$  when the DOPC fraction becomes sufficiently great. At that boundary, the number of phases would change by 2, in violation of the Law of Adjoining Phases. With this reasoning,  $L_d + L_o$  nanodomains would seem to be well-described as coexisting phases.

### 3.10 Summary

1. All phase regions of the 3-component mixture DSPC/DOPC/chol can be determined unequivocally, with spectroscopic methods and GUV imaging in agreement as to phase boundaries and phase identity. In contrast, the phase diagram of the 3-component mixture DSPC/POPC/chol shows no visible  $L_d + L_o$  domains by optical imaging of GUVs. However, as DOPC is replaced by POPC, phase boundaries determined spectroscopically shift smoothly to new values, with no significant change in the nature of the phase behaviors. These observations are consistent with nanodomains of  $L_d + L_o$  in POPC-rich mixtures being phase domains.

2. With two appropriate 3-component phase diagrams in hand, constructing the 4-component phase diagram that joins them requires a relatively modest effort that can enable a clear definition of the phase region where “modulated phase behavior” occurs.

3. Some phase boundaries do not show up clearly when examined by conventional fluorescence spectroscopic methods, but can show up distinctly with a new “3-dye method” that makes use of a second FRET acceptor.

4. Precise measurement of phase boundaries confirms some near-stoichiometric cholesterol compositions  $\chi_{\text{CHOL}}$ :  $\sim 0.17$  is the maximum solubility of cholesterol in the  $L\beta$  phase, corresponding to one shell of PC around each cholesterol molecule;  $\sim 0.27$  is the minimum cholesterol concentration to form the  $L_o$  phase; 0.30 is the maximum cholesterol concentration for  $L_d + L_o$  coexistence in DSPC/POPC/chol; 0.40 is the maximum cholesterol concentration for  $L_d + L_o$  coexistence in DSPC/DOPC/chol; and 0.67 is the maximum solubility of cholesterol in an  $L_o$  phase, corresponding to the high energy of having more than 3 cholesterol molecules in contact [40].

## References

- [1] D. Lingwood, K. Simmons, Lipid rafts as a membrane-organizing principle, *Science*. 327, 5961 (2010) 46-50.
- [2] S.L. Veatch, K. Gawrisch, S.L. Keller, Closed-loop miscibility gap and quantitative tie-lines in ternary membranes containing diphytanoyl PC, *Biophys. J.* 90 (2006) 4428–4436.
- [3] S.L. Veatch, S.L. Keller, Seeing spots: complex phase behavior in simple mixtures, *Biochim. Biophys. Acta.* 1746 (2005) 172–185.
- [4] J. Zhao, J. Wu, F.A. Heberle, T.T. Mills, P. Klawitter, G. Huang, G. Costanza, G.W. Feigenson, Phase studies of model biomembranes: Complex behavior of DSPC/DOPC/Cholesterol, *Biochim. Biophys. Acta.* 1768 (2007) 2764-2776.
- [5] J. Zhao, J. Wu, H. Shao, F. Kong, N. Jain, G. Hunt, G.W. Feigenson, Phase studies of model biomembranes: macroscopic coexistence of  $L\alpha + L\beta$ , with light-induced coexistence of  $L\alpha + L_o$  phases, *Biochim. Biophys. Acta* 1768 (2007) 2777–2786.
- [6] G.W. Feigenson, J.T. Buboltz, Ternary phase diagram of dipalmitoyl-PC/dilauroyl-PC/cholesterol: nanoscopic domain formation driven by cholesterol, *Biophys. J.* 80 (2001) 2775–2788.
- [7] F.A. Heberle, J. Wu, S.L. Goh, R.S. Petruzielo, G.W. Feigenson, Comparison of three ternary lipid bilayer mixtures: FRET and ESR reveal nanodomains, *Biophys. J.* 99 (2010) 3309-3318.
- [8] R.S. Petruzielo, F.A. Heberle, P. Drazba, J. Katsaras, G.W. Feigenson, Phase Behavior and Domain Size in Sphingomyelin-Containing Lipid Bilayers, *Biochim. Biophys. Acta.*, 1828 (2013) 1302-1313.
- [9] F.A. Heberle, R.S. Petruzielo, J. Pan, P. Drazba, N. Kučerka, R.F. Standaert, G.W. Feigenson, J. Katsaras, Bilayer thickness mismatch controls domain size in model membranes, *J. Am. Chem. Soc.* 135(18) (2013) 6853-9.
- [10] A. Pokorny, L.E. Yandek, A.L. Elegbede, A. Hinderliter, P.F. Almeida, Temperature and composition dependence of the interaction of d-lysine with ternary mixtures of sphingomyelin/cholesterol/POPC, *Biophys. J.* 91 (2006) 2184–2197.
- [11] R.F.M. de Almeida, A. Fedorov, M. Prieto, Sphingomyelin/ Phosphatidylcholine/ cholesterol phase diagram: boundaries and composition of lipid rafts, *Biophys. J.* 85 (2003) 2406–2416.

- [12] J.R. Silvius, Fluorescence energy transfer reveals microdomain formation at physiological temperatures in lipid mixtures modeling the outer leaflet of the plasma membrane, *Biophys. J.* 85 (2003) 1034–1045.
- [13] J.F. Hancock, Lipid rafts: contentious only from simplistic standpoints, *Nat. Rev. Mol. Cell Biol.* 7 (2006) 456-462.
- [14] P.F.F. Almeida, A. Pokorny, A. Hinderliter, Thermodynamics of membrane domains, *Biochim. Biophys. Acta.*1720 (2005) 1-13.
- [15] E.L. Elson, E. Fried, J.E. Dolbrow, G.M. Genin, Phase separation in biological membranes: integration of theory and experiment, *Ann. Rev. Biophys.* 39 (2010) 207-226.
- [16] N. Vyas, D. Goswami, A. Manonmani, P. Sharma, H.A. Ranganath, K. VijayRaghavan, L.S. Shashidhara, R. Sowdhamini, S. Mayor, Nanoscale organization of hedgehog is essential for long-range signaling, *Cell.* 133 (2008) 1214–1227.
- [17] D. Meder, M.J. Moreno, P. Verkade, W.L. Vaz, K. Simons, Phase coexistence and connectivity in the apical membrane of polarized epithelial cells, *PNAS.* 103 (2006) 329-334.
- [18] M. Ge, A. Gidwani, H. A. Brown, D. Holowka, B. Baird, J.H. Freed, Ordered and disordered phases coexist in plasma membrane vesicles of RBL-2H3 Mast Cells. An ESR study, *Biophys. J.* 85 (2003) 1278–1288.
- [19] C. Eggeling, C. Ringemann, R. Medda, G. Schwarzmann, K. Sandhoff, S. Polyakova, V.N. Belov, B. Hein, C von Middendorff, A. Schönle, S. W. Hell, Direct observation of the nanoscale dynamics of membrane lipids in a living cell, *Nature.* 457 (2009) 1159-1162.
- [20] S.J. Sahl, M. Leutenegger, M. Hilbert, S.W. Hell, C. Eggeling, Fast molecular tracking maps nanoscale dynamics of plasma membrane lipids, *PNAS.* 107, 15 (2010) 6829–6834.
- [21] T.S. van Zantena, J. Gómezb, C. Manzoa, A. Cambic, J. Bucetad, R. Reigadab, M.F. Garcia-Parajoa, Direct mapping of nanoscale compositional connectivity on intact cell membranes, *PNAS.* 107, 35 (2010) 15437–15442.
- [22] F.A. Heberle, G.W. Feigenson, Phase Separation in Lipid Membranes, *Cold Spring Harb. Perspect. Biol.* (2011) doi:10.1101/cshperspect.a004630.
- [23] T.M. Konyakhina, S.L. Goh, J. Amazon, F.A. Heberle, J. Wu, G.W. Feigenson, Control of a nanoscopic-to-macroscopic transition: modulated phases in 4-Component DSPC/DOPC/POPC/chol Giant Unilamellar Vesicles, *Biophys. J. Letters.* 101, 2 (2011) L8-L10.
- [24] S.L. Goh, J. Amazon, G.W. Feigenson. Towards a better raft model: Modulated phases in the 4-component bilayer, *DSPC/DOPC/POPC/CHOL*, *Biophys. J.*, 104 (2013) 853-862.

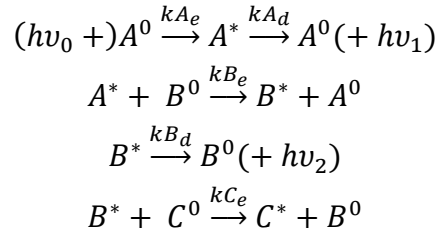
- [25] C. Esposito, A. Tian, S. Melamed, C. Johnson, S.Y. Tee, T. Baumgart, Flicker spectroscopy of thermal bilayer domain boundary fluctuations, *Biophys. J.* 93 (2007) 3169–3181.
- [26] S.L. Veatch, P. Cicuta, P. Sengupta, A. Honerkamp-Smith, D. Holowka, B. Baird, Critical fluctuations in plasma membrane vesicles, *ACS Chem. Biol.* 3 (2008) 287–293.
- [27] A.R. Honerkamp-Smith, S.L. Veatch, S.L. Keller. An introduction to critical points for biophysicists; observations in lipid membranes, *Biochim. Biophys. Acta.* 1788, 1 (2009) 53-63.
- [28] J.T. Buboltz, G.W. Feigenson, A novel strategy for the preparation of liposomes: rapid solvent exchange, *Biochim. Biophys. Acta.* 1417 (1999) 232–245.
- [29] M.I. Angelova, S. Soleau, P. Meleard, J.F. Faucon, P. Bothorel, Preparation of giant vesicles by external AC electric fields. Kinetics and applications, *Progr. Colloid. Polym. Sci.* 89 (1992) 127–131.
- [30] N.F. Morales-Pennington, J. Wu, E.R. Farkas, S.L. Goh, T.M. Konyakhina, J.Y. Zheng, W.W. Webb, G.W. Feigenson, GUV preparation and imaging: minimizing artifacts, *Biochim. Biophys. Acta.* 1798, 7 (2010) 1324-1332.
- [31] J.T. Buboltz, Steady-state probe-partitioning fluorescence resonance energy transfer: a simple and robust tool for the study of membrane phase behavior, *Phys. Rev. E.* 76 (2007) 021903.
- [32] P. Ceppi, S. Colombo, M. Francolini, F. Raimondo, N. Borgese, M. Masserini, Two tail-anchored protein variants, differing in transmembrane domain length and intracellular sorting, interact differently with lipids, *PNAS.* 102, 45 (2005) 16269-16274.
- [33] J.S. Marsh, *Principles of Phase Diagrams*, McGraw-Hill, New York, 1935, pp. 122–170.
- [34] The AOCS Lipid Library, <http://lipidlibrary.aocs.org/>, the joint Editors-in-Chief J. L. Harwood, R. J. Weselake, technical Editor W. W. Christie. Last updated 12/21/2012.
- [35] J.Huang, J.T. Buboltz, G.W. Feigenson, Maximum solubility of cholesterol in phosphatidylcholine and phosphatidylethanolamine bilayers, *Biochim. Biophys. Acta.* 1417 (1999) 89–100.
- [36] T.T. Mills, J. Huang, G.W. Feigenson, J.F. Nagle, Effects of cholesterol and unsaturated DOPC lipid on chain packing of saturated gel-phase DPPC bilayers, *Gen. Physiol. Biophys.* 28, 2 (2009) 126-39.

- [37] J.J Amazon, S.L.Goh, G.W. Feigenson, Competition between line tension and curvature stabilizes modulated phase patterns on the surface of giant unilamellar vesicles: A simulation study. *Phys. Rev. E* 87 (2013) 022708.
- [38] M. Schick, Membrane heterogeneity: manifestation of a curvature-induced microemulsion. *Phys. Rev. E* 85 (2012) 031902.
- [39] L.S. Palatnik, A.I. Landau, A.I, Phase equilibria in multicomponent systems, Ed. J. Jaffe, Holt, Rinehart & Winston, New York, 1964.
- [40] J. Huang, G.W. Feigenson, A microscopic interaction model of maximum solubility of cholesterol in lipid bilayers, *Biophys. J.* 76, 4 (1999) 2142-57.
- [41] J.T. Buboltz, C. Bwalya, S. Reyes, D. Kamburov, Stern-Volmer modeling of steady-state Förster energy transfer between dilute, freely diffusing membrane-bound fluorophores, *J. Chem. Phys.* 127 (2007) 215101.

## Supplemental Materials

### 3.S.1 Derivation of 3-dye FRET<sup>3</sup>

The bilayer contains three different fluorescent dyes, with maximum excitation wavelengths  $A < B < C$ . We seek an expression for the fluorescence intensity of dye B upon direct excitation of dye A. The derivation follows [41]. We assume an illumination wavelength  $\lambda_0$  (with frequency  $\nu_0$ ) that selectively excites A. Furthermore, we assume that the emission spectrum of A overlaps with the excitation spectrum of B but not that of C (i.e., A can transfer energy only to B), and that B transfers energy to C. Ignoring dye self-quenching, we use the following kinetic model for the relevant photophysical processes:



where the superscripts \* and 0 indicate excited and ground states;  $k_{Ae}$  is the rate constant for direct excitation of A;  $k_{Be}$  and  $k_{Ce}$  are rate constants for spontaneous energy transfer to acceptor B (from donor A) and acceptor C (from donor B); and  $k_{Ad}$  and  $k_{Bd}$  are rate constants for de-excitation of A and B by modes other than energy transfer (including fluorescence at frequencies  $\nu_1$  and  $\nu_2$ ).

---

<sup>3</sup> Derivations by Fred Heberle, reproduced from Supplemental materials for Konyakhina TM, Wu J, Mastroianni JD, Heberle FA, Feigenson GW. 2013. Phase diagram of a 4-component lipid mixture: DSPC/DOPC/POPC/chol. *Biochim Biophys Acta*. 1828(9):2204-14.

The rate equation for the excited state concentration of A is:

$$\frac{d\chi_{A^*}}{dt} = k_{Ae}\chi_{A^0}[h\nu_0] - k_{Ad}\chi_{A^*} - k_{Be}\chi_{A^*}\chi_{B^0} \quad (A.1)$$

Assuming low illumination intensity, only a small fraction of fluorophores are in the excited state (e.g.,  $\chi_{A^*} \ll \chi_A$ ), which enables the substitutions  $\chi_A \approx \chi_{A^0}$ ,  $\chi_B \approx \chi_{B^0}$ ,  $\chi_C \approx \chi_{C^0}$ . The steady-state approximation leads to an equation for the excited state concentration of A:

$$\chi_{A^*} = \frac{(k'_{Ae}/k_{Ad})\chi_A}{1 + (k_{Be}/k_{Ad})\chi_B} \quad (A.2)$$

with the additional substitution  $k_{Ae}[h\nu_0] = k'_{Ae}$ . Applying the same approach to B yields the rate equation:

$$\frac{d\chi_{B^*}}{dt} = k_{Be}\chi_B\chi_{A^*} - k_{Bd}\chi_{B^*} - k_{Ce}\chi_{B^*}\chi_C \quad (A.3)$$

A steady-state approximation combines Equations A.2 and A.3, which upon rearranging yields an equation for the excited state concentration of B:

$$F_B^{Aex} \propto \chi_{B^*} = \frac{(k'_{Ae}/k_{Bd})(k_{Be}/k_{Ad})\chi_A\chi_B}{[1 + (k_{Be}/k_{Ad})\chi_B][1 + (k_{Ce}/k_{Bd})\chi_C]} = \frac{C_0 C_1 \chi_A \chi_B}{[1 + C_1 \chi_B][1 + C_2 \chi_C]} \quad (A.4)$$

where we have defined a FRET metric  $F_B^{Aex}$  (sensitized B emission) that is proportional to  $\chi_{B^*}$ . The quenching constants  $C_1$  and  $C_2$  describe energy transfer between dye pairs  $A \rightarrow B$  and  $B \rightarrow C$ , respectively, and can be related to their respective Förster distances [39]:

$$C_i \approx \frac{\varepsilon R_{0,i}^2}{A} \quad (\text{A.5})$$

where  $A$  is the molecular area of the membrane and  $\varepsilon = \pi\Gamma(2/3) \approx 4.2541$ .

Equation A.4 shows the dependence of dye B sensitized emission on the concentrations of the three dye species. In a phase-separated bilayer, non-uniform partitioning modulates the dye concentrations within each phase in a manner that depends on the relative amounts of the phases present. For a two-phase system with a total dye molar concentration  $\chi_P^0$  and a molar partition coefficient  $K_P$ , the concentration of dye in each phase is:

$$\chi_P^1 = \frac{\chi_P^0}{1 - S_2 + S_2 K_P} \quad (\text{A.6})$$

$$\chi_P^2 = \frac{K_P \chi_P^0}{1 - S_2 + S_2 K_P} \quad (\text{A.7})$$

where superscripts refer to the phase (1 or 2),  $S_2$  is the mole fraction of phase 2, and  $K_P > 1$  indicates preference for phase 2. The observed fluorescence of dye B is a mole fraction-weighted sum of its fluorescence in each phase:

$$F_B^{Aex} = (1 - S_2)F_{B,1}^{Aex} + S_2 F_{B,2}^{Aex} \quad (\text{A.8})$$

Using the definition  $K'_P \equiv 1 - S_2 + S_2 K_P$ , combining equations A.4, A.6–8 and rearranging yields:

$$F_B^{Aex} = \frac{\alpha \chi_A^0 \chi_B^0 K'_C}{K'_A} \left( \frac{(1 - S_2) C_1^1}{[K'_B + C_1^1 \chi_B^0][K'_C + C_2^1 \chi_C^0]} + \frac{S_2 C_0^0 C_1^2 K_A K_B}{[K'_B + C_1^2 \chi_B^0 K_B][K'_C + C_2^2 \chi_C^0 K_C]} \right) \quad (\text{A.9})$$

where  $\alpha$  is a constant of proportionality that depends on experimental details (instrumentation and sample concentration), and  $C_0^0 \equiv C_0^2/C_0^1$ .

### 3.S2. 3-dye FRET to determine phase boundaries in lipid mixtures

FRET between dilute fluorescent lipid dyes is in principle a powerful tool for determining phase boundaries in lipid mixtures. The simplest form of the experiment is shown schematically in Fig. 3.S6:

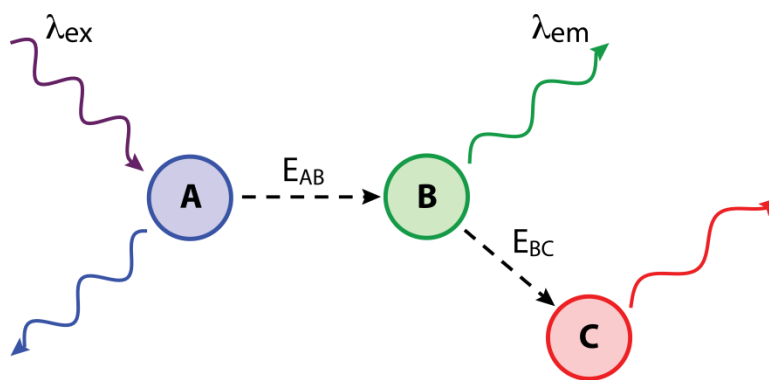


**Figure 3.S6** Schematic representation of the three dye FRET experiment. The bilayer contains three dyes with excitation wavelengths  $A < B < C$ . Dyes A and B form a FRET pair with efficiency  $E_{AB}$ , and B and C form a FRET pair with efficiency  $E_{BC}$ . Fluorescence emission of B is measured using an illumination wavelength that selectively excites dye A. Dye C is added to quench B fluorescence.

The sample is illuminated with monochromatic light of wavelength  $\lambda_{ex}$  to generate a small population of excited A fluorophores, which can either emit a lower energy photon, or donate energy *via* the nonradiative Förster mechanism to an acceptor fluorophore B. The efficiency of

energy transfer  $E_{AB}$  can be monitored by observing either A or B fluorescence. Sensitized acceptor emission, whereby the illumination wavelength  $\lambda_{ex}$  is chosen to selectively excite the donor A with emission collected at wavelength  $\lambda_{em}$  specific to the acceptor B, is a convenient FRET metric that provides good signal-to-noise even at dilute dye concentrations. In the following discussion, we refer to sensitized B emission with the symbol  $F_B^{Aex}$ , with the superscript serving as a reminder that the illumination wavelength is selective for A. Fig. 3.S6 also shows a third fluorophore C, which selectively accepts energy from B with efficiency  $E_{BC}$ . The presence of C reduces  $F_B^{Aex}$  in direct proportion to  $E_{BC}$ . We now describe how the addition of the quencher C can greatly facilitate the determination of phase boundaries in lipid bilayer mixtures.

FRET efficiency between freely-diffusing dyes depends on acceptor concentration.<sup>1,2</sup> In a phase-separated bilayer, non-uniform partitioning of dilute dyes between phase domains strongly modulates local acceptor concentrations, resulting in enhanced or reduced FRET efficiency (for like or unlike donor and acceptor partitioning, respectively).<sup>3</sup> In this case,  $F_B^{Aex}$  depends on dye partition coefficients and the relative amounts of the coexisting phases, as shown by Eq. 3.A.9 of the main text. Figure 3.S7 (solid black curve) plots Eq. 3.A.9 for the case of strong partitioning of A and B dyes, in the absence of quencher C (*i.e.*,  $\chi_C^0 = 0$ ):

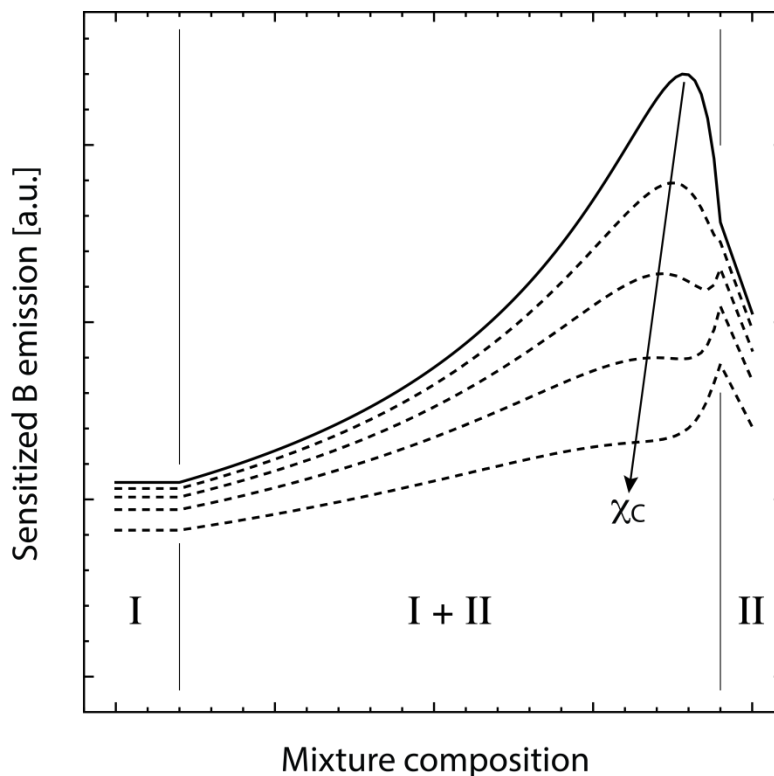


**Figure 3.S7** Reduction of sensitized dye B emission by addition of a quencher C. In the absence of C,  $F_B^{Aex}$  exhibits a characteristic “rise and fall” shape of enhanced FRET efficiency (solid black curve) within the I+II coexistence region, due to strong partitioning of both A and B into phase I. Increasing the concentration of C (dashed black curves) reduces  $F_B^{Aex}$  non-uniformly across the I+II region, with dramatic effects occurring near the phase II boundary. Crucially, at high concentrations of C (lower three curves), *the slope near the phase II boundary is reversed*, facilitating detection of the boundary.

The compositional trajectory begins in a single phase region I (e.g., Ld), follows a tieline of phase coexistence (where  $F_B^{Aex}$  is described by Eq. 3.A.9), and ends in a single phase region II (e.g., Lo). Dyes that prefer phase I exhibit a convex increase in concentration (Eqs. 3.A.6 and 3.A.7) as phase II replaces phase I along the tieline (left-to-right movement in Fig. 3.S7), resulting in greater transfer efficiency and enhanced  $F_B^{Aex}$ . The increase in  $F_B^{Aex}$  begins gradually at the phase I boundary and accelerates near the phase II boundary, with  $F_B^{Aex}$  finally falling as the fraction of phase I decreases to zero. Along the tieline, the combined effects of (a) a convex

increase in dye concentrations within phase I and (b) a linear decrease in the fraction of phase I, result in a peak in  $F_B^{Aex}$  near the phase II boundary. The peak position and intensity are further influenced by differences in the intrinsic fluorescence of dye B in the two phases: Fig. S7 demonstrates the case where B has greater intrinsic fluorescence in phase II, mimicking the observed behavior of BoDIPY-PC in the experiments presented in the main text.

As mentioned previously, the addition of dye C reduces B fluorescence in direct proportion to the  $B \rightarrow C$  transfer efficiency as shown by Eq. A.4, here modified to explicitly demonstrate the dependence on  $E_{BC}$ :

$$F_B^{Aex}(\chi_C) = \frac{C_0 C_1 \chi_A \chi_B}{[1 + C_1 \chi_B][1 + C_2 \chi_C]} = (F_B^{Aex}|_{\chi_C=0})[1 - E_{BC}(\chi_C)]$$

where

$$E_{BC}(\chi_C) = 1 - (1 + C_2 \chi_C)^{-1}$$

When dye C also prefers phase I,  $E_{BC}$  and  $E_{AB}$  have similar composition dependence, and the reduction in  $F_B^{Aex}$  caused by C is therefore non-uniform across the tieline. The effect of increasing dye C concentration ( $\chi_C$ ) is shown by the dashed curves in Fig. S7. Dye B fluorescence is strongly quenched near the phase II boundary, where the dyes are highly concentrated in the small fraction of phase I. Increasing  $\chi_C$  shifts the  $F_B^{Aex}$  peak to the left and reduces its intensity. At sufficiently high  $\chi_C$ , the slope near the phase II boundary reverses sign (lower three curves). To summarize, the behavior of Eq. 3.A.9 suggests that the slope of the  $F_B^{Aex}$  curve can be dramatically altered near the phase boundaries by manipulating the concentration of C.

Within a single phase region, the composition dependence of  $F_B^{Aex}$  is influenced by nonideal mixing of the dyes, and to a lesser extent by changes in dye photophysical properties (quantum yield) and the physical properties of the phase itself (molecular area). For Ld-preferring

dyes, mixing is nearly ideal within the Ld phase, and  $F_B^{Aex}$  typically has little composition dependence. Markedly different behavior is often observed for Ld-preferring dyes in single phase Lo compositions, where steep changes occur with relatively small changes in mixture composition. In Fig. 3.S7,  $F_B^{Aex}$  within the single phase regions I and II was modeled with linear variation consistent with experimental data (see Fig. 3.4 of the main text).

Figure S8 shows simulated noisy data corresponding to the  $F_B^{Aex}$  trajectories of Fig. 3.S7, with trajectories offset for clarity:

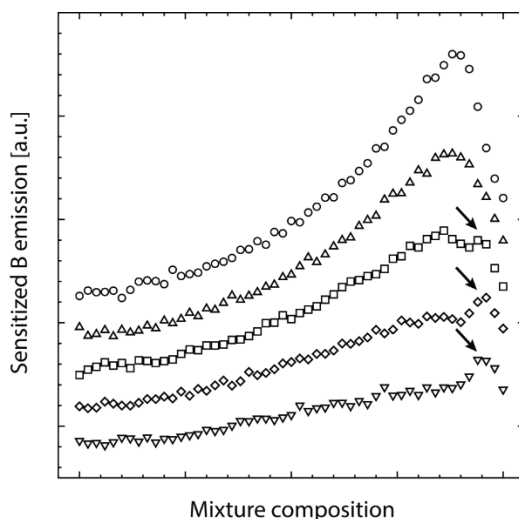


**Figure 3.S8** Simulated  $F_B^{Aex}$  trajectory data corresponding to model curves in Fig. 3.S7. Curves were sampled at 2 mol% compositional resolution, and Gaussian noise was added. Arrows mark the position of the phase II boundary determined by visual inspection of the trajectories (offset for clarity).

In the absence of C (open circles), the small change in slope at the phase II boundary is obscured by limited compositional resolution and experimental noise. Addition of C reverses the slope of  $F_B^{Aex}$  within the coexistence region near the phase II boundary, allowing for a clear determination of the boundary by visual inspection (black arrows).

## References

- [1] P.K. Wolber, B.S. Hudson, *Biophys. J.* 28 (1979) 197.
- [2] B. Kwok-Keung, L. Stryer, *Biochemistry.* 17 (1978) 5241.
- [3] J.T. Buboltz, *Phys. Rev. E.* 76 (2007) 021903.

## CHAPTER 4

### Phase Diagram of a Polyunsaturated Lipid Mixture: BSM/SDPC/Chol

#### 4.1 Abstract

Phospholipids having a polyunsaturated acyl chain are abundant in biological membranes, but their behavior in lipid mixtures is difficult to study. Here we elucidate the nature of such mixtures with this report of the first ternary phase diagram containing the polyunsaturated lipid SDPC in mixtures of BSM/SDPC/Chol (brain sphingomyelin/1-stearoyl-2-docosahexaenoyl-sn-glycero-3-phosphocholine/ cholesterol). These mixtures show macroscopic Ld + Lo phase separation, with phase boundaries determined by FRET and by fluorescence microscopy imaging of giant unilamellar vesicles (GUVs). Surprisingly, SDPC mixes with BSM/Chol similarly to how DOPC and POPC mix with BSM/Chol. In addition, modulated phases are observed within the Ld + Lo liquid-liquid immiscibility region upon addition of fourth component POPC. We find mixtures of BSM/SDPC/POPC/Chol to exhibit nanoscopic Ld + Lo domains over a very large volume of composition space.

#### 4.2 Introduction

Eukaryotic plasma membranes comprise a complex chemical mixture of proteins and lipids [1]. These membranes are both protective barriers, separating life from death for the cell, and participate in a variety of cellular processes that involve membranes, including immune signaling, protein sorting, endocytosis, and virus entry and exit.

For phase diagrams determined at equilibrium, the thermodynamics of mixing provides a powerful framework for establishing rules for understanding and interpreting the phase behavior.

These well-defined phase rules describe the conditions under which the different phases (e.g. solid gel  $L\beta$ , liquid-ordered  $L_o$ , and liquid-disordered  $L_d$ ) can coexist at equilibrium. Ternary lipid bilayer mixtures containing cholesterol and exhibiting phase separation can be grouped into two categories [2]: Type II diagrams exhibit macroscopic regions of  $L_d + L_o$  and  $L_d + L\beta + L_o$  immiscibility, with domains resolved under the light microscope. Type I mixtures have the same phase coexistence regions, but with nanoscopic domains [3]. These systems have liquid-liquid immiscibility regions that might resemble phase separation in real cells [4-9] where domains have been guessed to be in the nanoscopic range between 20-200 nm [8, 9]. Nanoscopic domains are detected *in vivo* in plasma membranes by methods that are sensitive to small length scales, such as FRET [10, 11], FRAP [12], electron spin resonance (ESR) [13], and stimulated emission depletion (STED) far-field fluorescence nanoscopy [14]. In particular, nanodomains that have  $L_d$  and  $L_o$  characteristics have been detected with FRET [10] and ESR [12] in live cells. Thus, lipid ‘raft’ domains, enriched in cholesterol and sphingolipids, together with non-raft domains, seem to be significant types of lateral heterogeneities in biological membranes [12, 15-20].

To date, a number of lipid mixture phase diagrams have been solved [21-29], but none of these lipid mixtures have included polyunsaturated lipids, in large part because of the experimental difficulties in working with polyunsaturated fatty acids, PUFAs. In this study we solve the phase diagram of a ternary mixture containing a PUFA lipid together with two other biologically abundant species, BSM/SDPC/Chol. We also discuss overcoming experimental difficulties in working with PUFAs. The predominant high- $T_m$  components of mammalian PM are sphingomyelins (SM), and we chose to study the sphingomyelin derived from porcine brain, BSM. Cholesterol, present at 35-45 mol% in mammalian plasma membranes [30], is an indispensable component of any plasma membrane model mixture. SDPC contains a stearyl chain and the

omega-3 polyunsaturated fatty acyl chain DHA, with 22-carbons and 6 double bonds [31, 32].

In the inner leaflet of animal cell plasma membranes PUFAs comprise ~50% of sn-2 fatty acyl chains [<http://lipidlibrary.aocs.org/Lipids/complex.html> [19]]. In retinal rod outer segment disk membranes DHA comprises up to 50% of the total lipid, with this high percentage required for optimal Rhodopsin function [33, 34]. DHA is also found at high concentrations in certain other membranes, including synaptosomes [35] and sperm [36]. The importance of DHA and PUFAs for human health has been studied [37-39], as well as spectroscopic studies [40-42], and studies of PUFA effects on membrane properties [43-54]. PUFAs seem to have a weaker interaction with cholesterol compared with saturated or monounsaturated acyl chains [55]. A relatively low solubility of cholesterol in PUFA-containing membranes was measured using both X-ray diffraction and solid-state  $^2\text{H}$  NMR [56-64]. It has been proposed [57, 59] that DHA could be directly involved in inducing lateral phase separations into DHA-rich/cholesterol-poor and DHA-poor/cholesterol-rich lipid domains.

Despite the clear importance of DHA-containing lipids such as SDPC, SDPE, PDPC, and PDPE, only a very limited number of PUFA-containing compositions have been examined. The vast majority of studies conducted on DHA-containing lipids have focused on only a few sample compositions, with one common ratio being 1/1/1 = DHA-containing lipid/SM/Chol, with the DHA-containing lipid being SDPC, SDPE, PDPC or PDPE [52, 53, 65]. Mixing behavior over all possible compositions of these three-component mixtures, especially the regions of immiscibility, can be described by use of a triangular phase diagram.

Since 1999, GUVs have proven to be useful tools for the visualization of bilayer phases and have been widely used to study phase behavior in model membranes [21-25, 66-68]. However, GUVs have their own characteristic limitations. One such limitation is the relatively low

compositional resolution of ~5% that can be achieved with this method (but see [69] for higher compositional precision). Also, GUVs are not useful for finding phase boundaries of mixtures with coexisting domains that are much smaller than the wavelength of light, due to the limits of optical resolution. Other GUV limitations are the potential for electrolysis-induced artifacts associated with the electroswelling method, and oxygen- and free radical-induced artifacts [67, 68]. These particular problems can be mitigated by forming GUVs by use of “gentle hydration”. Cuvette-based spectroscopic methods such as FRET can be used to construct a phase diagram with few artifacts and with a higher compositional resolution of ~2%, but a large number of samples are required. FRET experiments are cuvette-based, enabling sample preparation by use of rapid solvent exchange (RSE), which minimizes the lipid demixing, especially of cholesterol that can occur when lipid mixtures are dried [70]. RSE also has the benefit of convenient maintenance of an inert atmosphere at all stages of sample preparation, minimizing oxygen-induced artifacts that are a significant problem in mixtures containing PUFA lipids.

Biological membrane phase behavior can be modeled well by mixtures of four lipids, which enables study of Ld + Lo domain size from a few nanometers to many microns that is controlled by composition. Why do we care about the switch of domain size from nano to macro? The tens of nanometer scale seems to describe the phase-separated domains in animal cell plasma membranes better than does the micron scale [71-73]. Silvius [74] proposed the presence of nanodomains in a lipid bilayer with compositions mimicking the outer leaflet bilayer. Lipids such as SOPC or POPC, having one saturated sn-1 chain and one monounsaturated sn-2 chain, naturally occur as the most abundant phospholipid species in animal cell membranes. Optical microscopy studies on such lipids in ternary mixtures with cholesterol and a high-melting lipid show uniform membranes [21, 75], yet other methods indicate the presence of lateral heterogeneity [27, 75-77]

invisible to optical microscopy imaging. We have previously reported the presence of intermediate states that have modulated phase morphology in the 4-component mixture DSPC/DOPC/POPC/Chol [78, 79, 28]. Modulated phase morphology occurs when two liquid phases coexist, if the line tension that drives the minimization of domain perimeter is opposed by a long-range interaction such as bending energy of a curved membrane that acts to break up domains [79, 80].

We report that the phase diagram of BSM/SDPC/Chol at constant temperature is remarkably similar to phase diagrams having DOPC or POPC instead of SDPC. We also report the existence of modulated phases upon the addition of POPC as a fourth component to BSM/SDPC/Chol, finding that with SDPC-containing mixtures, only a small fraction of POPC results in nanodomains, compared to the much larger fractions of POPC required for nanodomains in DOPC-containing mixtures. Together, these findings indicate that a lipid with a single PUFA chain can give rise to macroscopic Ld + Lo domains, but that a modest fraction of POPC in the mixtures yields nanodomains.

## **4.3 Materials and Methods**

### **4.3.1 Materials**

Phospholipids were purchased from Avanti Polar Lipids (Alabaster, AL), and cholesterol from Nu Chek Prep (Elysian, MN). Fluorescent dyes C12:0 DiI and BoDIPY-PC were from Invitrogen (Carlsbad, CA), DHE was from Sigma-Aldrich (St. Louis, MO). Lipid stock solutions were prepared in HPLC grade chloroform with concentration determined to < 1% by inorganic phosphate assay. BSM stocks included 0.5% methanol by volume to prevent precipitation during

humid weather. Phospholipid purity was verified to be > 99% by thin-layer chromatography (TLC) of ~ 20 micrograms of lipid on washed and activated Adsorbosil TLC plates (Alltech, Deerfield, IL), developed in solvent system chloroform/methanol/water = 65/25/4. SDPC stocks were frequently checked for purity using a spectroscopic absorbance method (see section 2.2 for more details). Cholesterol stocks were prepared analytically and purity checked with TLC in petroleum ether/diethyl ether/chloroform = 7/3/3. Probe extinction coefficients were obtained from lot certificates of analysis: 91800 M<sup>-1</sup>cm<sup>-1</sup> at 504 nm for BoDIPY-PC and 12900 M<sup>-1</sup>cm<sup>-1</sup> at 324 nm for DHE. Fluorescent dyes were checked for purity with the following solvent systems: BoDIPY-PC in chloroform/methanol/water = 65/25/4; C12:0 DiI in chloroform/methanol = 10/1. Concentrations of fluorescent dyes were measured by absorption spectroscopy using an HP 8452A spectrophotometer (Hewlett-Packard, Palo Alto, CA).

#### **4.3.2 Control for PUFA lipid breakdown**

PUFA breakdown is readily initiated by free-radical formation and subsequent propagation of a chain-reaction that proceeds auto-catalytically [81-84]. Therefore, it is crucial to eliminate or greatly minimize factors such as oxygen, multivalent cations especially iron, and light, that initiate or propagate this breakdown pathway [81-85]. Our experimental protocol produces less than 2% breakdown after all experimental steps, as measured by TLC and a UV spectroscopic assay for lipid breakdown. All physical handling of lipids is performed in an inert atmosphere under low light conditions. All solvents and buffers that come into contact with SDPC were deoxygenated by bubbling with inert gas to displace dissolved oxygen. A low oxygen atmosphere was achieved by handling SDPC inside a glove box with O<sub>2</sub> levels reduced from the atmospheric reading of

18.2% down to the glove box reading of ~0.02%, as measured by an oxygen sensor (OXY-sen oxygen monitor, Alpha Omega Instruments). Minimization of iron ions was achieved by the addition of 50  $\mu\text{m}$  DTPA, efficient in chelating iron [85], to all aqueous solutions in contact with SDPC. SDPC was purchased from Avanti packaged into small aliquots of 2.5 mg per vial, enabling use of a fresh vial for every week of experimental work. Purity of lipid stocks was checked by TLC and UV spectroscopic assay for lipid breakdown. Samples for UV spectroscopic assay were prepared by extracting aqueous lipid suspensions from GUVs using Bligh-Dyer conditions [86]. A mixture of cyclohexane/EtOH = 10/1 was used to redissolve the dry film. Lipids without conjugated double bonds have a single strong absorption peak at ~200 nm. Breakdown-induced conjugation yields a strong peak at 235 nm. The ratio of peak heights at 235/200 was used to monitor breakdown.

#### **4.3.2.1 Control for photooxidation and light-induced phase separation**

Oxidation and photooxidation, as well as free radical-induced polymerization, are troublesome phenomena to researchers working with model lipid systems. The final stage of light-induced oxidation and free radical-induced polymerization can look identical to real macroscopic Ld + Lo phase separation and can mislead phase determination by fluorescent microscopy [67, 68, 87]. Light-induced artifacts can happen even in phase-separated mixtures that are inherently nanoscopic. DSPC/POPC/Chol and BSM/POPC/Chol mixtures lack macroscopic Ld + Lo phase separation, yet both mixtures undergo light-induced, artifactual, macroscopic domain separation [67, 68]. Light-induced phase separation happens during illumination with an optical microscope, and is strongly dependent on concentration of dye [68] or photosensitizer [88] and illumination

intensity and time. The kinetics of light-induced domain formation vary from system to system, but unlike real macroscopic phase separation, light-induced artifacts are observed to transition through stages of ripening, growing, and final fusing and rounding to produce artifactual light-induced phase separation. See Section 4.S.3. for additional details.

### 4.3.3 Terminology

We use the term “trajectory” to mean a series of samples along a specified path of compositions. Trajectories are used to examine the compositional dependence of a measurement such as FRET. We note that the mixtures studied here should be considered pseudo-ternary because we neglect all components of the aqueous buffer. Most important, we neglect water on the basis that its chemical potential is constant at every lipid composition examined because of the presence of excess water. Even so, the water composition of each phase varies over the phase diagram, and we do not measure its fraction in any of the phases. BSM is composed of various species, but for our purposes we count it as a single high- $T_m$  component. Gentle hydration requires use of small fractions of charged lipid, and we used 2% DPPG or 2% POPG (% of total lipid). These small fractions have been shown to have no effect on phase boundaries [89].

Within a tetrahedral phase diagram it is convenient to refer to compositions in terms of the fractional replacement of nanoscopic-inducing lipid by macroscopic-inducing lipid, which we term “ $\rho$ ”. Here we define  $\rho$  as:

$$\rho \equiv [\text{SDPC}] / ([\text{SDPC}] + [\text{POPC}])$$

We also define a “ $\rho$  window” to be bounded by two  $\rho$  values at which 50% of observed morphologies, which can be modulated or macroscopic or uniform, are modulated at each  $\rho$  value

#### 4.3.4 FRET, DHE → BoDIPY-PC

A series of trajectories, each with ~70 samples, was prepared in order to locate the boundaries of the Ld + Lo region. The precise location of boundaries was extracted from the features of the DHE → BoDIPY-PC stimulated acceptor emission data, as described [90-92].

Samples for FRET measurement were prepared by use of rapid solvent exchange (RSE) to minimize cholesterol de-mixing [90]. 250 nmol total lipid per sample along with dyes were dispensed into 13 mm glass tubes with a 25  $\mu$ L Hamilton syringe attached to a repeating dispenser (Hamilton USA, Reno, NV). Dye concentrations were 1 mol% for DHE and 0.066 mol% for BoDIPY-PC. Deoxygenated RSE buffer (0.500 mL, 200 mM KCl, 5 mM PIPES, 50  $\mu$ M DTPA, pH 7.0) was added to the chloroform solution of lipids and dyes. Samples were vortexed under vacuum (~670 mTorr) for 1 min, sealed under argon and placed in a water bath at 48 °C. At each sample preparation step, the temperature was chosen to ensure that all lipids were melted and thus well-mixed during formation of vesicles. For BSM-containing mixtures, 48 °C is above the BSM melting range of 35 - 45°C. Samples were cooled at 2 °C/h to 23 °C, then equilibrated at room temperature for 24 h before measurements. 1.90 mL of deoxygenated RSE buffer was added to 0.100 mL of sample to yield 25  $\mu$ M lipid in the cuvette. Data were collected on a Hitachi F-7000 FL spectrofluorimeter (Hitachi High Technologies America, Schaumburg, IL) at ambient temperature of 23°C, under a gentle stream of argon above the cuvette. Using 2.5 nm bandpass for excitation and emission slits and 10 s integration time, intensity was measured in 4 channels (ex/em): DHE fluorescence (327/393 nm), BoDIPY-PC sensitized emission (327/517 nm),

BoDIPY-PC direct fluorescence (500/517 nm), and light scattering (440/430 nm). Control samples were prepared to correct for non-FRET contributions as described previously [27, 90] in order to account for direct fluorescence emission from donor and acceptor, and scattering of excitation light by the vesicle suspension.

### **4.3.5 GUV imaging**

#### **4.3.5.1 GUVs preparation by gentle hydration**

The gentle hydration method for making GUVs was first introduced by Reeves and Dowben [93], and significantly modified by Akashi et al. [94]. We describe below some observations and changes made to this procedure that are specifically relevant for phase behavior studies of lipid mixtures. Negatively-charged lipids provide electrostatic repulsion between bilayers, which facilitates formation of GUVs from the layers of lipid film deposited on the walls of a glass tube. Higher temperature and longer equilibration times were avoided to minimize oxidation and free radical chain reactions that degrade PUFA lipids.

#### **4.3.5.2 GUVs preparation by electroswelling**

GUVs were also prepared by a modified electroswelling procedure as described [103-107]. Briefly, each sample contained 250 nmol of lipid mixture in 200  $\mu$ L chloroform, dispensed in an inert atmosphere glove box. Small fractions of fluorescent dyes C12:0 DiI (0.02 mol%) and naphthopyrene (0.07 mol%) were added. A lipid film was created by evenly spreading the chloroform solution onto indium tin oxide (ITO)-coated microscope slides (Delta Technologies, Stillwater, MN) on a hotplate with surface temperature measured to be  $\sim$ 50  $^{\circ}$ C. After the residual solvent had been removed under vacuum for 2 h at  $\sim$ 50 mTorr, ITO slides were sealed with Buna-

N O-rings to create a chamber, which was then filled with deoxygenated 100 mM sucrose containing 50  $\mu$ M DTPA. The films were held for 2 h at 50 °C in an AC field of 5 Hz,  $\pm$  1 Vpp, using a Wavetek FG2C function generator (Meterman, Everett, WA) followed by 10 h of cooling to 23°C using a Digi-sense temperature controller R/S (Cole Palmer, Vernon Hills, IL). GUVs were harvested into deoxygenated 100 mM glucose solution under inert atmosphere, then allowed to settle for 1 h before microscopy observations at 23 °C.

#### **4.3.6 Fluorescence microscopy**

For all gentle hydration experiments, a Nikon Eclipse Ti microscope (Nikon Instruments, Melville, NY) was used for wide-field fluorescence microscopy at 23 °C, using a 60X 1.2 NA water immersion objective. GUVs prepared by electroswelling sometimes contained naphthopyrene at 0.07 mol% as a dye with preferential Lo phase partitioning. Naphthopyrene was not used in samples prepared by gentle hydration in order to minimize light-induced artifacts. Images were taken with an Andor Zyla sCMOS camera (Oxford Instruments, South Windsor, CT). Most GUVs prepared by electroswelling were imaged with a different microscope, a Nikon Diaphot-TMD microscope (Micro Video Instruments Inc., Avon, MA) for wide-field fluorescence microscopy at 23 °C, with a 60X 1.4 NA oil immersion objective. Images were recorded with a Photometrics charge-coupled device camera CoolSNAP HQ2 (Tucson, Arizona). C12:0 DiI fluorescence was imaged with ex/em 546/585 nm; naphthopyrene with 436/480 nm. Images from GUVs containing multiple dyes were color-merged using NIS software, with BoDIPY-PC green, C12:0 DiI red, and naphthopyrene blue. For GUVs shown in this study, very low dye levels together with short exposure times required image contrast to be increased with NIS Elements Basic Research Software (MVI, Inc.).

### **4.3.7 Critical point investigation and percolation map**

The critical point of the Ld + Lo region was found by determining the continuous, “percolating” phase as a function of composition to obtain a “percolation map”. Percolation map refers to the set of marked compositions within an area of the phase diagram to discover at which compositions the changeover occurs from Lo being continuous to Ld being continuous (Fig. 4.4). The Ld + Lo percolation map near the critical point was examined by analyzing ~50-100 GUVs at each composition. The locus of compositions where connectivity in GUVs changes between Ld and Lo was extrapolated to its intersection with the Ld + Lo upper phase boundary, thereby marking the critical point [27]. We note that for compositions in the middle region of the tieline, where the area fractions of Lo and Ld phases are close to equal, the majority of GUVs displayed a single round Ld (or Lo) domain. This is an indication that the samples were well equilibrated, without multiple small kinetically trapped domains. We found that the percolation changeover point occurs where the area fraction of Ld is roughly equal to that of Lo.

## **4.4 Results**

### **4.4.1 FRET, DHE → BoDIPY-PC**

We make use of changes in FRET as donor and acceptor dyes partition between coexisting phases. When dyes concentrate within the same phase, their average separation distance decreases, resulting in a compositional region of enhanced FRET efficiency (REE). When dyes prefer different phases, the increase in average dye separation leads to a region of reduced FRET efficiency (RRE). Here we used the donor/acceptor FRET dye pair DHE/BoDIPY-PC, which

partition into Lo and Ld phase, respectively, to generate RREs where Ld and Lo phases coexist. Fig. 4.1 shows representative FRET trajectories prepared to locate boundaries. Trajectories T1 and T2 were used to locate the boundaries of the coexistence region Ld + Lo (Fig. 4.1A-C). FRET data for trajectory T1 (Fig. 4.1A and 2B) were used to determine the LHS and RHS boundaries of this region. T1 shows the appearance of Lo at  $\chi_{\text{CHOL}} \sim 0.08$ ,  $\chi_{\text{BSM}} \sim 0.22$ , and the appearance of Ld at  $\chi_{\text{CHOL}} \sim 0.32$ ,  $\chi_{\text{BSM}} \sim 0.62$  for the RHS (Fig. 4.2B). Fig. 4.2C shows T2 with boundaries at  $\chi_{\text{CHOL}} \sim 0.12$ ,  $\chi_{\text{BSM}} \sim 0.18$  for the LHS, and  $\chi_{\text{CHOL}} \sim 0.35$ ,  $\chi_{\text{BSM}} \sim 0.55$  for the RHS.

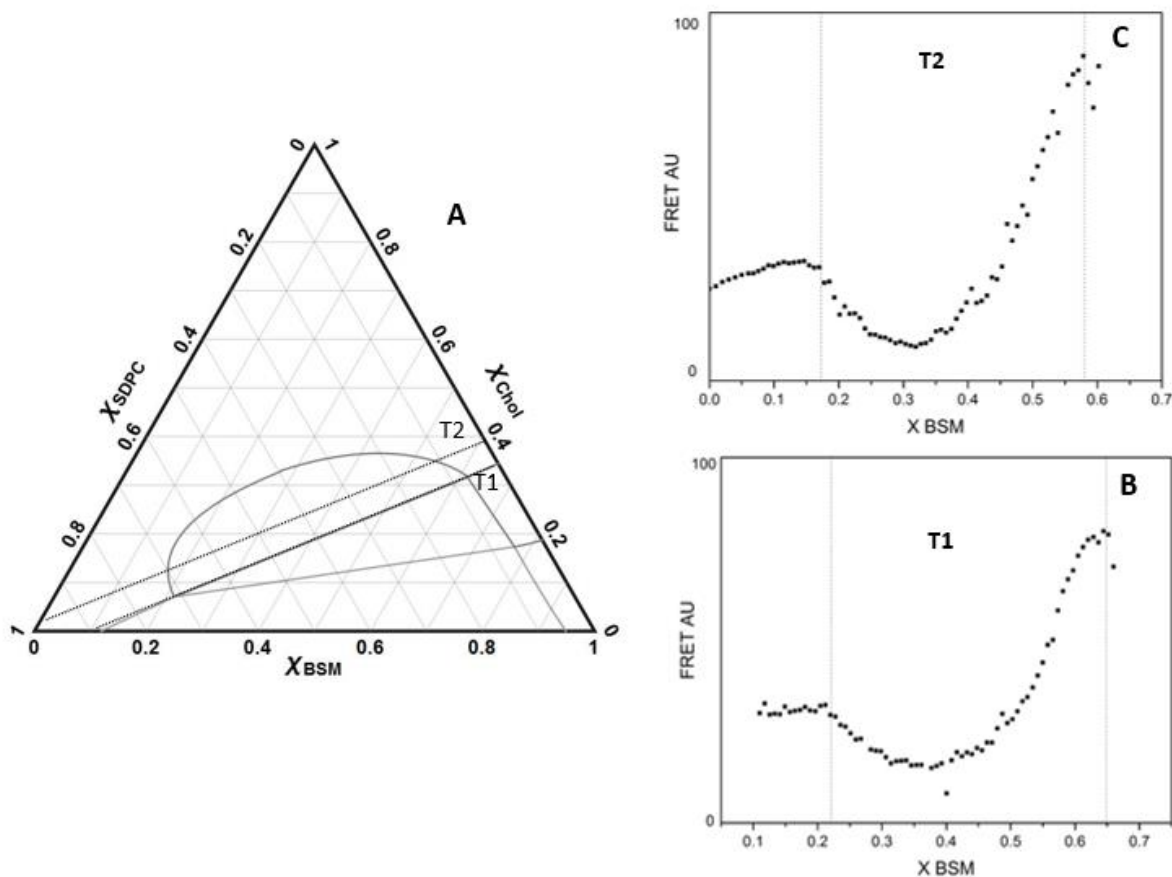


**Figure 4.1** FRET trajectories T1 and T2 determine Ld + Lo phase boundaries with high accuracy. (A) T1 and T2 are shown as dashed lines. Phase boundaries are shown in grey for reference. T1 compositions  $0.11 \leq \chi_{BSM} \leq 0.65$  and  $0 \leq \chi_{CHOL} \leq 0.35$ ; T2 compositions  $0 \leq \chi_{BSM} \leq 0.6$  and  $0.03 \leq \chi_{CHOL} \leq 0.4$ . DHE, Bodipy-PC and C12:0 DiI were 1 mol%, 0.066 mol% and 0.05 mol% respectively. (B) FRET along T1 using 2-dye pair DHE  $\rightarrow$  BoDIPY-PC to locate boundaries. FRET changes abruptly at the onset of a phase transition, allowing precise boundary determination (vertical lines show fit for slope change and location of the phase boundary where Ld + Lo phase coexistence appears/disappears.) (C) FRET along T2 using 2-dye pair DHE  $\rightarrow$  BoDIPY PC to locate boundaries.

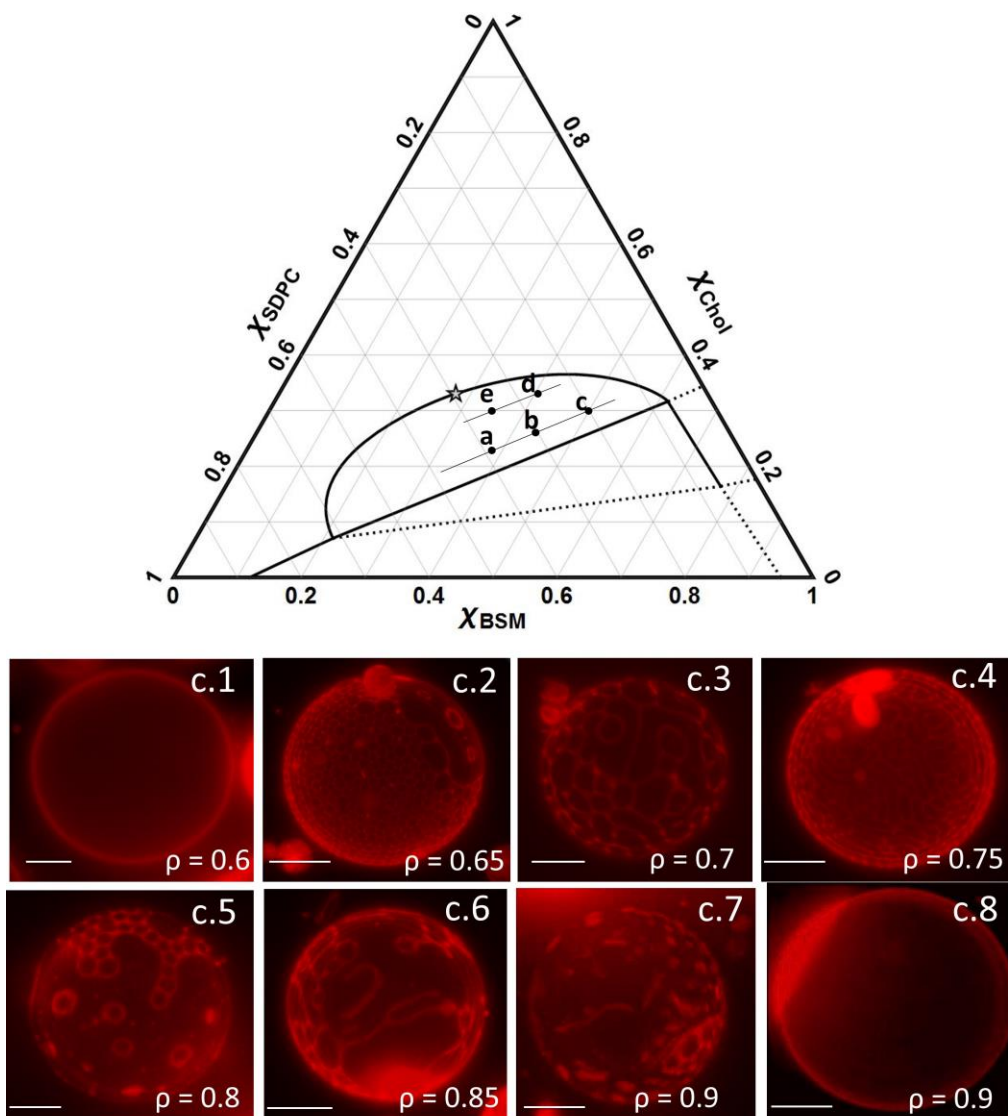


**Figure 4.2** Modulated phase patterns are observed. Phase diagram shows compositions examined for BSM/(SDPC+POPC)/Chol: 0.39/0.39/0.22 (a); 0.44/0.30/0.26 (b); 0.50/0.20/0.30 (c); 0.41/0.26/0.33 (d); 0.35/0.35/0.30 (e). A progression of morphologies from uniform to modulated to round macroscopic domains is observed (c.1-c.8) for composition (c) 0.41/0.26/0.33. Images were contrast and brightness enhanced. GUVs appeared uniform before the onset of modulated phases ( $\rho < 0.64$ ), and showed macroscopic round domains at  $\rho > 0.90$ . Composite 3D images for each GUV were obtained by combining slices along a z stack series. At each composition  $\rho$  slices share common Chol and BSM endpoints, with varying  $\rho$ . DiI used at 0.011 mol% partitions into Ld. Temperature 23 °C. Scale bar 10 microns.

## **4.4.2 Microscopy imaging on GUVs**

### **4.4.2.1 Phases observed on GUVs**

BSM/SDPC/Chol shows macroscopic phase coexistence in three regions, Ld + Lo, Ld + Lo + L $\beta$ , and Ld + L $\beta$ . Fig. 4.5 shows upper Ld + Lo boundaries determined by the gentle hydration method. Fig. 4.8 shows representative GUV images used to determine the LHS boundary of the Ld + L $\beta$  region.

### **4.4.2.2 Upper boundary determination**

The upper BSM/SDPC/Chol boundary terminates at a maximum  $\chi_{\text{CHOL}} \sim 0.37$ , as determined by GUV imaging (Fig. 4.5) and FRET experiments using the donor/acceptor pair DHE/BoDIPY-PC (data not shown). This maximum cholesterol fraction is slightly lower than the  $\chi_{\text{CHOL}} \sim 0.40$  found for POPC- or DOPC-containing mixtures at 25°C, and reflects the slight but unexpectedly higher miscibility of cholesterol with SDPC.

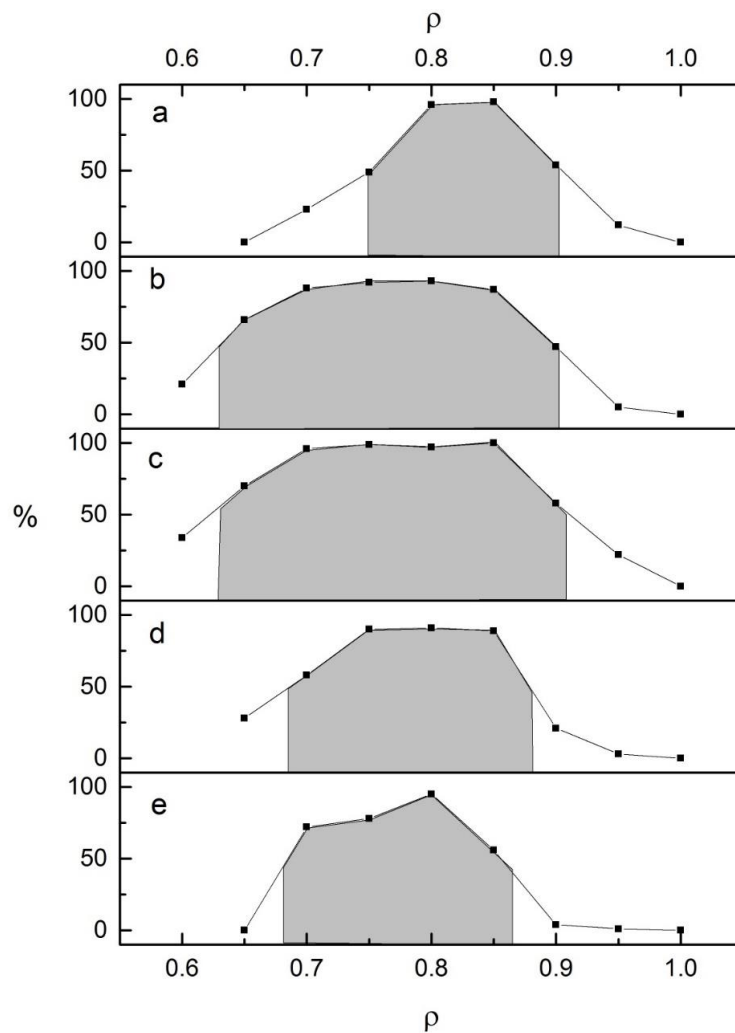


**Figure 4.3** The  $\rho$  values for the modulated phase windows vary along two tielines. Panels (a-e) correspond to compositions (a-e) examined. Compositions BSM/(SDPC+POPC)/Chol are (a-e): 0.39/0.39/0.22 (a); 0.44/0.30/0.26 (b); 0.50/0.20/0.30 (c); 0.41/0.26/0.33 (d); 0.35/0.35/0.30 (e). % of GUVs showing modulated morphology at various  $\rho$  values are graphed. Solid area under each plot corresponds to the width of  $\rho$  window. Here we define  $\rho$  window to be bounded by two  $\rho$  values at which at least 50% of observed morphologies are modulated (from counting % of modulated, macroscopic and uniform morphologies observed at each  $\rho$  value at a given composition). Points (a-c) lay along lower Chol tieline and points (d-e) lay along higher Chol tieline.

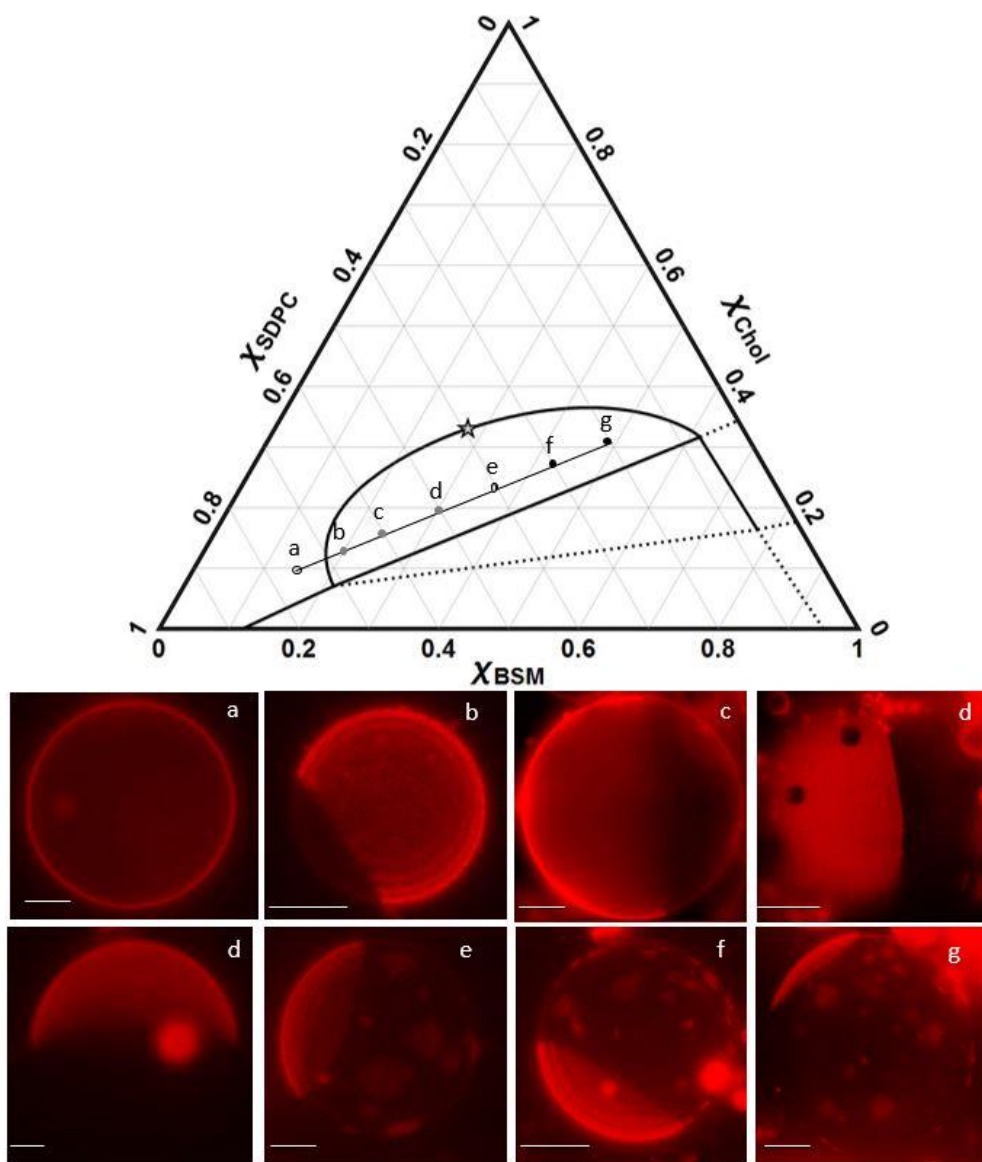


**Figure 4.4** Percolation threshold study at  $\rho = 1$  (BSM/SDPC/Chol). Percolation maps enable finding critical points, marked by star. Boundaries for the Ld + Lo region are shown for reference. Filled circles, GUVs within Ld + Lo phase coexistence with Lo as the percolating phase; grey circles, Ld is the percolating phase; open circles, GUVs are uniform within a one phase region; half black/white circles, GUVs exhibiting both types of connectivity. Critical points BSM/SDPC/Chol 0.28/0.39/0.33. Representative GUVs (a-g) are shown corresponding to each composition (a-g). GUV compositions BSM/SDPC/Chol are: (a) 0.15/0.75/0.1; (b) 0.2/0.67/0.13; (c) 0.25/0.60/0.15; (d) 0.3/0.5/0.2; (e) 0.37/0.40/0.23; (f) 0.43/0.30/0.27; (g) 0.48/0.20/0.31. Temperature 23 °C. Scale bar 10 microns.

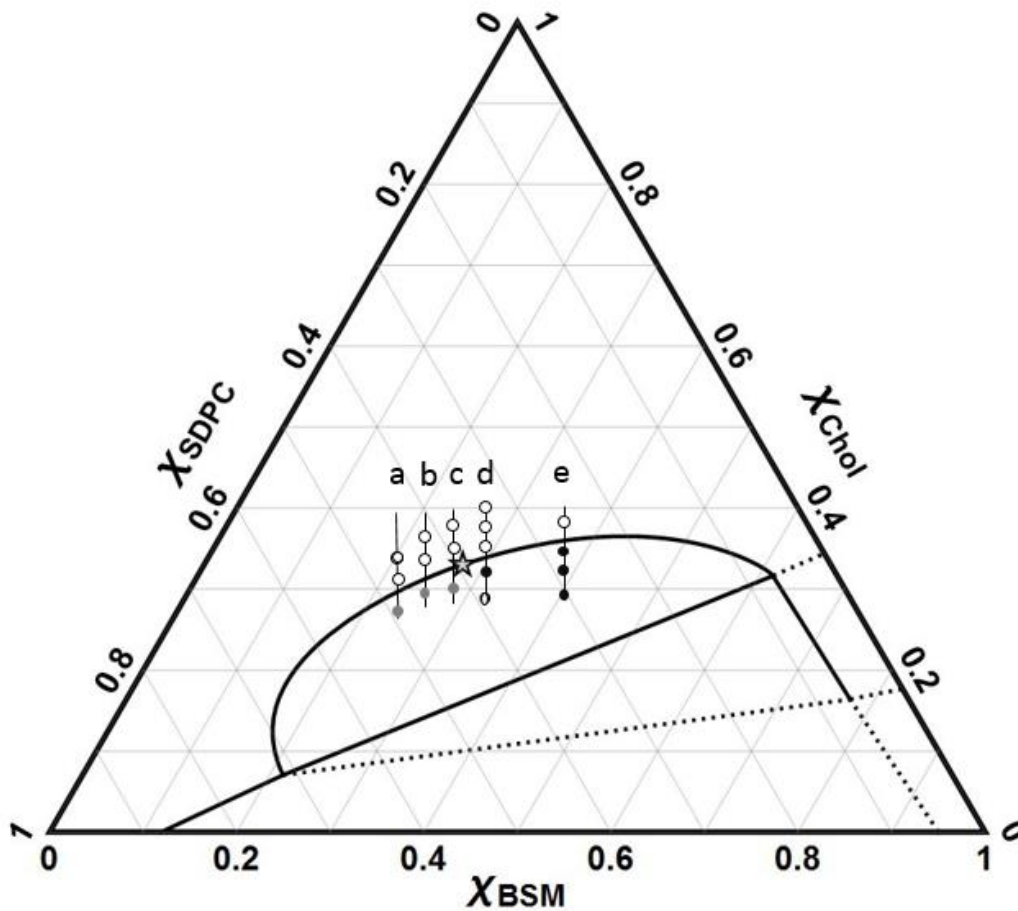


**Figure 4.5** Critical point investigation and boundaries determined by GUVs (prepared by gentle hydration). Representative trajectories (a-e) are shown. Boundaries for the Ld + Lo region are shown for reference. Filled circles, GUVs within Ld + Lo phase coexistence with Lo as the percolating phase; grey circles, Ld is the percolating phase; open circles, GUVs are uniform within a one phase region; half black/white circles, GUVs exhibiting both types of connectivity. The critical point is at BSM/SDPC/Chol = 0.28/0.39/0.33.

### 4.4.2.3 Region of modulated phase domains

Fig. 4.2 and Table 4.1 show 5 compositions examined in this modulated  $\rho$  window study of BSM/SDPC/POPC/Chol. Points (a-c) in Fig. 4.2 and Table 4.1) are on a tieline at lower  $\chi_{\text{CHOL}}$  and points (e-d) are on a tieline at higher  $\chi_{\text{CHOL}}$ . We define the  $\rho$  window as bounded by two  $\rho$  values at which 50% of observed morphologies are modulated. For a tieline located just above the three-phase coexistence region, points a-c, modulated phases were observed over the range  $0.75 < \rho < 0.90$  (point a: Fig. 4.3, top panel a); and over the range  $0.64 < \rho < 0.90$  (points b and c: Fig. 4.2, panels b and c). At a higher cholesterol tieline, where the compositions of the coexisting phases are closer and phase properties likely to be more similar, a very similar modulated phase window of  $0.68 < \rho < 0.84$  was observed (Fig, 4.4, panels d and e). Thin Ld stripes with Lo being the percolating phase were prevalent in compositions towards higher Lo fractions, points (c) and (d), consistent with the Lever Rule and previous observations in DSPC-containing mixtures [79].

Composition	$\rho$	Uniform (%)	Modulated (%)	Macroscopic (%)	N
a	0.65	100	-	-	87
	0.7	77	23	-	92
	<b>0.75</b>	51	49	-	112
	<b>0.8</b>	4	96	-	69
	<b>0.85</b>	-	98	2	55
	<b>0.9</b>	-	54	46	79
	0.95	-	12	88	54
1	-	-	100	87	
b	<b>0.65</b>	34	66	-	124
	<b>0.7</b>	12	88	-	115
	<b>0.75</b>	1	92	7	132
	<b>0.8</b>	-	93	7	95
	<b>0.85</b>	-	87	13	80
	<b>0.9</b>	-	47	53	99
	0.95	-	5	95	91
1	-	-	100	71	
c	<b>0.65</b>	30	70	-	108
	<b>0.7</b>	3	96	1	66
	<b>0.75</b>	-	99	1	111
	<b>0.8</b>	-	97	3	83
	<b>0.85</b>	-	100	-	51
	<b>0.9</b>	-	58	42	92
	0.95	-	22	78	73
1	-	-	100	46	
d	0.65	72	28	-	104
	<b>0.7</b>	41	58	1	109
	<b>0.75</b>	5	90	5	71
	<b>0.8</b>	6	91	3	67
	<b>0.85</b>	-	89	11	54
	0.9	-	21	79	133
	0.95	-	3	97	88
1	-	-	100	45	
e	0.65	100	-	-	55
	<b>0.7</b>	26	72	2	123
	<b>0.75</b>	9	78	13	76
	<b>0.8</b>	2	95	3	84
	<b>0.85</b>	-	56	44	88
	0.9	-	4	96	71
	0.95	-	1	99	69
1	-	-	100	53	
Composition	$\rho$	Uniform (%)	Modulated (%)	Macroscopic (%)	N

**Table 4.1.** Percentage of GUVs with main observed morphologies. GUVs were classified as having 3 main regimes: uniform, modulated or macroscopic Ld +Lo coexistence. % of each morphology was recorded and used to determine the  $\rho$  window for each composition.

#### 4.4.2.4 Critical point investigation and percolation map

The critical point was experimentally found by determining the continuous, percolating, phase as a function of composition to obtain a percolation map (Figs. 4.5 and 4.6). The critical point was determined to be at BSM/SDPC/Chol = 0.28/0.39/0.33 (Fig. 4.1). In the SDPC-rich Ld phase that is in equilibrium with a BSM-rich Lo phase, at a cholesterol concentration of about 37 mol% the phases become indistinguishable; this is the critical point. Critical fluctuations were also observed for compositions near the critical point.

#### 4.4.3 GUVs formed by electroswelling

We began studies of the BSM/SDPC/Chol mixture by preparing GUVs using the method of electroswelling. However, we soon learned that this method produces artifacts. Fig. 4.7 shows that for GUVs made by electroswelling, upper and LHS boundaries are artifactually expanded, indicating wider immiscibility. GUVs made by electroswelling showed macroscopic phase separation for Ld + Lo, Ld + Lo + L $\beta$ , and Ld + L $\beta$  phase regions, consistent with GUVs made by gentle hydration, but the boundaries are artifactually expanded. Furthermore, the RHS of the Ld + Lo coexistence region cannot be determined accurately by GUVs due to the difficulty of preparing GUVs with a high mole fraction of BSM, as shown in Fig. 4.7.

## 4.5 Discussion

### 4.5.1 Description of ternary phase diagram

Fig. 4.6 shows the BSM/SDPC/Chol phase diagram, obtained by FRET and GUVs made by gentle hydration. We describe below the individual phase regions.

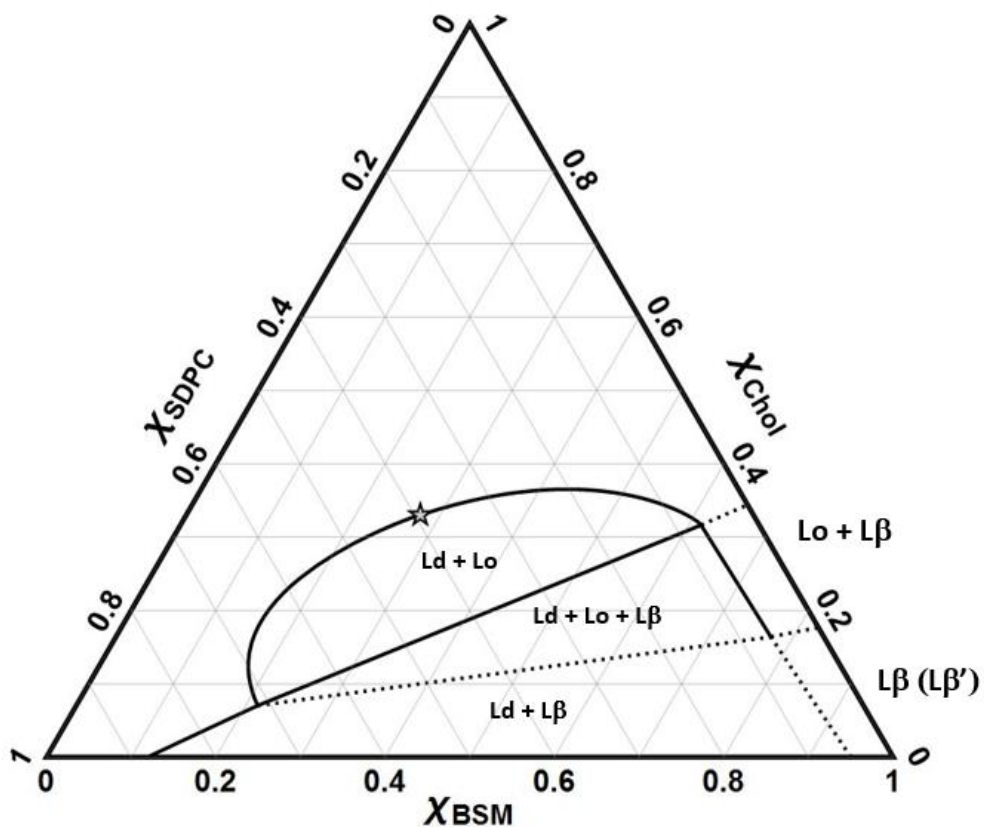


**Figure 4.6** Phase diagram of BSM/SDPC/Chol obtained by FRET and by microscopy imaging on GUVs made by gentle hydration method, all at 23 °C. Solid lines show measured phase boundaries, dashed lines boundaries that are putative or extrapolated.

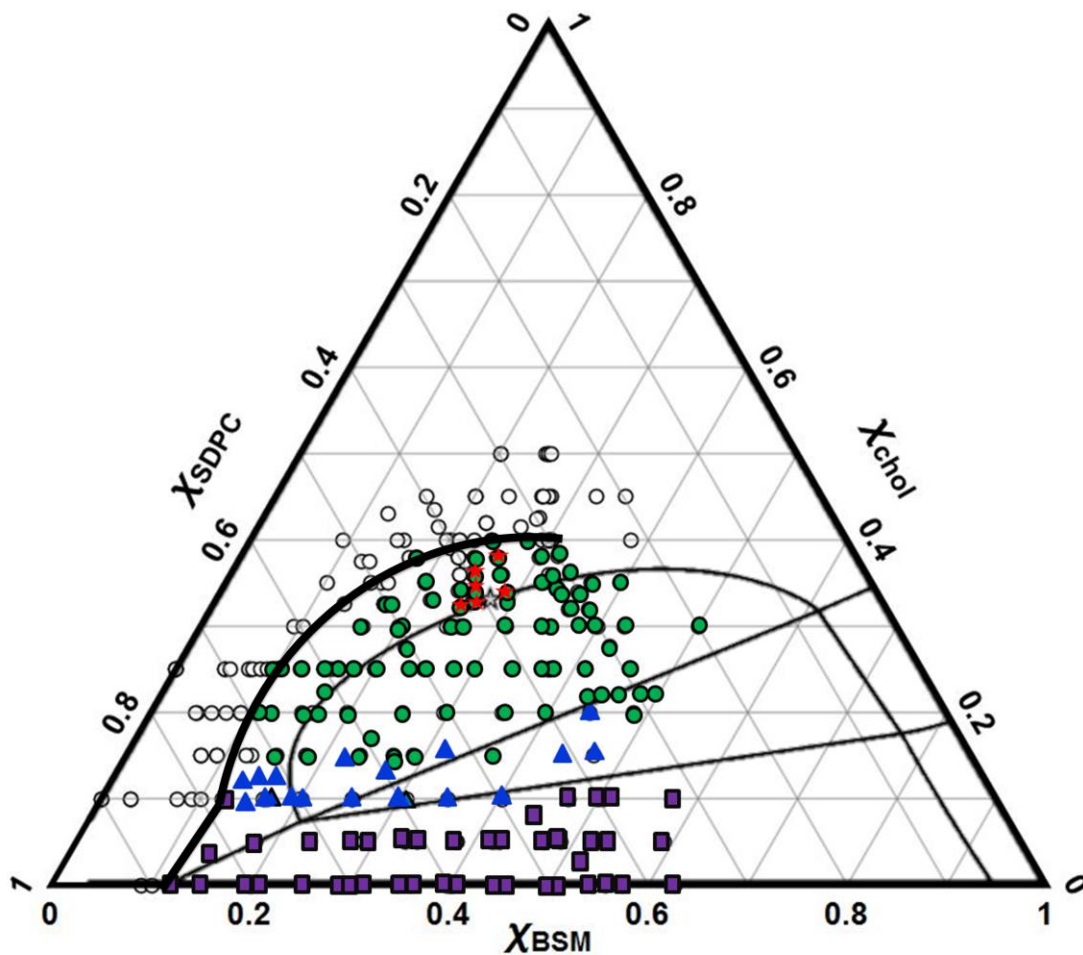


**Figure 4.7** Electroswelling produces artifactual domains, yielding “expanded” boundaries for  $L_d + L_o$  in BSM/SDPC/Chol. Open circles show where uniform GUVs appear; green closed circles are macroscopic  $L_d + L_o$ ; blue triangles mark compositions within  $L_d + L_o + L_\beta$ ; and purple squares mark  $L_d + L_\beta$  compositions. Solid lines are real boundaries. Red stars indicate critical fluctuations observed by electroswelling. Thick black line indicates boundaries obtained by electroswelling. Boundaries obtained by FRET and gentle hydration (from Figure 4.6) are shown for comparison.

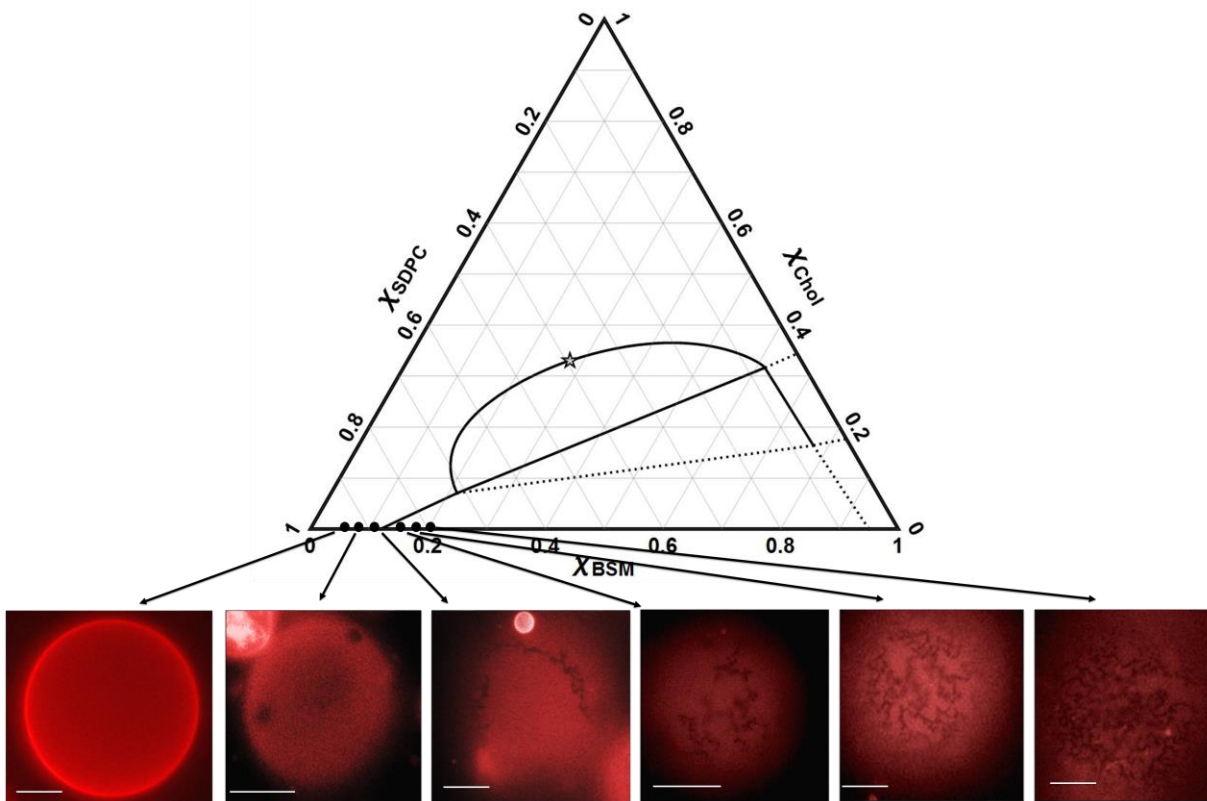


**Figure 4.8** Locating the LHS boundary at zero cholesterol. Six representative compositions are shown (a-f). Temperature 23 °C. Scale bar 10 microns. Gel domains become thicker as  $\chi_{BSM}$  increases.

BSM/SDPC/Chol is a Type II diagram, with three regions of macroscopic phase separation:

Ld + Lo, Ld + Lo + L $\beta$ , and Ld + L $\beta$ .

## 4.5.2 Phase regions

### 4.5.2.1 Liquid + gel coexistence, Ld + L $\beta$ ( $\beta'$ )

The upper boundary of the Ld + L $\beta$ ( $\beta'$ ) region is a line that is also the lower boundary of the 3-phase coexistence region Ld + Lo + L $\beta$ . The LHS boundary at  $\chi_{\text{CHOL}} = 0$  of this region indicates the maximum solubility of BSM in SDPC-rich Ld to be  $\chi_{\text{BSM}} = 0.12$ . The RHS boundary of Ld + L $\beta$ ( $\beta'$ ) is approximated by extrapolating the measured RHS of the Ld + Lo + L $\beta$  region to  $\chi_{\text{CHOL}} = 0$ , and shows that SDPC is rather insoluble in the BSM-rich L $\beta'$  phase, with  $\chi_{\text{SDPC}} \sim 0.05$  without cholesterol, similar to the boundary reported by Petruzielo et al for BSM/DOPC. The maximum solubility of cholesterol in the BSM-rich L $\beta$  phase is at  $\chi_{\text{CHOL}} \sim 0.16$ . This maximum cholesterol solubility in L $\beta$  is the same as found for the similar mixtures BSM/DOPC/Chol and BSM/POPC/Chol [29], as well as for other mixtures of DSPC/DOPC/Chol, DSPC/POPC/Chol [27], and DPPC/DLPC/Chol [95]. Note that  $\chi_{\text{CHOL}} \sim 0.16$  corresponds closely to each cholesterol being surrounded by a single shell of 6 phospholipid neighbors, with the clear implication that this solid phase cannot accommodate any higher fraction of cholesterol.

#### 4.5.2.2 Gel [L $\beta$ (L $\beta'$ )]

The pure hydrated lipid BSM at room temperature is a solid with tilted chains, L $\beta'$ . As found for DPPC [96]. Addition of cholesterol causes the chain tilt to disappear but without the formation of a coexisting phase. This gel region L $\beta$ (L $\beta'$ ) is bounded at  $\chi_{\text{SDPC}} = \sim 0.05$ ,  $\chi_{\text{CHOL}} \sim 0.17$ .

#### 4.5.2.3 Liquid-ordered + gel coexistence, $L_o + L_\beta$

These boundaries were chosen to be in agreement with Schreinemakers' Rules [97], and so are only estimates. This almost rectangular region has one edge along the BSM/Chol binary axis from  $\chi_{\text{CHOL}} \sim 0.17 - 0.34$ . Along this axis,  $L_\beta$  transitions to  $L_o$  with increasing cholesterol fraction as a continuous phase change [96].

#### 4.5.2.4 3-phase coexistence, $L_d + L_o + L_\beta$

GUV data and FRET data for trajectory T1 (Fig. 4.1A and 4.1B) were used to determine the LHS and RHS boundaries of this region. In particular, we used the previously determined phase diagram for BSM/DOPC/Chol to guide the choice of trajectory T1, which shows the appearance of  $L_o$  at the point  $\chi_{\text{CHOL}} \sim 0.08$ ,  $\chi_{\text{BSM}} \sim 0.22$ , and the appearance of  $L_d$  at  $\chi_{\text{CHOL}} \sim 0.32$ ,  $\chi_{\text{BSM}} \sim 0.62$  for the RHS (Fig. 4.2B). The  $L_o$  phase that separates anywhere along this tieline has  $\chi_{\text{CHOL}} \sim 0.32$ . The solubility of BSM in  $L_d$  mixtures with SDPC/Chol, POPC/Chol and DOPC/Chol is essentially the same, and that is also the case for the  $L_o$  mixtures: the upper and lower boundaries of the three phase region are nearly independent of the type of low- $T_m$  lipid. The upper and lower boundaries of the  $L_d + L_o + L_\beta$  region are useful because they are thermodynamic tielines. The BSM/DOPC/Chol tieline reported previously by Petruzielo et al agrees well with SSM/DOPC/Chol measurements by Farkas and Webb, who used both polarization imaging of GUVs and mass spectrometry on phase patches excised from GUVs [98].

#### 4.5.2.5 Liquid–liquid coexistence, Ld + Lo

Contrary to published reports, we find that SDPC mixes about as well with BSM and Chol as do DOPC and POPC. This important observation stems from the comparison to other macroscopic mixtures BSM/DOPC/Chol and DSPC/DOPC/Chol, and nanoscopic mixtures BSM/POPC/Chol and DSPC/POPC/Chol. The upper BSM/SDPC/Chol boundary has a maximum  $\chi_{\text{CHOL}} \sim 0.37$ , found from GUV imaging (Fig. 4.5) and from FRET experiments using the donor/acceptor pair DHE/BoDIPY-PC (data not shown). Similarly, the upper Ld + Lo boundary in BSM systems for *both* DOPC and POPC mixtures terminates at  $\chi_{\text{CHOL}} \sim 0.40$  at 25 °C [29]. Thus we observe that SDPC has similar miscibility gaps in mixtures with cholesterol and BSM, compared to mixtures with DOPC or POPC with BSM and cholesterol. As discussed in the Introduction, many previous studies indicated poor solubility of DHA-containing lipids with Chol. Thus, we expected to see a larger region of immiscibility in the BSM/SDPC/Chol system. A recent study [65] shows that the solubility of a DHA-containing lipid in mixtures with SM/Chol depended on whether the glycerophospholipid was PC or PE. Solid state  $^2\text{H}$ NMR studies on PSM/PDPE-d31/Chol = 1/1/1 mol) showed that PE with a DHA chain separates away from regions enriched in PSM and cholesterol [65]. In contrast,  $^2\text{H}$ NMR spectra for PSM/PDPC-d31/Chol = 1/1/1 mol) showed that PC with a DHA chain is more miscible in PSM-rich/sterol-rich domains.

#### 4.5.3 Region of modulated phase domains

The size and the morphology of phase domains can be controlled by the composition and type of low- $T_m$  lipid used in mixtures with high- $T_m$  lipids such as DSPC, SM or DPPC, and

cholesterol. There are 3 regimes of different morphology within the Ld + Lo liquid-liquid coexistence region of GUVs: uniform (nanoscopic), modulated, or macroscopic domains. The first experiments to address morphology changes in Ld + Lo region examined a titration series joining two ternary systems in the Ld + Lo regions of DSPC/DOPC/Chol and DSPC/POPC/Chol [78, 79]. Spatially modulated domain features were obtained for sample compositions in the range  $0.15 < \rho < 0.35$ , whereas for  $\rho > 0.35$ , large round, macroscopic domains were observed [78, 79]. When line tension dominates any other interactions that depend on domain size, coexisting liquid phases round up into large circular domains to minimize their perimeter. This simple morphology can be modulated when interactions of sufficient magnitude compete with line tension, so that patterns appear—a maze of stripes, tiny round domains, curved lines, and branched lines [80]

In BSM/SDPC/POPC/Chol we observed  $\rho$  windows of  $0.65 < \rho < 0.90$  for the five compositions examined (Fig. 4.3 and Section 4.S.4), which is a much higher fraction of SDPC than the fraction of DOPC in the previously described systems [78, 79]. In other words, to create modulated phases, a much higher fraction of the mixture needs to be the macroscopic-inducing SDPC, compared with other macroscopic-inducing lipids such as DOPC or DiPhyt-PC. With DSPC/DOPC/POPC/Chol, only ~15% replacement of POPC by DOPC is needed to detect modulated morphology, and by 30% replacement DOPC macroscopic phases are predominant. In this current study we find that it takes ~70% replacement of POPC by SDPC to induce modulated phases, with macroscopic morphology becoming predominant at ~95% SDPC. These observations have implications for cell membranes, pointing to the possible compositional regime where cells could abruptly change the size and connectivity of membrane domains through slight changes in local membrane composition.

#### 4.5.4 Critical point investigation

Locating the critical point can be useful [99-101]. As previously discussed, both Type II and Type I phase diagrams have the same form: a central three phase region joining three two phase regions. For both types of phase diagrams, the Ld + Lo region terminates in a critical point. In this study we show the location of the critical point to be at BSM/SDPC/Chol = 0.28/0.39/0.33, quite similar to the critical point found in related mixtures [27-29, 98]. In other studies, micropipette aspiration of GUVs was used to measure composition-dependent trends in line tension within the Ld + Lo region of eSM/DOPC/Chol, showing a critical point near 0.26/0.34/0.40 [102]. One important reason to know the location of critical point is that line tension must approach zero near a critical point. This has been demonstrated experimentally in ternary systems both by varying temperature at a fixed composition toward an upper miscibility critical point [99], and by varying composition at fixed temperature toward a consolute point [102].

#### 4.5.5 Comparison of boundaries obtained by electroswelling and by gentle hydration

As described in Section. 4.S.1, electroswelling produced artifactually expanded boundaries in the Ld + Lo and Ld + Lo + L $\beta$  regions of the BSM/SDPC/Chol mixture. Fig. 4.7 illustrates superposition of compositions examined by electroswelling over the phase boundaries obtained by FRET and GUVs made by gentle hydration. Electroswelling significantly expands the miscibility gap. Note that regions of liquid-liquid coexistence (Ld + Lo and Ld + Lo + L $\beta$ ) are the most susceptible to this artifactual expansion. In contrast, the Ld + L $\beta$  boundaries are in agreement with those from gentle hydration and FRET data.

## 4.6 Summary

1. We determined the first phase diagram (BSM/SDPC/Chol) that models an animal cell plasma membrane containing only naturally abundant lipids, including a PUFA-containing lipid, SDPC.
2. The phase diagram is a Type II mixtures, thus having macroscopic phase separation regions: Ld + Lo; Ld + Lo + L $\beta$ ; and Ld + L $\beta$ .
3. Compared with phase diagrams of BSM/cholesterol with either DOPC or with POPC, BSM/SDPC/Chol shows comparable regions of immiscibility. This was an unexpected result, as it is often thought that PUFAs mix poorly with BSM-rich/Chol-rich domains.
4. SDPC is a naturally abundant lipid that yields macroscopic domains in mixtures with BSM and Chol. However, it requires only a small fraction of POPC, ~30 mole%, to yield nanoscopic Ld + Lo domains.
5. Sample preparations with SDPC, using gentle hydration and RSE, were necessary to avoid PUFA breakdown.

## Supplemental Materials

### S. 1. Artifacts produced by electroswelling

#### S.1.1. Expanded boundaries

The two different GUV preparation methods each have their own advantages and disadvantages: gentle hydration enables GUV formation with PUFA-containing mixtures with minimal breakdown, but the yield of GUVs can be low, with many multilamellar vesicles and smaller GUV diameters (~30-50  $\mu\text{m}$ ). Electroformation on ITO-coated slides gives high yield of GUVs and larger diameter of vesicles (up to 100  $\mu\text{m}$ ), but some electrode-induced artifacts are apparent. One of those observed artifacts is an expansion of Ld + Lo upper and LHS boundaries produced by the electroswelling method. It was reported before [98, 67] that electroformation with BSM-containing mixtures is prone to such artifacts. Farkas [98] observed expansion of the Ld + Lo region in the SM/DOPC/Chol phase diagram, which was dependent on preparation procedure and composition. For samples with SM >30%, the procedure made little difference to phase boundaries. However, for high-DOPC compositions, the phase boundary contracted by shifting toward the RHS for the samples prepared in inert atmosphere conditions on titanium slides, as compared to the same compositions prepared on ITO slides in the presence of O<sub>2</sub>. In this study we have made similar observations: SDPC-containing samples prepared on ITO slides in the absence of O<sub>2</sub> had expanded boundaries as compared to samples of the same composition prepared by gentle hydration, also in the absence of oxygen (Fig. 4.7). Farkas et al [98] did not try to distinguish

between ITO vs. titanium slides or aerobic vs. anaerobic contributions. In our case, all samples made by both gentle hydration and electroswelling were prepared under inert atmosphere conditions, thus the variable was the use of ITO slides in electroformation, versus no electrodes in gentle hydration. Therefore we conclude that the artifactual expansion in phase boundaries is likely due to the use of electrodes and ITO slides and not to presence or absence of oxygen. Since electroswelling is a popular technique for GUV preparation, one must be aware of potential pitfalls of this method and specifically for samples containing either BSM or PUFA lipids.

### **S.1.2. Artifacts produced by electroswelling: budding vesicles**

Electroswelling produced numerous budding GUVs (Fig. 4.S1) within the Ld + Lo region. This fission of phase domains from a GUV leads to a GUV that looks uniform with microscopy, even though the GUV was phase-separated before the budding. GUVs prepared in the Ld + Lo region are susceptible to budding due to their fluid nature; moreover, the presence of SDPC seems to greatly increase the occurrence of fission. This could be due not only to the nature of the SDPC lipid, but also to artifactual breakdown products resulting from the electroswelling method, i.e. reactions occurring on ITO slides under applied voltage, further catalyzed by ROS and initiating a cascade in formation of breakdown products. The budding might well occur during the long period of slow cooling to the desired temperature (10 hours cooling). We note that GUVs in the Ld + Lo region prepared by gentle hydration did not produce budding vesicles. By use of refractive index difference to detect GUVs, together with fluorescence detection of complementary dyes (Fig. 4.S2), budded vesicles can be observed. One caveat when extensive budding occurs is the inability to discern the true phase state of a given GUV. Especially in instances when only one dye is used,

a typical scenario for GUV imaging studies, any pinched-off phase will be dark, i.e. invisible by fluorescence. However, use of DIC or phase contrast enables observation of all vesicles present, regardless of their composition (Fig. 4.S1). The importance of detecting these dark vesicles is apparent: despite their uniform appearance; their presence indicates Ld + Lo phase separation at a given composition. Caution must be taken not to confuse pinched-off vesicles for GUVs with genuinely uniform, one phase composition.

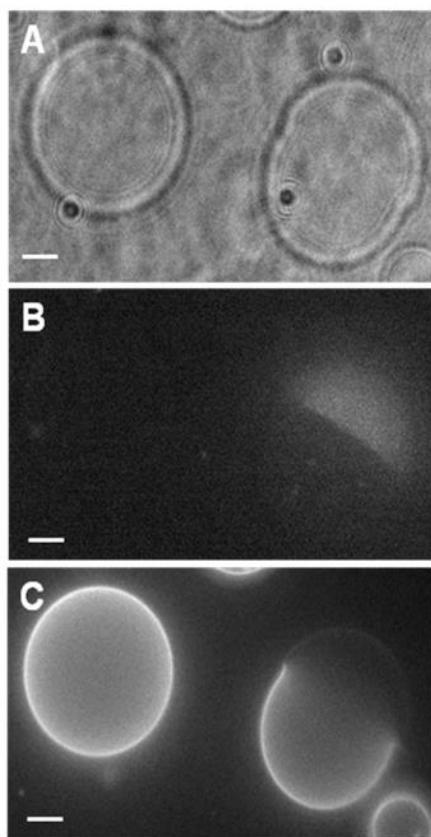


**Figure 4.S1** GUVs of BSM/SDPC/Chol within Ld + Lo phase coexistence region can lack fluorescence and appear invisible, i.e. “dark” in fluorescence imaging. Composition 0.375/0.375/0.25, 100 mM sucrose inside and 100 mM glucose outside. (A) phase contrast image shows all GUVs present in the field of view. (B) C12:0 DiI fluorescence does not show all vesicles (arrow). (C) naphthopyrene reveals the “dark” vesicle in B (arrow shows the same GUV that is dark in (B)). White arrows indicate a budding site visible in GUV. Wide-field illumination, temperature 23 °C, scale bars 10  $\mu$ m.

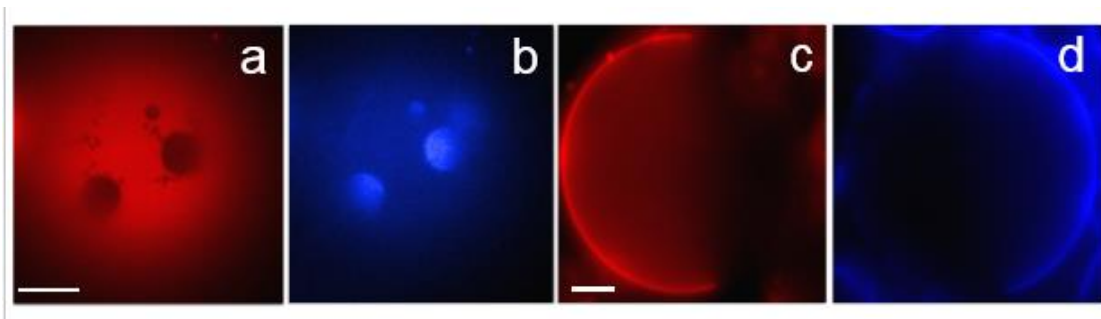


**Figure 4.S2** Complementarity of C12:0 DiI and naphthopyrene reveals a region of Ld + Lo + L $\beta$  phase coexistence (a-b) and Ld + Lo (c-d). (a) C12:0 DiI has a strong preference for Ld round domains; (b) naphthopyrene partitions into round Lo domains and has weaker partitioning into edged L $\beta$  domains. The same GUV of 0.35/0.55/0.10 (BSM/SDPC/Chol) is shown; (c,d) C12:0 DiI (red) and naphthopyrene (blue) have complementary partitioning within Ld + Lo coexistence region. GUV of 0.29/0.38/0.33 (BSM/SDPC/Chol) composition. Wide-field illumination, temperature 23 °C, scale bars 10  $\mu$ m.

## S.2. Cooling rates

We found a cooling rate of 2.5 °C/h over a 10 h cooling time to be sufficient to allow samples to equilibrate. However, samples in the gel region had to be equilibrated for ~ 30 h cooling time (0.83 °C/h) in order for phase-separated domains to be visible. Note that only samples with  $X_{\text{BSM}} > 0.5$  had to be cooled for 30 h. Samples with  $X_{\text{BSM}} < 0.5$  exhibited visible gel domains with 10 h cooling time (Fig. 4.S3). This is consistent with previous observations [87, 98].

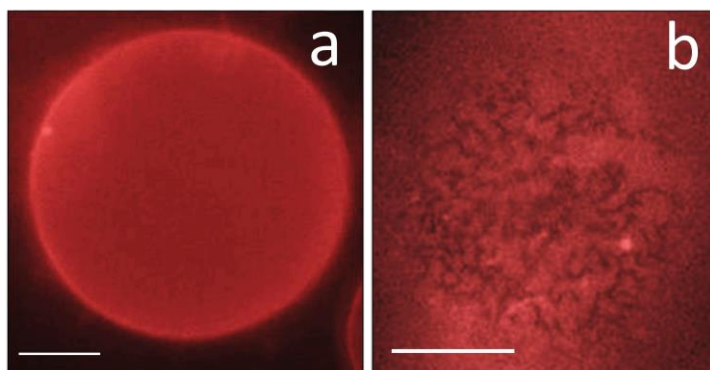


**Figure 4.S3** Slow cooling time needed to create macroscopic phase separation of Ld + L $\beta$ . Ld+L $\beta$  coexistence at 0% chol is observed up to  $\chi_{\text{BSM}}=0.5$  with 10 hours cooling time. GUVs with composition  $\chi_{\text{BSM}} > 0.5$  appear uniform with 10 hr cooling time (a). GUV of 0.5/0.5/0 (BSM/SDPC/CHOL) appears uniform with 10 hr. cooling time (a). However, Ld + L $\beta$  is apparent with 30 hr. cooling time (b). Both vesicles look uniform in the naphthopyrene channel. Wide-field illumination, temperature 23 °C, scale bars 10  $\mu\text{m}$ .

### S.3. Control for photooxidation and light-induced phase separation

Important work by Ayuyan and Cohen points to lipid peroxides and their breakdown products as a source of light-induced domain artifacts [67]. The model starts with photo-excitation of fluorescent probe, release of singlet oxygen and free radical formation, followed by an auto-catalyzed chain reaction and lipid peroxide formation. However, peroxide formation is only one of many possible culprits of light-induced artifacts and the exact molecular steps of light-induced domain formation starting from the excitation of a fluorophore and proceeding to the actual molecular phase separation are not well understood [68, Girotti]. Lipid polymerization or oligomerization upon illumination may contribute to domain formation and macroscopic phase separation, even in mixtures that otherwise appear uniform by fluorescence imaging (e.g. in DSPC/POPC/Chol, SM/POPC/Chol) [68] and may promote artifactual domain growth in

inherently macroscopic systems (e.g. DSPC/DOPC/Chol, SM/DOPC/Chol, and DSPC/SDPC/Chol). Zhao et al [68] suggested that rapid light-induced domain separation might arise from pre-existing lipid clusters. As the boundary of the Ld + Lo region is approached from the high  $\chi_{\text{chol}}$  direction, mixtures closer to the phase boundary (more non-randomly mixed) show faster appearance of light induced domains.

From the experimental standpoint, the sensitivity of a model system to light-induced artifacts depends of many parameters, including: (1) the chemical nature of dyes and lipids used, dye concentration, and lipid composition, especially proximity to a phase boundary; (2) experimental conditions for fluorescent imaging, especially exposure time and light intensity at the sample [more details in 68, 87]. Any lipid can get photooxidized at any double bond, including cholesterol molecules. Mixtures with unsaturated and polyunsaturated lipids should be vigilantly controlled for light-induced artifacts, and some extra steps at the stage of sample preparation might be necessary to eliminate peroxidation and breakdown possible even before the intense light illumination. Both ROS and Fe are known catalysts and prerequisites for a lipid peroxidation cascade, therefore deoxygenating all solvents and chelating Fe with DTPA may be required when working with di- and poly- unsaturated lipids. The use of the free radical scavenger n-propyl gallate was shown to reduce or eliminate light-induced artifacts from occurring [67]; however, it enters the bilayer and changes the phase boundaries [68]. To minimize light-induced artifacts, we used dye concentration as low as 0.011 mol%; DIC rather than fluorescence to locate GUVs, and imaging with low exposure times of ~10 msec.

#### S.4. Modulated phases and $\rho$ window

For samples with large fractions of Lo phase, nearly 100% of vesicles displayed modulated phase patterns at some  $\rho$  value: point (a) had > 50% uniform morphology observed at  $\rho = 0.75$ ; 96% and 98% modulated morphology at  $\rho = 0.80$  and  $0.85$  with a rapid decrease to 54% modulation at  $\rho = 0.90$ . Point (b) had 66% modulation at  $\rho = 0.65$ ; 88% modulated phases at  $\rho = 0.7$ ; >90% modulation at  $\rho = 0.75$  and  $\rho = 0.80$ ; and 87% modulation at  $\rho = 0.85$ ; with a rapid decrease in modulated phases to < 50% (with >50% macroscopic morphologies) at  $\rho = 0.90$ . Point (c) had 70% modulation at  $\rho = 0.65$ ;  $\sim 100\%$  modulated phases at  $0.75 < \rho < 0.85$ , with a rapid decrease to 58% modulated phases (42% macroscopic morphologies) at  $\rho = 0.90$ . Point (d) exhibited > 90% modulation at  $0.75 < \rho < 0.85$ ; with a rapid decrease to 21% modulated morphologies at  $\rho = 0.9$ . At  $\rho = 0.95$  only 3% modulation was observed and 97% of GUVs displayed macroscopic Lo + Ld coexistence. Point (e) had only one  $\rho$  value with > 90% modulated phases,  $\rho = 0.8$ . At values  $\rho < 0.8$  the vast majority of GUVs had uniform appearance and at  $\rho > 0.85$  the vast majority of GUVs exhibited macroscopic phase separation. As the fraction of Lo phase was reduced (i.e., movement along the tieline toward the Ld phase boundary), the fraction of vesicles showing modulated phases decreased (Fig. 4.3 and Table 4.1). Point (a) had the most narrow  $\rho$  window out of all 5 compositions examined. Points (b-c) had  $\rho$  window of  $0.64 < \rho < 0.90$ ; points (d-e)  $\rho$  window of  $0.68 < \rho < 0.84$  (Fig. 4.3).

## References

- [1] G. van Meer. 2005. Cellular lipidomics. *EMBO. J.* 24 3159-3165.
- [2] Phillips M.C., Ladbrooke B.D., Chapman D. 1970. Molecular interactions in mixed lecithin systems. *Biochim. Biophys. Acta.* 196: 35–44.
- [3] Shimshick E.J, McConnell H.M. 1973. Lateral Phase Separation in Phospholipid Membranes. *Biochem.* 12: 2351-2360.
- [4] J.F. Hancock. 2006. Lipid rafts: contentious only from simplistic standpoints, *Nat Rev Mol Cell Biol.* 7:4 56-462.
- [5] Almeida P.F.F., Pokorny A., Hinderliter A. 2005. Thermodynamics of membrane domains, *Biochim. Biophys. Acta.* 1720: 1-13.
- [6] J.F. Hancock, Lipid rafts: contentious only from simplistic standpoints. 2006. *Nat Rev Mol Cell Biol.* 7:456-462.
- [7] Almeida P.F.F., Pokorny A. Hinderliter A. 2005. Thermodynamics of membrane domains, *Biochim Biophys Acta.* 1720:1-13.
- [8] Elson E.L., Fried E., Dolbrow J.E., and Genin G.M. 2010. Phase Separation in Biological Membranes: Integration of Theory and Experiment. *Ann. Rev. Biophys.* 39:207-226.
- [9] Lingwood D. and Simons K. 2010. Lipid Rafts as a Membrane-Organizing Principle. *Science.* 327:46-50.
- [10] Sengupta P., Holowka D., Baird B. 2007. Fluorescence resonance energy transfer between lipid probes detects nanoscopic heterogeneity in the plasma membrane of live cells. *Biophys. J.* 92:3564–3574.
- [11] Sharma P., Varma R., Mayor S. Nanoscale organization of multiple GPI-anchored proteins in living cell membranes. *Cell.* 2004; 116:577–589.
- [12] Meder D., Moreno M.J., Verkade P., Vaz W.L., Simons K., 2006. Phase coexistence and connectivity in the apical membrane of polarized epithelial cells. *PNAS.* 103: 329-334.
- [13] Swamy MJ, Ciani L, Ge M, Smith AK, Holowka D, Baird B, Freed JH. *Biophys J.* 2006 Jun 15; 90(12):4452-65.2006
- [14] Eggeling C., Ringemann C., Hell S.W. Direct observation of the nanoscale dynamics of membrane lipids in a living cell. *Nature.* 2009; 457:1159–1162

- [15] Simons K., Ikonen E., 1997. Functional rafts in cell membranes. *Nature*. 387: 569- 572.
- [16] Simons K. Ehehalt R. 2002. Cholesterol, lipid rafts, and diseases. *J.Clin. Invest.* 110:597-603.
- [17] Simons K., Ikonen E., 1998. Protein and lipid sorting from the trans-Golgi network to the plasma membrane in polarized cells. *Cell and Develop. Biol.* 9:503-509.
- [18] Simons K. Vaz W.L.C. 2004. Model systems, Lipid Rafts, and Cell Membranes. *Biophys. Biomol. Struct.* 33:269-295.
- [19] <http://lipidlibrary.aocs.org/Lipids/complex.html>
- [20] Simmons K., Lingwood D. 2010. Lipid Rafts as a Membrane-Organizing Principle. *Science*. 327: 46-50.
- [21] J. Zhao, J. Wu, F.A. Heberle, T.T. Mills, P. Klawitter, G. Huang, G. Costanza and G.W. Feigenson. 2007. Phase studies of model biomembranes: complex behavior of DSPC/DOPC/Cholesterol. *Biochim. Biophys. Acta - Biomembranes* **1768**: 2764–2776.
- [22] Veatch S.L., Keller S.L., 2005. Miscibility phase diagrams of giant vesicles containing sphingomyelin. *Phys Rev Lett.* 94: 148101.
- [23] Veatch S.L., Keller S.L. 2005. Seeing spots: complex phase behavior in simple mixtures. *Biochim Biophys Acta.* 1746:172–185.
- [24] Veatch SL, Gawrisch K, Keller SL. Closed-loop miscibility gap and quantitative tie-lines in ternary membranes containing diphytanoyl PC. *Biophys J.* 2006; 90:4428–4436.
- [25] Feigenson G.W, Buboltz J.T. 2001. Ternary Phase Diagram of Dipalmitoyl-PC/Dilauroyl-PC/Cholesterol: Nanoscopic Domain Formation Driven by Cholesterol. *Biophys. J.* 80:2775-2788.
- [26] F.M. Goni, A. Alonso. 2009. *Biochim. Biophys. Acta* 1788:169-177.
- [27] Heberle F.A., Wu J, Goh S.L., Petruzielo R., Feigenson G.W. 2010. Comparison of Three Ternary Lipid Bilayer Mixtures: FRET and ESR Reveal Nanodomains. *Biophys. J.* 99 3309-3318.
- [28] Konyakhina TM, Wu J, Mastroianni JD, Heberle FA, Feigenson GW. 2013. Phase diagram of a 4-component lipid mixture: DSPC/DOPC/POPC/chol. *Biochim Biophys Acta.* 1828(9):2204-14.
- [29] Petruzielo RS, Heberle FA, Drazba P, Katsaras J, Feigenson GW. 2013. Phase Behavior

- and Domain Size in Sphingomyelin-Containing Lipid Bilayers. *Biochim Biophys Acta.* 1828:1302–1313.
- [30] P. Yeagle, *The Membranes of Cells*, 2nd ed., 1993
- [31] Saiz L., Klein M.L. 2001. Influence of Highly Polyunsaturated Lipid Acyl Chains of Biomembranes on the NMR Order Parameters. *J. Am. Chem. Soc.* 123: 7381-7387.
- [32] Jump, D. B. 2002. The biochemistry of n-3 polyunsaturated fatty acids. *J. Biol. Chem.* 277:8755–8758.
- [33] Wiegand R.D., Anderson R.E.. 1983. Phospholipid molecular species of frog rod outer segment membranes. *Exp. Eye Res.* 37:159–173.
- [34] Mitchell D.C., Litman B.J. 1998. Effect of cholesterol on molecular order and dynamics in highly polyunsaturated phospholipid bilayers. *Biophys. J.* 75:896–908.
- [35] Breckenridge W.C., Gombos G., Morgan L.G. 1972. The lipid composition of adult rat brain synaptosomal membranes. *Biochim. Biophys. Acta.* 266:695–707.
- [36] Neill A.R., Masters C.J. 1973. Metabolism of fatty acids by bovine spermatozoa. *J. Reprod.Fertil.* 34:279–287.
- [37] Stillwell W., Wassall S.R.. 2003. Docosahexaenoic acid: membrane properties of a unique fatty acid. *Chem. Phys. Lipids.* 126:1–27.
- [38] Wassall S.R., Stillwell W., 2008. Docosahexaenoic acid domains: the ultimate non-raft membrane domain. *Chem. Phys. Lipids.* 153:57–63.
- [39] Wassall S.R., Stillwell W. 2009. Polyunsaturated fatty acid-cholesterol interactions: domain formation in membranes. *Biochim Biophys Acta.* 1788:24-32.
- [40] Litman, B. J., E. N. Lewis, and I. W. Levin. 1991. Packing characteristics of highly unsaturated bilayer lipids: Raman spectroscopic studies of multilamellar phosphatidylcholine dispersions. *Biochem.* 30: 313–319.
- [41] Paddy, M. R., F. W. Dahlquist, E. A. Dratz, and A. J. Deese. 1985. Simultaneous observation of order and dynamics at several defined positions in single acyl chain using <sup>2</sup>H NMR of single acyl chain perdeuterated phosphatidylcholines. *Biochem.* 24:5988 – 5995.
- [42] Salmon, A., S. W. Dodd, G. D. Williams, J. M. Beach, and M. F. Brown. 1987. Configurational statistics of acyl chains in polyunsaturated lipid bilayers from <sup>2</sup>H NMR. *J. Am. Chem. Soc.* 109:2600 –2609.

- [43] Everts, S., and J. H. Davis. 2000.  $^1\text{H}$  and  $^{13}\text{C}$  nuclear magnetic resonance of multilamellar dispersions of polyunsaturated (12:6) phospholipids. *Biophys. J.* 79:885–897.
- [44] H Binder, K Gawrisch. 2001. Dehydration induces lateral expansion of polyunsaturated 18:0-22:6 phosphatidylcholine in a new lamellar phase. *Biophys. J.* 81 (2): 969-82.
- [45] Separovic, F., and K. Gawrisch. 1996. Effect of unsaturation on the chain order of phosphatidylcholines in a dioleoylphosphatidylethanolamine matrix. *Biophys. J.* 71:274 – 282.
- [46] Huster, D., G. Paasche, U. Dietrich, O. Zschoernig, T. Gutberlet, K. Gawrisch, and K. Arnold. 1999. Investigation of phospholipid area compression induced by calcium-mediated dextran sulfate interaction. *Biophys. J.* 77:879–887.
- [47] Koenig, B. W., H. H. Strey, and K. Gawrisch. 1997. Membrane lateral compressibility measured by NMR and x-ray diffraction. *Biophys. J.* 73:1954 –1966.
- [48] Rawicz, W., K. C. Olbrich, T. McIntosh, D. Needham, and E. Evans. 2000. Effect of chain length and unsaturation on elasticity of lipid bilayers. *Biophys. J.* 79:328 –339.
- [49] D. Huster, K. Arnold, K. Gawrisch. 1998. Influence of docosahexaenoic acid and cholesterol on lateral lipid organization in phospholipid mixtures, *Biochem.* 37:17299–17308.
- [50] Olbrich, K., W. Rawicz, D. Needham, and E. Evans. 2000. Water permeability and mechanical strength of polyunsaturated lipid bilayers. *Biophys. J.* 79:321–327.
- [51] Shaikh S.R., Cherezov V., Caffrey M., Soni S.P., LoCascio D., Stillwell W., Wassall S.R. 2006. Molecular organization of cholesterol in unsaturated phosphatidylethanolamines: X-ray diffraction and solid state  $^2\text{H}$  NMR reveal differences with phosphatidylcholines. *J Am Chem Soc.*128:5375-83.
- [52] Shaikh S.R., Dumauval A.C., Castillo A., LoCascio D., Siddiqui R.A., Stillwell W., Wassall S.R. 2004. Oleic and docosahexaenoic acid differentially phase separate from lipid raft molecules: a comparative NMR, DSC, AFM, and detergent extraction study. *Biophys J.* 87:1752-66.
- [53] Soni S.P., LoCascio D.S., Liu Y., Williams J.A., Bittman R., Stillwell W., Wassall S.R. 2008. Docosahexaenoic acid enhances segregation of lipids between:  $^2\text{H}$ -NMR study. *Biophys J.* 95(1):203-14.
- [54] Koubi L., Saiz L., Tarek M., Scharf D, Klein M.L. 2003. Influence of Anesthetic and Nonimmobilizer Molecules on the Physical Properties of a Polyunsaturated Lipid Bilayer. *J. Phys. Chem. B.* 107: 14500-14508.

- [55] Kucerka N., Marquardt D., Harroun T.A., Nieh M.P., Wassall S.R., de Jong D.H., Schäfer L.V., Marrink S.J., Katsaras J. 2010. Cholesterol in bilayers with PUFA chains: doping with DMPC or POPC results in sterol reorientation and membrane-domain formation. *Biochem.* 35:7485-93.
- [56] Brzustowicz, M. R., V. Cherezov, M. Caffrey, W. Stillwell, and S. R. Wassall. 2002b. Molecular organization of cholesterol in polyunsaturated membranes: microdomain formation. *Biophys. J.* 82:285–298.
- [57] Brzustowicz, M. R., V. Cherezov, M. Zerouga, M. Caffrey, W. Stillwell, and S. R. Wassall. 2002a. Controlling membrane cholesterol content. A role for polyunsaturated (docosahexaenoate) phospholipids. *Biochem.* 41:12509–12519.
- [58] Brzustowicz, M. R., W. Stillwell, and S. R. Wassall. 1999. Molecular organization of cholesterol in polyunsaturated phospholipid membranes: a solid state <sup>2</sup>H NMR investigation. *FEBS Lett.* 451:197–202.
- [59] Shaikh, S. R., M. R. Brzustowicz, N. Gustafson, W. Stillwell, and S. R. Wassall. 2002. Monounsaturated PE does not phase-separate from the lipid raft molecules sphingomyelin and cholesterol: role for polyunsaturation? *Biochem.* 41:10593–10602.
- [60] Shaikh, S. R., V. Cherezov, M. Caffrey, W. Stillwell, and S. R. Wassall. 2003a. Interaction of cholesterol with a docosahexaenoic acid-containing phosphatidylethanolamine: trigger for microdomain/raft formation? *Biochem.* 42:12028–12037.
- [61] Shaikh, S. R., A. C. Dumaul, D. LoCassio, R. A. Siddiqui, and W. Stillwell. 2003b. Acyl chain unsaturation in PEs modulates phase separation from lipid raft molecules. *Biochem. Biophys. Res. Commun.* 311:793–796
- [62] Shaikh SR, Locascio DS, Soni SP, Wassall SR, Stillwell W. 2009. Oleic- and docosahexaenoic acid-containing phosphatidylethanolamines differentially phase separate from sphingomyelin. *Biochim. Biophys. Acta.* 178:2421-2426.
- [63] Saiz L., Klein M.L., 2001. Structural properties of a highly polyunsaturated lipid bilayer from molecular dynamics simulations. *Biophys. J.* 81:204–216.
- [64] Shaikh S.R., Brzustowicz M.R., Stillwell W., Wassall S.R.. 2001. Formation of inverted hexagonal phase in SDPE as observed by solid-state <sup>31</sup>P NMR. *Biochem. Biophys. Res. Commun.* 286:758–763.
- [65] Shaikh S.R., Kinnunb J.J. Lengb X., Williamsb JA., Wassal S.R. 2015. How polyunsaturated fatty acids modify molecular organization in membranes: Insight from NMR studies of model systems, *Biochim. Biophys. Acta.* 1848:1, 211–219

- [66] Korlach J., Schwille P., Webb W.W. and Feigenson G.W.,1999. Characterization of lipid bilayer phases by confocal microscopy and fluorescence correlation spectroscopy. *Proc. Natl. Acad. Sci.* 96: 8461–8466.
- [67] Ayuyan A.G., Cohen F.S. 2006. Lipid Peroxides Promote Large Rafts: Effects of Excitation of Probes in Fluorescence Microscopy and Electroformation Research During Vesicle Formation. *Biophys J.*91: 2172-2183.
- [68] Zhao, J., Wu, J., Shao, H., Kong, F., Jain, N., Hunt, G., and Feigenson, G.W. 2007. Phase studies of model biomembranes: macroscopic coexistence of  $L\alpha + L\beta$ , with light-induced coexistence of  $L\alpha + L_o$  phases. *Biochim. Biophys. Acta* 1768: 2777-2786.
- [69] Baykal-Caglar E1, Hassan-Zadeh E, Saremi B, Huang J. 2012. Preparation of giant unilamellar vesicles from damp lipid film for better lipid compositional uniformity. *Biochim Biophys Acta.* 1818(11):2598-604
- [70] Buboltz, J.T. 2007. Steady-state probe-partitioning fluorescence resonance energy transfer: A simple and robust tool for the study of membrane phase behavior. *Phys. Rev. E* 76: 021903.
- [71] Feigenson G.W. 2009. Phase Diagrams and Lipid Domains in Multicomponent Lipid Bilayer Mixtures. *Biochim. Biophys Acta.* 1788: 47-52.
- [72] Mayor S., Rao M. 2004. Rafts: scale-dependent, active lipid organization at the cell surface. *Traffic.* 5: 231-240.
- [73] Jacobson K., Mouritsen OG, Anderson RG. 2007. Lipid rafts: at a crossroad between cell biology and physics. *Nat. Cell Biol.* 9: 7-14.
- [74] Silvius, J. R. 2003. Fluorescence energy transfer reveals microdomain formation at physiological temperatures in lipid mixtures modeling the outer leaflet of the plasma membrane. *Biophys. J.* 85:1034–1045.
- [75] de Almeida, R. F. M., A. Fedorov, and M. Prieto. 2003. Sphingomyelin/ Phosphatidylcholine/ cholesterol phase diagram: boundaries and composition of lipid rafts. *Biophys. J.* 85:2406–2416.
- [76] de Almeida, R.F.M., Loura, L.M.S., Fedorov, A., and Prieto, M. 2005. Lipid Rafts have Different Sizes Depending on Membrane Composition: A Time-resolved Fluorescence Resonance Energy Transfer Study. *J. Mol. Biol.* 346: 1109-1120.
- [77] Silvius, J.R. 2003a. Fluorescence Energy Transfer Reveals Microdomain Formation at Physiological Temperatures in Lipid Mixtures Modeling the Outer Leaflet of the Plasma Membrane. *Biophys. J.* 85: 1034-1045.

- [78] Konyakhina TM, Goh SL, Amazon J, Heberle FA, Wu J, Feigenson GW. Control of a nanoscopic-to-macroscopic transition: modulated phases in 4-Component DSPC/DOPC/POPC/chol Giant Unilamellar Vesicles. *Biophys J Letters*. 2011;101(2):L8–L10.
- [79] Goh SL, Amazon J, Feigenson GW. Towards a better raft model: Modulated phases in the 4-component bilayer, DSPC/DOPC/POPC/CHOL. *Biophys J*. 2013;104:853–862.
- [80] Seul M., Andelman D. Domain shapes and patterns: the phenomenology of modulated phases. *Science*.1995;267:476–483.
- [81] Esterbauer H., Jurgens G., Quehenberger O., Koller E.. 1987. Autoxidation of human low density lipoproteins: loss of polyunsaturated fatty acids and vitamin E and generation of aldehydes. *J Lipid Res*. 28: 495-507.
- [82] Spiteller G. 2010. Is Lipid Peroxidation of Polyunsaturated Acids the Only Source of Free Radical That Induce Aging and Age-Related Diseases. *Rejuvenation Research*. 13:91-99.
- [83] Kim R..S, LaBella F.S.. 1987. Comparison of Analytical Methods for Monitoring Autoxidation profiles of authentic lipids. *J of lipid Res*. 1110-1117.
- [84] Frenkel E.N. 1996. Antioxidants in Lipid Foods and Their Impact on Food Quality. *Food Chem*. 57: 51-55.
- [85] Buettner G.R., Jurkiewics B.A. 1996. Catalytic Metals, Ascorbate and Free Radicals: Combinations to Avoid. *Radiation Res*. 145: 532-541.
- [86] Bligh,E.G. and Dyer,W.J. 1959. A rapid method for total lipid extraction and purification. *Can.J.Biochem.Physiol*. 37:911-917.
- [87] Morales-Pennington N.F, Wu J., Farkas E.R., Goh, S.L, Konyakhina T.M., Zheng J.Y, Webb WW, and Feigenson G.W. 2010. GUV Preparation and Imaging: Minimizing Artifacts. *Biochim. Biophys. Acta*. 1798:1324-1332.
- [88] Heuvingh, J., Bonneau, S., 2009. Asymmetric Oxidation of Giant Vesicles triggers Curvature-associated Shape Transition and Permeabilization. *Biophys J*. 97: 2904–2912.
- [89] Feigenson GW, Buboltz JT. Ternary phase diagram of dipalmitoyl-PC/dilauroyl-PC/cholesterol: nanoscopic domain formation driven by cholesterol. *Biophys J*. 2001;80: 2775–2788.
- [90] Buboltz, J.T., and Feigenson, G.W. 1999. A novel strategy for the preparation of liposomes: rapid solvent exchange. *Biochim. Biophys. Acta* 1417: 232-245.

- [91] Heberle, F.A., Buboltz, J.T., Stringer, D., and Feigenson, G.W. 2005. Fluorescence Methods to Detect Phase Boundaries in Lipid Bilayer Mixtures. *Biochim. Biophys. Acta* 1746: 186-192.
- [92] Buboltz, J.T., Bwalya, C., Williams, K., and Schutzer, M. 2007b. High-Resolution Mapping of Phase Behavior in a Ternary Lipid Mixture: Do Lipid—Raft Phase Boundaries Depend on the Sample Preparation Procedure? *Langmuir* 23: 11968-11971.
- [93] Reeves JP, Dowben RM. Formation and properties of thin-walled phospholipid vesicles. *Journal of Cellular Physiology*. 1969;73:49–60.
- [94] Akashi K, Miyata H, Itoh H, Kinoshita K. Preparation of giant liposomes in physiological conditions and their characterization under an optical microscope. *Biophys J*. 1996;71:3242–3250.
- [95] Feigenson GW, Buboltz JT. Ternary phase diagram of dipalmitoyl-PC/dilauroyl-PC/cholesterol: nanoscopic domain formation driven by cholesterol. *Biophys J*. 2001;80: 2775–2788.
- [96] Mills TT, Huang J, Feigenson GW, Nagle JF. Effects of cholesterol and unsaturated DOPC lipid on chain packing of saturated gel-phase DPPC bilayers. *Gen Physiol Biophys*. 2009;28(2):126–39.
- [97] Marsh JS. *Principles of Phase Diagrams*. McGraw-Hill; New York: 1935. pp. 122–170.
- [98] Farkas ER, Webb WW. Precise and millidegree stable temperature control for fluorescence imaging: application to phase transitions in lipid membranes. *The Review of Scientific Instruments*. 2010;81:093704.
- [99] Honerkamp-Smith A. R., P. Cicuta, M. Collins, S. L. Veatch, M. Schick, M. den Nijs, and S. L. Keller Line tensions, correlation lengths, and critical exponents in lipid membranes near critical points, *Biophys. J*. 2008: 5(1) 236-46.
- [100] Veatch SL, Cicuta P, Sengupta P, Honerkamp-Smith A, Holowka D, Baird B. Critical fluctuations in plasma membrane vesicles. *ACS Chem Biol*. 2008;3:287–293.
- [101] Honerkamp-Smith AR, Veatch SL, Keller SL. An introduction to critical points for biophysicists; observations in lipid membranes. *Biochim Biophys Acta*. 2009; 1788(1):53–63.
- [102] Tian A, Johnson C, Wang W, Baumgart T. Line Tension at Fluid Membrane Domain Boundaries Measured by Micropipette Aspiration. *Physical Review Letters*. 2007;98:18–21

- [103] Angelova M.I. and Dimitrov D.S. 1986. Liposome Electroformation. *Faraday Discuss, Chem. Soc.* 81:303–312.
- [104] Dimitrov D.S. ,Angelova M.I. 1987.Lipid swelling and liposome formation on solid surfaces in external electric fields. *New Trends in Colloid Science.* 48–56.
- [105] Dimitrov D.S. and Angelova M.I., 1988. Lipid swelling and liposome formation mediated by electric fields. *Chem. Interfacial Electrochem.* 19: 323–336.
- [106] Angelova M.I. and Dimitrov D.S.1988. A mechanism of liposome Electroformation. *Prog. Colloid Poym. Sci.* 76: 59–67.
- [107] Angelova M.I., Soléau S., Méléard P., Faucon J.F. and Bothorel P. 1992. Preparation of giant vesicles by external AC fields. Kinetics and application. *Prog. Colloid Polym. Sci.* 89:127–131.

## APPENDIX

### **Synthesis of a novel phosphorescent lipid-probe analog and measurement of its phosphorescence signal in liposomes.**

#### **A.1 Introduction**

How long do small lipid domains last? The lifetime of lipid ‘rafts’ has not been measured. Phosphorescent probes might be useful for this purpose, but these have been mainly used to study rotational motions of proteins in membranes [1, 2]. For liquid bilayer domains, given a translational diffusion coefficient  $\sim 10^{-8}\text{cm}^2\text{sec}^{-1}$ , a probe within a domain of diameter 100 nm would be expected to reside in that environment for  $\sim 2$  ms, and in a domain of 10 nm diameter for  $\sim 20$   $\mu\text{s}$ . In addition to diffusion, the lifetime of the domain itself can influence the measured probe signal. These timescales fall within the vast range of phosphorescent lifetimes. With a model that accounts for measured probe lifetime in two distinct environments, measured equilibrium partition between the environments, measured diffusion coefficients in the two environments, and known area fractions of the two environments from a thermodynamic tieline, we can recover information about domain lifetime and geometry. This would be a novel application of phosphorescence to the study of membrane domain structure that involves a synthesis of novel phosphorescent lipid-probe analog.

Eosin Y (tetra-bromo Fluorescein) and Erythrosin B (tetra-iodo Fluorescein) are phosphorescent probes with lifetimes in the micro-to-millisecond range [3-9]. A recently published super-resolution STED study on live cells [10] has shown that GPI-anchored proteins have a lifetime of approximately 10-20 ms in small nanoscopic domains (<20 nm). It is a surprising and interesting result, indicative that even nanoscopic domains may have lifetimes on a timescale

relevant to biological reactions (micro-to milli-second range). There is a significant literature [11, 12] that describes how the long lifetime of the triplet state of eosin (tetrabromo fluorescein) or erythrosin (tetraiodo fluorescein) enable determination of the molecular motions that occur on the timescale of micro- to milli-seconds. A much smaller literature describes the use of these phosphorescent probes to study fatty acid rotational motions in membranes [13], i.e. the effort required for otherwise readily obtainable motional information caused this research direction to wither. Phosphorescent lipid analogs are not commercially available, and there are no data available on using phosphorescent probes for studying membrane domains. The outlined here set of experiments, if successful, might allow to make a correlation between lifetimes of phosphorescent probes and the sizes of the domains in model systems.

For measuring phosphorescence, we benefit from the expertise of others [12, 13]: for eosin and erythrosin probes, delayed fluorescence is in the range 500 - 600 nm, with phosphorescence distinguishable at 620 - 760 nm; erythrosin has an unusually high quantum yield QY for phosphorescence together with low QY for fluorescence; dissolved oxygen is sufficiently depleted by several minutes of argon bubbling. For oxygen removal we use both chemical reduction by sodium sulfite, as well as argon bubbling. We have a phosphorescence lifetime instrument, and learned to make lifetime measurements.

For the proposed studies, the key criterion is that we must have distinct lifetimes for our probe in the two phases, Ld and Lo. The local probe environment is likely to have pronounced but hard to predict influence on the lifetime and QY. For this reason, we anticipate synthesizing and screening for suitable lifetimes a variety of headgroup-labeled probes. We have synthesized eosin-PE (Fig A1), starting from eosin-5-isothiocyanate and DOPE, based on our previous syntheses of lissamine rhodamine-labeled PEs by this route [14]. Erythrosin B has a surprisingly strong signal

(Fig A2).

## A.2 Data analysis and connection to models<sup>4</sup>

A phosphorescent probe can experience two distinct environments, coexisting Lo and Ld phase domains. The probe has phosphorescence lifetimes  $\tau_o$  and  $\tau_d$ , and diffusion coefficients  $D_o$  and  $D_d$  in each pure phase, and relative concentration in the two phase given by partition coefficient  $K_p$ . We achieve crucial simplification of our analysis by working along a thermodynamic tieline, because then we know the area fraction  $H$  occupied by each phase,  $H_o$  and  $H_d$ . Our goal here is to relate the measured lifetime decay curve [15, 16] to these known parameters and to the geometric description of the phase separation.

The experimental phosphorescence decay can be written,

$$P(t) = \int \exp \left[ - \int_0^t \frac{1}{\tau(\gamma(s))} ds \right] \mathcal{D}[\gamma]$$

where  $\mathcal{D}[\gamma]$  is the probability of the diffusion path and  $\tau(\gamma)$  is the local phosphorescence lifetime  $\tau_o$  or  $\tau_d$  along the diffusion path. There are two extreme cases, slow diffusion resulting in the two distinct lifetimes  $\tau_o$  and  $\tau_d$ , and fast diffusion that mixes the two lifetimes to give a single value that we call  $\tau_{mix}$ . More important for our studies is the intermediate case of three (overlapping) lifetime distributions, because this case contains information about domain size and geometry. We define the narrow areas of “mixing” on each side of the phase boundary as  $h_o$  and  $h_d$ , as shown in the figure. These are related to the boundary perimeter  $C$  and the convexity/concavity of the

---

<sup>4</sup> Data analysis and mathematical equations were derived by Jon Amazon, former graduate student at GWF lab.

geometry, where  $B < 0$  means  $L_o$  domains are convex,  $B > 0$  means  $L_d$  domains are convex, as

$$h_o \approx 2C\sqrt{D_o\tau_o} + 4BD_o\tau_o \text{ and } h_d \approx 2C\sqrt{D_d\tau_d} - 4BD_d\tau_d.$$

In sum, given all the measureable parameters, mixing areas we fit only the geometric parameters  $C$  and  $B$ . We expect three broad peaks, centered at  $\tau_o$  and  $\tau_d$  and  $\tau_{mix}$ . Areas  $I$  under each peak:

$$I_o = \frac{K_p(H_o - h_o)}{K_pH_o + H_d}; \quad I_d = \frac{H_d - h_d}{K_pH_o + H_d}$$

$$I_{mix} = \frac{K_ph_o + h_d}{K_pH_o + H_d}$$

### A.3 Material and Methods

100 mg of FITC (in dry box) was dissolved in 1ml of EtOH in an amber vial. 164 mg (106  $\mu$ L) of bromine was added drop by drop and the reaction mixture was stirred for 2 hr in dark dry box. Initial reaction proceeds towards the formation of undesirable dibromo product (dibromofluorescein, also known as Eosin B, which is non-phosphorescent) and the reaction solution appears clear. Upon the reaction proceeding further, the tetrabromo derivative (Eosin Y, phosphorescent) appears, evident by precipitation of red crystals. The reaction was stirred for 2 hr at 23°C to allow the rxn to go to completion. The insoluble material, the compound of interest, was collected by filtration using a Büchner Funnel with Whatman#1 filter paper and washed with

10 ml of cold EtOH. Collected crystals were solubilized in 10mM Phosphate Buffer, pH 7.4 and re-precipitated at 4°C with chilled 1N Phosphoric acid. Crystals were then centrifuged (centrifuge at 4°C) and washed with ice cold distilled water 3X times. The final product (crystals) were collected and dried on vacuum overnight.

Synthesis of phosphorescent lipid Eosin Y-PE analogs was achieved by reacting eosin or erythrosine isothiocyanates with the PE amino groups. All reactions of PE lipids with phosphorescent reagents were carried out at 23°C under dry conditions (dry box, RH ~0%) and with exclusion of light. To a solution of DOPE (25 mg, 33.6  $\mu$ moles) in dry CHCl<sub>3</sub> (2 mL, dried over 3A sieves) was added triethylamine (0.05 mL, 35  $\mu$ mol). After the solution was stirred for 30 min, a solution of phosphorescent eosin Y isothiocyanate, synthesized during step 1 of the reaction (1.2 molar equivalent, 28.5 mg, 40.3  $\mu$ mol) was added. The reaction mixture was stirred for 24 h at room temperature in the dark and in the dry box. The product was dried on the vacuum to give a residue, which was then purified using the combination of methods.

We have developed a purification method that produces modest separation of the compound of interest. It is a two-fold process that utilizes 1) column chromatography (SiO<sub>2</sub>) and 2) preparative TLC plates. The best separation is achieved by first purifying a crude rxn mix on a column, (column volume ~100 ml of ~30g of silica per ~10 mg of crude reaction mix, eluting solvent 65/25 = chloroform/methanol). Column separation allows separating unreacted PE from the product. Unfortunately, unreacted Eosin Y runs together with product EosinY-DOPE. Therefore, we used a second method for purification, TLC preparative plates. This particular mixture has a high tendency to ‘overload’ a silica column. The best separation results are achieved with preparative plate TLC loading with ~0.5 mg per plate.

#### **A.4 Results**

We have synthesized a novel phosphorescent lipid-analog probe and demonstrated its effective phosphorescence sensitivity. The synthesis pathway is shown in Fig. A1.

The synthesis of Eosin Y from Fluorescein was described by [5]. The covalent addition of lipid to Eosin Y was based on the method by [17, 18]. The purity of the final product was judged to be >95% using TLC analysis and absorbance measurements (data not shown). This particular molecule, Eosin Y-DOPE, has never been reported in the literature nor is it available commercially. We have also verified that a tetraiodo-derivative of Fluorescein (Erythrosin B) produces a strong phosphorescence signal which is a suitable candidate for the proposed lifetime studies (Fig.A2). Both Eosin Y-DOPE and Erythrosin B exhibit delayed fluorescence peaks at ~550 nm, and phosphorescence peaks at ~685 nm [108]. Erythrosin B has stronger signal and longer lifetime. Samples were deoxygenated using Argon bubbling for 30 min prior to measurements. Phosphorescence decay curves for Erythrosin B are shown in Fig. A2. The absence of the phosphorescence emission in the presence of oxygen reinforces the conclusion that the observed signal at 695 nm is in fact due to phosphorescence.

#### **A.5 Discussion and future directions**

Is it possible to relate the phosphorescence lifetimes of suitably labeled lipid probes to the actual geometries and lifetimes of the lipid domains? Phosphorescent probes have been used to study rotational motions of proteins [2, 3]. Eosin Y (tetra-bromo Fluorescein) and Erythrosin B (tetra-iodo Fluorescein) are two phosphorescent probes known to have lifetimes in the micro-to-millisecond range [3- 9]. Currently, there is no consensus on the lifetime of lipid domains in model

systems. There have been recent studies on live cells using a super-resolution STED method [10], which have concluded that GPI-anchored proteins have lifetimes of nearly 10-20 ms in small (< 20 nm) nanoscopic domains. The result indicates that even nanoscopic domains may have lifetimes on a timescale relevant to biological reactions, i.e. micro-to-milliseconds). Upon the successful implementation of this technique, we will be able to reliably measure domain lifetimes and possibly sizes through the application of phosphorescent probes.

We propose to synthesize a novel Erythrosin B-DOPE, which will be used for the bulk of the lifetime experiments. We have already synthesized the phosphorescent probe Eosin Y-DOPE. Eosin Y-DOPE has a strong phosphorescence signal; however, Erythrosin B (Fig. A2) has an even stronger phosphorescence signal, a higher quantum yield for phosphorescence, and a longer lifetime.

It is critical to have probes with significantly different lifetimes in pure Lo and Ld phases to clearly distinguish lifetime observations in samples with coexisting phases. Measurements in 'pure' phases can be achieved by preparing Erythrosin B-DOPE in an all-Ld phase bilayer DOPC, and also in an all-Lo phase bilayer of DOPC + chol (60%). Samples must be carefully deoxygenated by bubbling with Argon and measured using the PTI instrument QuantaMaster™ 30 spectrofluorimeter with a pulsed xenon flash lamp having a ~180 microsecond pulse width. Erythrosin B-DOPE may exhibit minor lifetime variability in the Lo and Ld phases. To accommodate such a situation we may have to use the following approach: 1) induce a range of lifetimes in Erythrosin B-DOPE by externally adding salts containing heavy atoms (NaBr) or spin-labeled probes [19]; or 2) synthesize additional probes and screen their lifetimes until we find probes with appropriate lifetime values. It should be noted that it is possible to induce phosphorescence and intersystem crossing from an excited singlet to triplet state and in doing so

increase the quantum yield of phosphorescence. This is accomplished at the expense of fluorescence's quantum yield which diminishes as heavy-atoms are introduced to the fluorescence compound, a phenomenon commonly referred to as a 'heavy'-atom effect.

Erythrosin B-DOPE can be used in the measurement of lifetimes for various-sized domains. After successful measurements in the pure Ld and Lo phases, we could further evaluate the system by measuring phosphorescence lifetimes in BSM/SDPC/SOPC/chol with a controllable switch from macro-to-nano domains. A proper theoretical model for lifetime analysis is critical for deriving correlations between probe lifetimes in given phases and domain sizes. A lifetime decay curve in the presence of coexisting phases is directly dependent on the phase-specific probe lifetimes  $\tau\{Ld\}$  and  $\tau\{Lo\}$ , diffusion coefficients  $D\{Ld\}$  and  $D\{Lo\}$ , probe partition coefficient ( $Kp$ ), and lifetime  $\tau_{domain}$ . We will develop analytical models for a representative sample of potential domain sizes and geometries including those occurring from modulated phase behavior. The desired end goal is to better develop and define the relationship between probe lifetimes and sizes and the lifetimes of lipid domains.

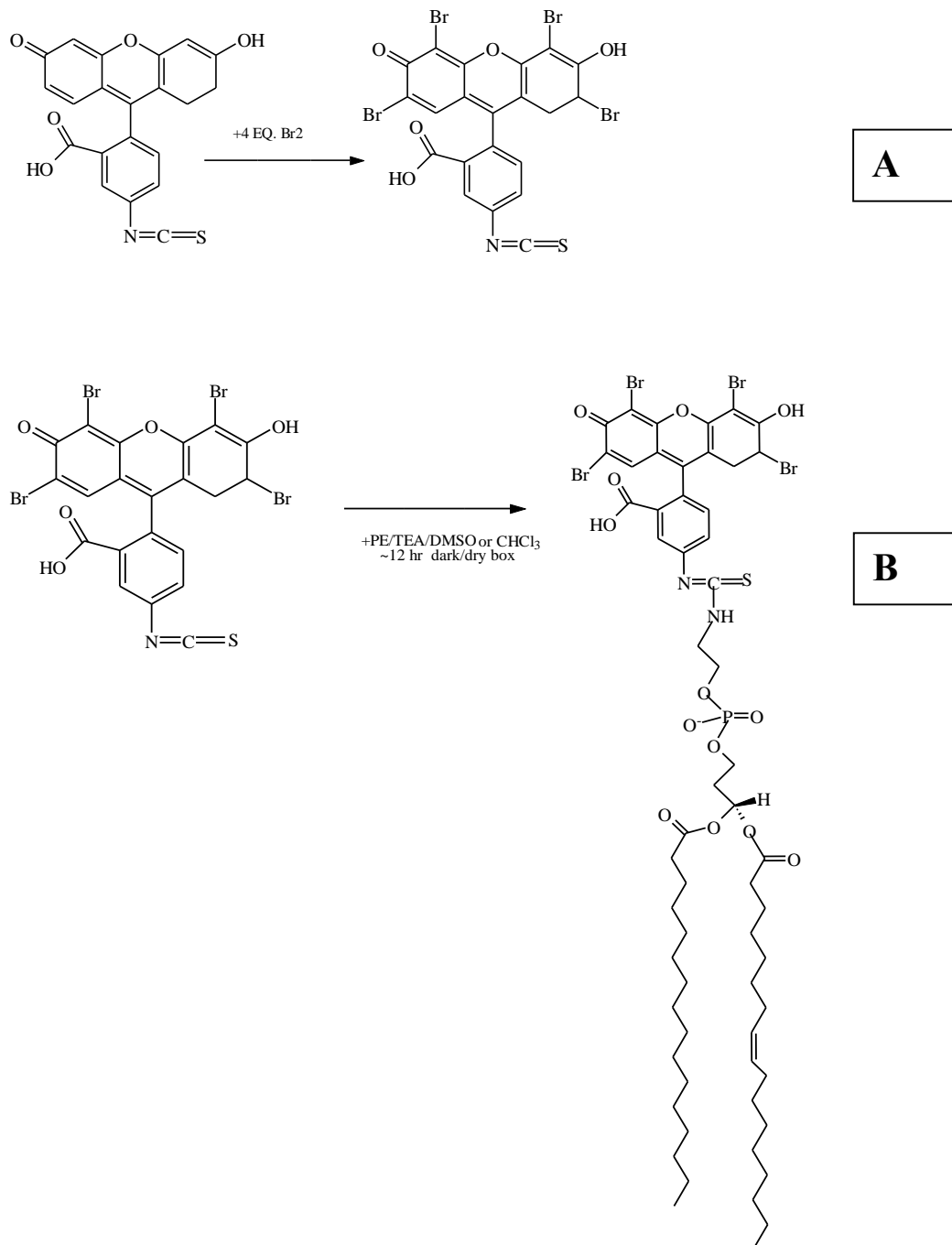


**Figure A.1** Synthesis of a phosphorescent lipid probe. Panel (A) shows step 1, bromination reaction. Conversion of Fluorescein Isothiocyanate to its tetrabromo-derivative Eosin Y Isothiocyanate. Panel (B) shows step 2: covalent addition of DOPE to Eosin Y Isothiocyanate.

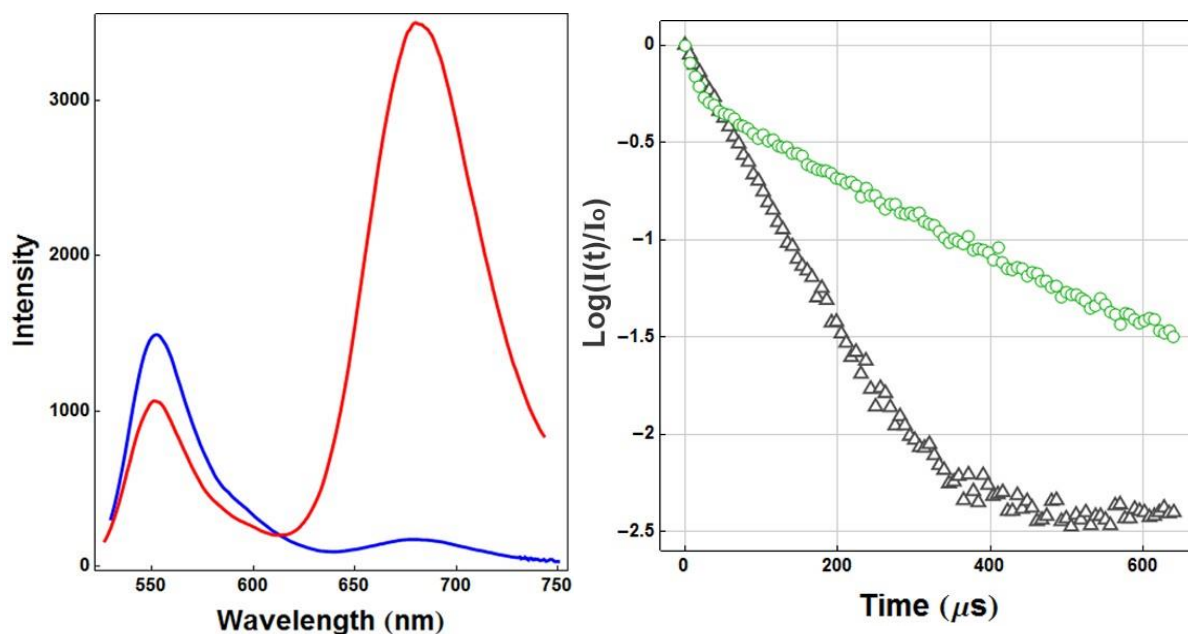


**Figure A.2** (left) 10 $\mu$ M erythrosin em spectra, ex 500nm, blue is delayed fluorescence, red 695nm at 200 $\mu$ sec delay after ex is phosphorescence; (right) decay curves for 10 $\mu$ M erythrosin in 5mM DOPC +1% CTAB liposomes (green) has lifetime 195 $\mu$ s with a small 50 $\mu$ s component; black triangles are in the absence of liposomes, lifetime 50 $\mu$ s. pH = 7 for all.

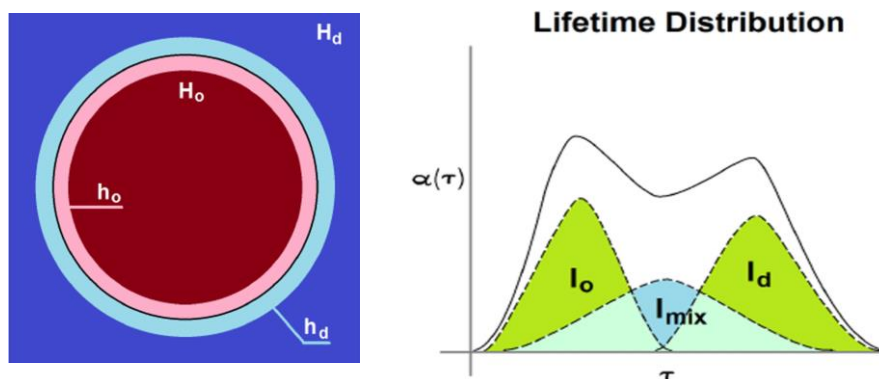


**Figure A.3**, (left) circular domain showing lifetime  $h_0$  and  $h_d$ ; (right) deconvolution of lifetime distribution.

## References

- [1] McPherson RA, Sawyer WH, and Tilley L. 1992. Rotational Diffusion of the Erythrocyte Membrane Protein Band 3: Effect of Hemichrome Binding. *Biochemistry* 31:512-518.
- [2] Tilley L, Sawyer WH, Morrison JR, and Fidge NH. 1988. Rotational Diffusion of Human Lipoproteins and Their Receptors Determined by Time-Resolved Phosphorescence Anisotropy. *J. Biol. Chem.* 263:17541-17547.
- [3] Jovin TM and Vaz WLC. 1989. Rotational and Translational Diffusion in Membranes Measured by Fluorescence and Phosphorescence Methods. *Meth. Enz.* 172:471.
- [4] Blatt E and Corin AF. 1986. The Microsecond Rotational Motions of Eosin-Labelled Fatty Acids in Multilamellar Vesicles. *Biochim. Biophys. Acta* 857:85-94.
- [5] Cherry RJ. 1978. Measurement of Protein Rotational Diffusion in Membranes by Flash Photolysis. *Meth. Enz.* 54:47-61.
- [6] Pravinata LC, You Y, Ludescher RD, Erythrosin B Phosphorescence Monitors Molecular Mobility and Dynamic Site Heterogeneity in Amorphous Sucrose. 2005. *Biophys L.* 88:3551-3561.
- [7] Ludescher RD, You Y. Phosphorescence of Erythrosin B as a Robust Probe of Molecular Mobility in Amorphous Solid Sucrose. 2006. *Applied Spectroscopy.* 60:813-819.
- [8] Simon-Lukasik, KV, Ludescher RD. Erythrosin B phosphorescence as a probe of oxygen diffusion in amorphous gelatin films. 2003. *Food Hydrocolloids.* 18: 621-630.
- [9] Garland PB, Moore CH. 1979. Phosphorescence of Protein-Bound Eosin and Erythrosin. A Possible Probe for Measurements Of Slow Rotational Mobility. *Biochem. J.* 183, 561-572.
- [10] Eggeling C, Ringemann C, Medda R, Schwarzmann G, Sandhoff K, Polakova S, Belov VN, von Middendorff C, Schonle A, and Hell SW. 2009. Direct Observation of the Nanoscale Dynamics of Membrane Lipids in a Living Cell. *Nature.* 457:1159-1162.
- [11] Damjanovich S, Tron L, Szollosi J, Zidovetzki R, Vaz WLC, Regateiro F, Arndt-Jovin DJ, Jovin TM. 1983. Distribution and mobility of murine histocompatibility H-2K antigen in the cytosolic membrane. *Proc. Nat. Acad. Sci. USA* 80:5985-5989.
- [12] Jovin TM, Vaz WLC. 1989. Rotational and translational diffusion in membranes measured by fluorescence and phosphorescence methods. *Meth. Enz.* 172:471-513.
- [13] Blatt E, Corin AF. 1986. The microsecond rotational motions of eosin-labelled fatty acids in multilamellar vesicles. *Biochim. Biophys. Acta* 857:85-94.

- [14] Gruber HJ, Schindler H. 1994. External surface and lamellarity of lipid vesicles: a practiceoriented set of assay methods. *Biochim. Biophys. Acta* 1189:212-224.
- [15] Beechem JM, Knutson JR, and Brand L. 1986. Global analysis of multiple dye fluorescence anisotropy experiments on proteins. *Biochem. Soc. Trans.* 14:832-835.
- [16] Grinvald A, Steinberg IZ. 1974. On the analysis of fluorescence decay kinetics by the method of least squares. *Anal. Biochem.* 59:583-598.
- [17] Sun X.L, Liu H., Orban J.M, Sun L., Chaikof E.L.2001.Synthesis and Terminal Functionalization of a Polymerizable Phosphatidylethanolamine. *Bioconjugate Chem.* 12:673-677.
- [18] Silvius J.R., Leventis R., Brown P.M., Zuckermann M. 1987. Novel fluorescent phospholipids for assays of lipid mixing between membranes. *26: 4279-4287*
- [19] London E., and Feigenson G.W. 1981. Fluorescence quenching in model membranes. 1. Characterization of quenching caused by a spin-labeled phospholipid. *Biochem.* 20:1932-1938.